Vacuum Ultraviolet Time-resolved Photoelectron Spectroscopy using Velocity Map Imaging

Michael Hemsworth

A thesis submitted in partial fulfillment

of the requirements for the degree of

MASTER OF SCIENCE

in Physics

Department of Physics

Faculty of Science

University of Ottawa

Abstract

This thesis covers two separate but related projects. The first project covers the design and simulation of a new angle-resolved photoelectron-photoion coincidence (PEPICO) spectrometer. The spectrometer utilizes velocity map imaging (VMI) to measure the photoelectron kinetic energy and angular distributions in coincidence or covariance with the photoion mass spectrum using a Wiley-McLaren time-of-flight mass spectrometer. The instrument was also designed for 3D VMI, a technique that measures the full three dimensional photoelectron velocity distribution. Simulations were performed to measure the spectrometer performance with respect to photoelectron kinetic energy resolution, mass resolution and photoelectron time spread resolution, the latter being important for 3D VMI.

The second project covers a time-resolved velocity map imaging photoelectron spectroscopy study of nonadiabatic excited state dynamics in carbonyl sulfide (OCS). An ultrafast tunable vacuum ultraviolet light source was tuned to two different vibrational states of the $^1\Sigma^+$ excited state. A direct measurement of the excited state lifetimes was made. The photoelectron kinetic energy and angular distributions were used to determine three different ionization mechanisms: we found evidence for direct ionization, superexcited OCS* molecular autoionization and superexcited photofragment S* autoionization. In the future, definitive evidence of our assignments could be made with a coincidence measurement, thus the results from this experiment will be used as a benchmark for the new spectrometer described above.

Acknowledgments

I would first and foremost like to thank my supervisor, Dr. Albert Stolow, for the invaluable guidance and expertise he has given me over my time here in Ottawa. He has helped me learn so much, about both science and myself, over the last two years. I look forward to visiting again soon.

I would also like to thank everyone else in the Stolow group for being so helpful and inviting. Dr. Rune Lausten was invaluable in teaching me the intricacies of running an amplified laser system and I learned so much from him about optics in general. Dr. Anja Röder introduced me to the lab side of TRPES experiments, spent many long hours with me troubleshooting the OCS experiment, and taught me the importance of keeping a well written lab book. I would like to thank Dr. Andrey Boguslavskiy for his assistance both in the lab and for data analysis, Scott Goudreau for helping me with code and experiments, Dr. Adrian Pegoraro for his helpful suggestions in group meetings, Doug Moffatt and Denis Guay for keeping the lab equipment in running condition, and finally Dr. Paul Hockett for having many interesting conversations with Rune and I over a pint at the pub. Without all of you this work would not have been possible (and would have been much less fun).

October 2020

Contents

List of Figures

List of Tables

Chapter 1

Introduction

One of the most challenging yet important problems in molecular physics is the coupling of electronic and vibrational degrees of freedom. This fundamental coupling leads to charge flow and energy transfer in molecules, through processes such as radiationless transitions, internal conversion, isomerization, proton and electron transfer, etc[1–8], which are the underlying effects governing, as examples, photosynthesis, vision[9], and molecular solar cell technology[10]. The timescales of these dynamic processes is of fundamental importance to their function in the natural world; they are always in competition with other dissipative processes. In order for e.g. vision to function, the isomerization of rhodopsin following absorption of a photon must occur on timescales much faster than the dissipation of energy to the surrounding medium[9]. This leads to a picture in which the dynamics govern molecular function as opposed to the often argued structure-function relationship[11].

The electronic and vibrational coupling can be understood in terms of the breakdown of the Born-Oppenheimer approximation (BOA), which is an adiabatic approximation that allows the separation of electronic from nuclear motions. Using the BOA, nuclear potential energy surfaces can be defined that describe molecular structures and nuclear trajectories, permitting a mechanistic picture of the molecular dynamics[12]. The breakdown of the BOA occurs exactly when the nuclear potential energy surfaces of different electronic states are in close proximity. In these regions, the concept of separate electronic and vibrational states becomes obscure[13], which as alluded to above, makes studying non-adiabatic dynamics one

of the most challenging problems in molecular physics.

A powerful method used to study molecular dynamics is the ultrafast pump-probe technique, pioneered by Zewail and coworkers[14]. An ultrafast pump pulse is used to excite a coherent superposition of stationary states, which creates a time-evolving wavepacket. A time-delayed ultrafast probe pulse then projects the evolving dynamics onto a final state observable. It is important to note the choice of final state projection by the probe pulse critically determines the accessible information. As the photochemical reaction evolves towards the products, we can expect both the electronic and vibrational structures to change significantly, where selection rules and other restrictions can limit the ability to follow the dynamics along the entire reaction coordinate. Therefore, care must be taken when choosing a probing scheme. Many different probing schemes exist, each with their own advantages and limitations. Some common techniques include transient absorption[15], four-wave mixing[16], resonance-enhanced multiphoton ionization[17], high harmonic spectroscopy[18] and time-resolved photoelectron spectroscopy (TRPES)[19].

In this thesis, the probing scheme we will focus on is TRPES, which is sensitive to both electronic configurations and vibrational dynamics[20], allowing it to follow ultrafast non-adiabatic processes. TRPES provides unprecedented details on charge and energy flow inside molecules[13]. Specifically, we will explore the technique of velocity map imaging (VMI) TRPES in the gas phase. This technique detects photoelectron kinetic energy and angular distributions emitted from a molecule following ultrafast irradiation by a pump excitation and a time-delayed ionizing probe laser pulse. VMI TRPES has several advantages as a probe[21]:

- Ionization is always allowed given that the emitted photoelectron helps conserve angular momentum
- The photoelectron angular distributions provide details about the symmetries of the evolving states[22]

- Single electrons are easily detectable making TRPES extremely sensitive
- Ions can be detection in coincidence to further differentiate the carrier of the photoelectron spectrum
- Multiphoton processes are easily revealed as higher photoelectron kinetic energy releases

Our goal here is to improve upon the VMI technique, simulating, designing and then building a spectrometer from the ground up with new features such as 3D VMI and coincidence measurements in mind. We also performed a VMI experiment with an existing spectrometer to study the ultrafast molecular dynamics of carbonyl sulfide (OCS) which reinforced the design choices we have made.

Thesis outline

This thesis is split into two parts over three chapters. In the first part, Chapter 2, we present the simulation and design of a new VMI photoelectron spectrometer at the University of Ottawa. We evaluate the simulated performance of several designs based on photoelectron energy resolution, ion mass spectrometry mass resolution, and time spread resolution for 3D VMI. A new advance in VMI electrode potentials that increases the time spread by a factor of two while maintaining VMI conditions will be discussed. The spectrometer was designed for photoelectron-photoion covariance measurements, which correlates electrons and ions from the same photoionization event. This technique provides exquisite detail into the photoionization process and would have been invaluable for the experiments described in Chapter 4, as will be mentioned below.

The second part of this thesis focussed on a time-resolved velocity map imaging photoelectron spectroscopy study of the molecule carbonyl sulfide. Chapter 3 describes the ultrafast tunable vacuum ultraviolet light (VUV) source and the existing VMI spectrometer utilized in the OCS experiment of Chapter 4, as well as topics surrounding stability, data pre-processing

and calibration. It was written specifically about the experimental setup in Femtolab 4 at the National Research Council on 100 Sussex Drive.

Chapter 4 describes a valence shell TRPES study of the $^1\Sigma^+$ excited state dynamics of OCS at two different VUV pump wavelengths. These experiments demonstrate the importance of understanding the energetic structure of the molecular ionization continuum states in order to understand the projection of the excited state onto the final state by the probe pulse. We were able to compare the resulting photoelectron spectra and angular distributions to deduce three different final state projections by the probe pulse: direct ionization to the molecular ionization continuum, projection to superexcited Rydberg states followed by molecular autoionization, and projection to superexcited Rydberg states, followed by dissociation of the neutral superexcited molecule into neutral CO and superexcited S* photoproducts, the latter subsequently autoionizing to produce S^+ and an electron. This study of OCS will be used as a benchmark test of the new VMI described in Chapter 2. As alluded to above, photoelectron photoion covariance measurements of this process would provide definitive evidence for the conclusions drawn in this chapter. This OCS valence shell spectroscopy study will also be used as a benchmark for future ultrafast core shell X-ray spectroscopic studies. It has often been argued that probing the atom specific local charge density variations will offer new insights into the underlying dynamics. OCS, comprised of three distinct atoms, offers three different core-shell perspectives on the excited state dynamics. The valence shell study presented in this thesis will be directly compared, in a future study, to the core shell counterparts to verify the claim that ultrafast X-ray spectroscopy is a key advance in the field of molecular dynamics.

Chapter 2

Velocity Map Imaging Spectrometer Design

2.1 Introduction

As stated in Chapter 1, time-resolved photoelectron spectroscopy is a powerful tool for studying ultrafast non-adiabatic processes because it is sensitive to both electronic and vibrational dynamics. The photoelectron kinetic energy and angular distributions provide exquisite detail about charge and energy flow inside molecules. There are a wide variety of techniques which can be used to measure these photoelectron distributions, each with their own advantages and disadvantages. In this chapter, the design of a new photoelectron spectrometer for the University of Ottawa will be presented. I will focus on the specific technique of velocity map imaging (VMI), why we chose it as the basis for the new instrument, and the modifications we have made to the standard design to allow for 3D VMI and photoelectron-photoion covariance measurements.

2.2 VMI photoelectron spectroscopy techniques

There are several techniques employed to measure photoelectron kinetic energy and angular distributions, each with their own advantages and disadvantages. While the specifics of each technique differ, the fundamental principles of charged particle detection remain the

same. All methods require a source of target molecules, typically a gas jet supplied by a pulsed valve, that is intersected by a source of ionizing radiation, typically a laser. The intersection of the gas jet with the laser is called the interaction region, where separation of electrons from the parent ions occurs. A set of electric and/or magnetic fields is then used to accelerate electrons towards a detector that measures one, two or three components of the photoelectron initial velocity vector. The components can be split into two categories: v_z, defined as the velocity in the direction of the detector and v_x/v_y defined as the velocity components in the plane parallel to the detector face. The categories are distinct, as v_z is typically measured using time-of-flight (TOF) methods whereas v_x/v_y are measured with techniques which utilize position sensitive detectors. All experiments must be performed under high to ultrahigh vacuum conditions in order to avoid any trajectory deflections of the charged particles due to collisions with background gases.

Here, the technique we are interested in is VMI, which is an example of the latter category. First described by Eppink and Parker[23], VMI maps the initial velocity vector of an electron to a point on the detector, regardless of initial position. Electrons born in the interaction region expand in spherical shells, called Newton spheres, with radii expand at a rate proportional to the electron kinetic energy. A set of open ring electrostatic lenses accelerate the 3D Newton spheres towards a microchannel plate (MCP) detector where they are "pancaked" into a 2D projection. The 2D projection encodes the electron kinetic energy in the radial coordinate and the angular distribution in the angular coordinate. Provided that the physics of the interaction maintains cylindrical symmetry about an axis parallel to the detector face, the full 3D distribution can be reconstructed from the 2D projection using an Abel inversion algorithm. In practice this means the laser polarization must be parallel to the detector face. What makes VMI so powerful is its ability to measure the photoelectron angular distributions, which provide exquisite detail for determining photoionization dynamics which relate to molecular reaction pathways. VMI also has the ability to measure all photoelectron

energies simultaneously and a 4π collection efficiency, making data acquisition fast compared to other methods. One downside of VMI is the relatively low energy resolution, typically around $\Delta E/E = 1\%$ (measured at the largest detector radius). Improvements to the standard VMI design have been made to increase the resolution[24,25] and incorporating these will be a main design goal for the new spectrometer.

Another downside is the cylindrical symmetry requirement, which precludes the use of pump-probe crossed polarization or magic angle polarization schemes, as well as some molecular alignment techniques [26, 27]. It would be of great interest to remove the cylindrical symmetry restriction in order to open the possibility of using these techniques. A tomographic reconstruction algorithm can be used to do so[28,29], however, this requires collection of multiple projections at different laser polarization angles. In a time-resolved experiment, data acquisition becomes prohibitively lengthy as collection of multiple projections would be required at each time delay.

In theory, it is possible to obtain the full 3D distribution without the need for inversion by measuring both the TOF and 2D position simultaneously. In this situation, the 2D position yields the radius and azimuthal (in-plane) angle whereas the TOF is directly related to the polar (elevation or out-of-plane) angle. Gated time slicing[30] and double exposure methods[31] have been employed for 3D ion VMI. In practice this is much more difficult to achieve for electrons. Their light mass means that even 1eV electrons are travelling at 6×10^5m/s, which under the required field strengths, results in an arrival time spread on the order of tens of nanoseconds. Nanosecond resolution is easily achievable when measuring the TOF only, but 2D position is typically measured with CCD or CMOS cameras which have millisecond scale frame rates. Discerning which TOF corresponds with which 2D position for several electron hits in a single image becomes ambiguous. Detectors such as delay line anodes map 2D position to a set of delays that can be measured on the nanosecond time scale but can only practically measure a single electron per laser event[32]. This necessitates very low laser powers

such that data collection over many hours is required for a good signal to noise ratio.

Achieving full 3D VMI capabilities at multiple electrons per laser shot rates has recently been demonstrated[33,34]. The technique utilizes statistical variations in the MCP electron gain in order to make correlations between the TOF and 2D position measurements. As an MCP relies on a secondary electron avalanche to amplify a single particle hit into millions of electrons, the total number of secondary electrons emitted (the electron gain) has an inherent distribution, called the pulse height distribution. Since both the brightness of a spot on the phosphor screen and the total charge (determined independently) are both measures of the number of electrons emitted from the MCP, a single electron detection event will have a correlated brightness and charge. The 2D position can then be imaged by a fast CMOS camera whose framerate matches the laser repetition rate, whereas the TOF can be measured with a fast digitizer or oscilloscope coupled to the phosphor screen through a pickoff capacitor. If it is from the same electron event, the total charge as measured by phosphorescence intensity and that by integrating the voltage waveform on the oscilloscope will be correlated. Thus, a charge correlation algorithm can be used to simultaneously determine the TOF and 2D position for each electron input hit. A challenge of this technique is the TOF resolution, which is determined by the arrival time spread of the electrons at the detector. In standard VMI, the time spread is typically minimized to improve mapping of complimentary angle forward- and backward-moving electrons (i.e. the points on a sphere which would overlap in a 2D projection) to the same point on the detector. 3D VMI must maintain velocity mapping while maximizing the turn-around-time spread for greater resolution. The 3D VMI capability and its corresponding TOF resolution is another main design consideration for the new spectrometer.

Time-of-flight mass spectrometry is another feature we wish to implement. When working with molecular beams it is important to avoid cluster formation. Molecular clusters are essentially different molecules than their constituents and can have dramatic effects on what

is measured in the photoelectron spectrum. The dramatic cooling upon supersonic expansion from a pulsed valve can lead to van der Waals bonding between neutral molecules. Different pulsed valve conditions as well as seed gas concentration have an effect on their formation. Using mass spectrometry to diagnose the molecular beam in-situ would be of great advantage. Mass spectrometry can also be used in a time-resolved fashion to determine rates of product ion formation in photodissociation experiments[35]. In principle any flight tube with controllable electrode potentials, such as a VMI spectrometer, can be used to measure ion TOF with varying mass resolutions. For the relatively low molecular masses we are interested in, increasing mass resolution only matters to a certain point. For molecular beam diagnostics and potential time-resolved experiments, time-of-flight mass spectrometry capabilities with a sufficiently high mass resolution is of interest for the new spectrometer.

During an ionization event, many processes can take place. After excitation, the molecule can ionize directly, autoionize from superexcited Rydberg states, dissociate into ionic and neutral fragments, or dissociate into neutral and superexcited fragments which may further autoionize. The ability to distinguish which electrons correlate with which ions would be very beneficial for determining ionization dynamics and reaction mechanisms. True coincidence methods exist which measure time-resolved 1D-3D velocity distributions (TOF, 2D position, or both combined) of both electrons and ions simultaneously[36–38]. They are, however, limited to an average of much less than one electron per laser shot in order to avoid false coincidences. Covariance measurements are a significant improvement on this technique, allowing for multiple events per laser shot, provided the probability of two particles arriving at the same time/location is negligibly small[39,40]. It determines the electron-ion pairs by leveraging statistical correlations between electrons and ions from the same underlying process. Implementing covariance techniques will be a feature worth considering for the new spectrometer.

To summarize, the main design goals for the new spectrometer are:

- High energy resolution (2D position) VMI
- maximizing the turn-around-time spread for 3D VMI
- Ion time-of-flight mass spectrometry capabilities with modest mass resolution
- Electron VMI – ion TOF covariance capabilities

Different spectrometer designs, simulations of their performance with respect to these categories, and the design we chose will be discussed in the rest of this chapter.

2.3 Simulation

The SIMION charged particle optics simulation software was used to determine different criteria such as energy resolution, electron time spread, and ion mass resolution, for several different VMI designs. Two levels of simulation were performed: a faster 2D method where a small number of electron trajectories were sampled, and a full 3D Monte Carlo simulation sampling many trajectories. The faster method was used to quickly determine the merits of different designs while the Monte Carlo method was used to better estimate certain spectrometer capabilities of the designs. Note that all electrodes in simulations are cylindrically symmetric unless otherwise stated. The following sections will define the resolution criteria used and the assumptions made at both levels of simulation.

2.3.1 Axes and angle definitions

Figure 2.1 shows the axis convention which will be used for the rest of this chapter. The z-axis is the TOF axis or the cylinder axis along the direction from the interaction region to the detector. The y-axis is the laser axis. Depending on the spectrometer design, the molecular beam travels either along the z-axis or the x-axis. The elevation (polar) angle theta is defined as counter-clockwise about the positive x-axis starting from the positive z-axis. The azimuthal (in-plane) angle is defined as clockwise about the z-axis starting from

the positive x-axis. The origin is defined as the center of the interaction region.

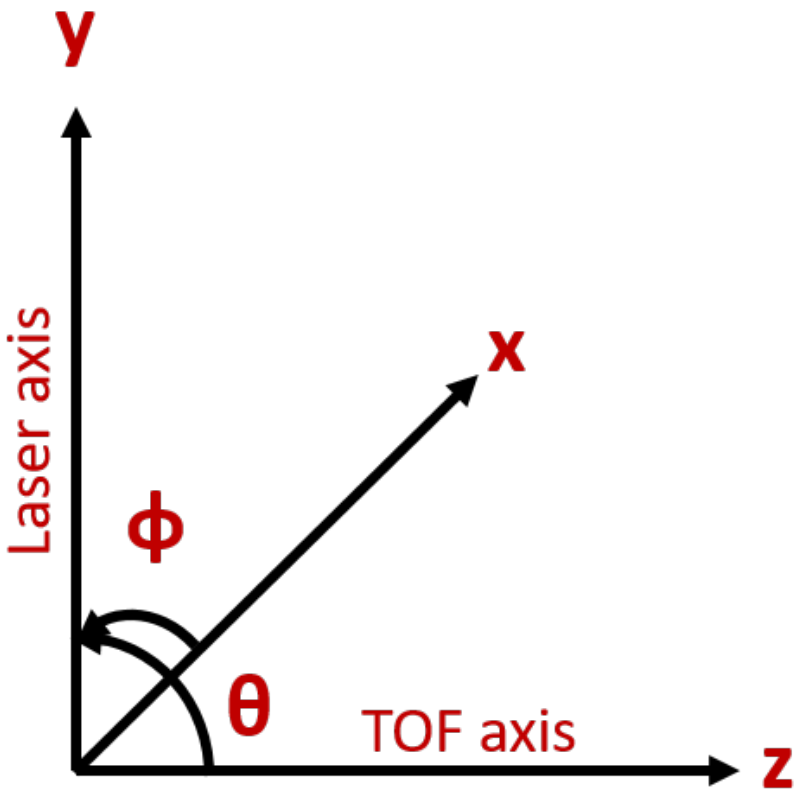

Figure 2.1: Axis convention used for all simulations in this chapter. The molecular beam axis is either along the x-axis or the z-axis, depending on the spectrometer design. Theta is the elevation (polar) angle and phi is the azimuthal angle.

2.3.2 The choice of molecular beam axis

The molecular beam is a supersonic gas jet of a small percentage of target molecules seeded in an inert gas, typically Helium. It is usually generated by a pulsed valve and skimmed by the small aperture of a molecular beam skimmer before entering the interaction region. A good supersonic expansion (e.g. Mach 10) of heavy molecules seeded in helium will have a parallel speed on the order of 1800m/s with a velocity spread of 5% or 90m/s (FWHM) along the direction of travel[41]. Perpendicular to the molecular beam, the velocity spread at

the interaction region is negligible due to its very small subtended solid angle. For recoiling photoelectrons, the molecular beam centre of mass velocity has little effect on their resolution. A 0.01eV electron travels at 6×10^4m/s, with higher energy electrons travelling much faster, making the center of mass velocity irrelevant.

The beam velocity cannot be ignored for ions, however, as their much heavier mass means their recoil speeds are comparable to that of the center of mass. This means that the center of mass velocity imparted by the molecular beam will affect the ion trajectories. As stated in section axes, the molecular beam axis can be aligned either parallel (z-axis) or perpendicular (x-axis) to the TOF axis. Each choice has its own advantages and disadvantages. Aligning the beam parallel to the TOF axis is beneficial for TOF mass spectrometry because the lack of perpendicular velocity means that ion trajectories are not offset at the detector. Only the recoil velocity of photofragments from a photodissociation event will have a perpendicular velocity component. The major downsides are that the velocity spread along the TOF axis will blur the TOF resolution for mass spectrometry and that the molecular beam is flying directly into the detector. This can cause premature degradation of the MCP as well as an increase in the background gas density in the VMI chamber which ideally is pumped out after each laser shot. In contrast, a molecular beam along the x-axis can pass directly through the interaction region and into a turbo molecular pump, lowering the background gas in the VMI chamber. The downsides, as alluded to earlier, are an x-axis offset in the ion trajectories due to the beam velocity and a blurring effect due to their velocity spread. As will be shown in section 2.12, the perpendicular molecular beam geometry is more beneficial in our case, due to the extremely narrow transverse velocity spread (along the TOF axis), which leads to greatly improved mass resolution.

2.3.3 The interaction region

The interaction region is defined as the finite volume occupied by the intersection of the laser focal volume with the skimmed gas jet. Ideally, the interaction region would be of infinitesimal volume, modelled as a point source. In practice both the laser focus and the gas jet have finite size, which has a blurring effect on the final image. A 200nm laser pulse with a 5mm spot size focussed by a 2m focal length spherical mirror has a $100\mu m$ waist at the focus with a Rayleigh range of 4cm. A well formed molecular beam from a pulsed valve passed through a 1mm skimmer aperture 30cm from both the valve and the interaction region will produce a cylinder with roughly a 2mm diameter. The intersection of these two volumes is therefore approximately a 2mm long by 0.1mm diameter cylinder. In the 2D simulations, the interaction region was sampled by 3 rows of 3 points defining a rectangle of dimension 2mm x 0.1mm, as shown in Fig. 2.2. In the 3D simulations the interaction region was sampled as a normal (Gaussian) distribution in the x and z coordinates with a 0.1mm $1/e^2$ width, and a uniform distribution in y over the 2mm length. A normal distribution in x and z was chosen because of the well defined Gaussian profile of a focussed laser. The uniform distribution in y represents the worst case scenario, as the density profile of a low concentration heavier seed gas tends to be hydrodynamically focussed in a supersonic gas jet expansion. Figure 2.3 shows a y-z projection of the 3D interaction region sampling.

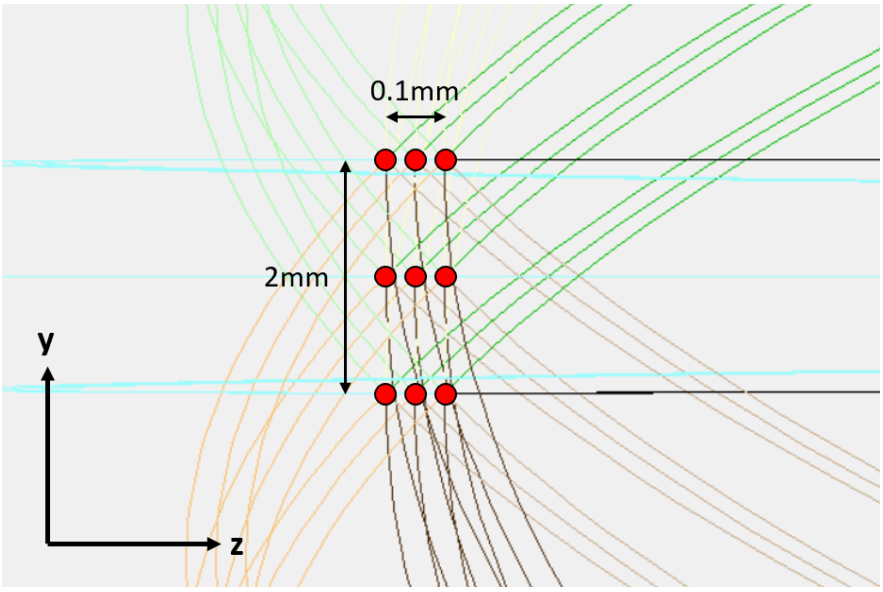

Figure 2.2: Interaction region sampled by 9 points in 2D simulations, shown as red circles. The different coloured lines represent different electron trajectories.

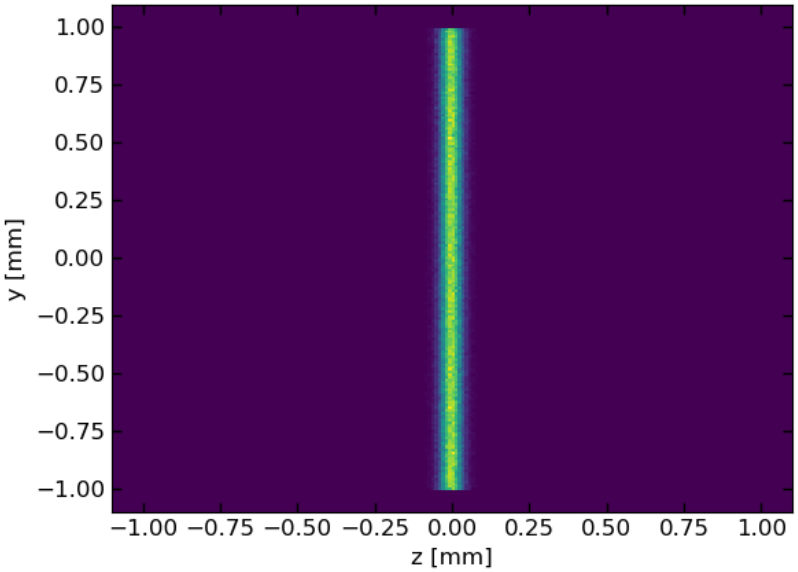

Figure 2.3: x-y projection heat map of the 3D interaction region sampling. The distribution is Gaussian in x/z with a $1/e^2$ width of 0.1mm and uniform in y over 2mm.

2.3.4 Energy resolution

Typically, VMI energy resolution is measured as a relative uncertainty $\Delta E/E$. In order to calculate $\Delta E/E$ we need the relationship between energy and position on the detector. In a spatially uniform acceleration field pointing in the z direction, there are no forces acting on the electrons in the x-y plane. This means that the final x-y position on the detector is directly proportional to its initial velocity. In VMI, the velocity mapping is achieved by curved field lines, which complicates this relation. However, to a good approximation the direct relationship can be used. This approximation will be explored in more detail in later simulations. Since kinetic energy is proportional to velocity squared, we can write the energy as

$$E = kR^2, \tag{2.1}$$

where R is the radial position on the detector and k is a proportionality constant. The energy spread is

$$\Delta E = \frac{dE}{dR}\Delta R = 2kR\Delta R,$$

and dividing by 2.1 gives the relative uncertainty

$$\frac{\Delta E}{E} = 2\frac{\Delta R}{R}. \tag{2.2}$$

The velocity mapping fields are set in such a way that the best focussing occurs at the largest radius of the detector. The relative uncertainty is then smallest at the largest radius and increases as R approaches zero. In other words, the electron focal length, and hence the energy resolution, is energy dependent, analogous to the optical phenomenon of chromatic aberration. Figure 2.4 shows an improperly focussed VMI simulation to illustrate the chromatic aberration effect. Trajectories for 6 different electron energies from 0 to 10eV in steps of 2eV ejected perpendicular to the TOF axis are shown. The red crosses mark the approximate

focal planes for each kinetic energy, making the aberration very apparent.

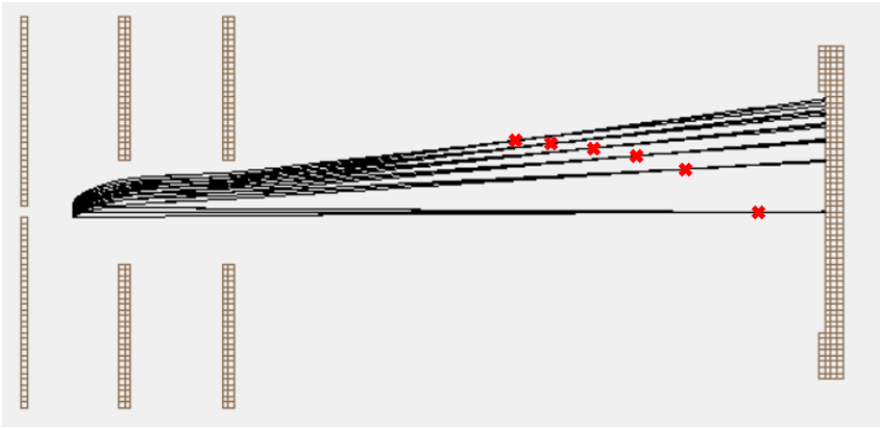

Figure 2.4: VMI simulation of electron kinetic energies from 0 and 10eV in steps of 2eV. Incorrect voltage settings were used to highlight the chromatic aberration effect. Red crosses mark the approximate focal planes for each energy.

VMI resolution is thus typically reported as the ΔR spread at the largest radius on the detector of electrons born in a finite interaction region ejected perpendicular to the TOF axis. For clarity, a schematic is shown in Fig. 2.5, showing electrons with initial velocity v_0 following trajectories (black lines) towards the detector with a spread ΔR at a radius R from the center. Note that the VMI potentials were intentionally detuned in this figure to illustrate the ΔR spread. With proper focussing conditions the electron trajectories converge to a much smaller ΔR.

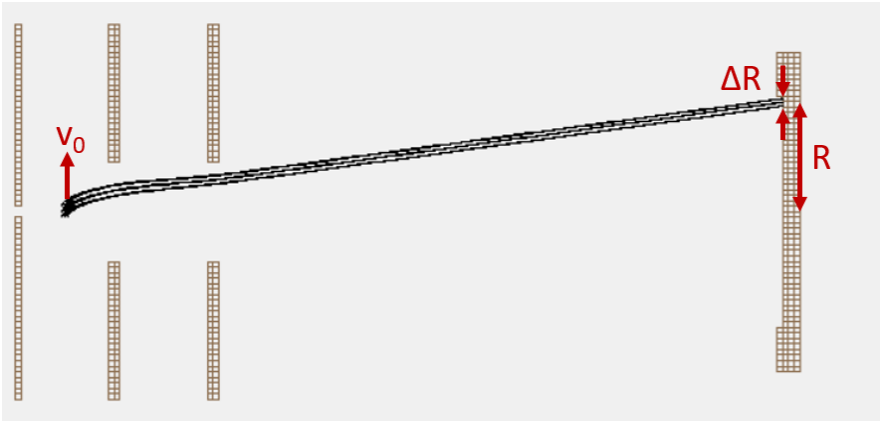

Figure 2.5: Schematic of how VMI energy resolution is calculated in simulation. Electrons with initial velocity v_0 follow trajectories (black lines) towards the detector with a spread ΔR at a radius R from the center.

In our 2D simulations, we will follow this precedent, calculating ΔR as the difference between the smallest and largest radii electron hits on the detector for a given kinetic energy ejected perpendicular to the TOF axis, and calculating R as the average radius of all electrons of the same kinetic energy. For the 3D simulations, a uniform spherical distribution (Y_0^0) of thousands of electrons at several discrete kinetic energies was flown to accurately recreate an experimental image (For details see appendix A). The image was then Abel inverted[42] and fit with Gaussians to determine the peak widths and positions. The full width at half maximum (FWHM) was taken as the ΔR value and the center of the Gaussian was used as the R value.

There are other effects which affect the overall energy resolution, such as MCP spot size broadening and surface imperfections of the electrodes which are not considered in these simulations. The simulations are therefore an estimate of the pure instrument response function under ideal conditions.

2.3.5 Time spread resolution

The electron time spread resolution was characterized by the arrival time difference between the first and last electrons to hit the detector. What determines the time spread is the field strength in the interaction region, which can be explained from first principles. Consider two electrons born at the same point in a constant electric field that is pushing them towards a detector. One is initially moving with speed v_0 towards the detector while the other is moving in the opposite direction with speed $-v_0$. The electron initially moving away from the detector will be accelerated by the field in the opposite direction, turn around and reach a speed of v_0 exactly at its starting point. Since both electrons have a speed v_0 at the same location, they will take equal time to travel the same distance to the detector. The only difference in flight time then is the turn around time of the electron travelling away from the detector. The turn around time is directly related to the field strength and therefore

minimizing the field strength in the interaction region will increase the time spread. There is a trade-off, however, that in order to collect electrons flying in all directions the fields must be strong enough to push electrons towards the detector before they expand too much and collide with the edges of the spectrometer. There are also constraints on the fields required to maintain VMI conditions.

The longer the time spread, the more TOF bins can be collected and the higher the TOF resolution. The actual size of the bins depends on many things, including the MCP geometry, the pickoff capacitor, the RF cable length, the preamplifier bandwidth, and the oscilloscope resolution, which is beyond the scope of this thesis, but from our preliminary results we estimate the TOF resolution to be <100ps. The goal of these simulations is then to measure and maximize the time spread as much as possible while maintaining VMI conditions.

2.3.6 Mass resolution

In a constant electric field, the equation of motion of an ion with mass m and charge q is

$$\Delta z = v_0 t + \frac{1}{2}\frac{qE}{m}t^2,$$

where Δz is the distance travelled, v_0 is the initial velocity in the z direction and E is the electric field. Assuming $v_0 = 0$, the TOF of the ion is

$$t = \sqrt{2\Delta z \frac{m}{qE}}.$$

Since Δz and E are constants, the TOF is proportional to the square root of m/q, which means that the ion TOF difference t_{m+1}–t_m becomes smaller as the mass m increases. There are two assumptions made here: a constant electric field and zero initial velocity. In a VMI spectrometer, either one or the other of these assumptions does not hold, depending on the molecular beam geometry. If the molecular beam axis is along (parallel) the TOF

axis, a constant electric field is a good approximation as all ions will travel the same path directly along the TOF axis. However, the initial velocity along the TOF axis now has a spread dictated by the molecular beam speed ratio (e.g. 5% at 1800m/s). In the case of a perpendicular molecular beam, the opposite is true. The velocity spread along the TOF axis is now practically zero, but the perpendicular velocity spread means that ions will not travel the same paths. Since VMI has curved field lines, the constant field approximation fails. Simulations for both molecular beam geometries were performed (where possible) to investigate the differences between the two.

The mass resolution is defined as the maximum atomic mass m that can be separated from its neighbours $m+1$ and $m-1$. A mass resolution of 100amu means the 100amu peak is separable from its neighbours at 99amu and 101amu, but 101amu is not separable from 102amu. As we are mostly interested in smaller polyatomic molecules, we will qualify the effective mass resolution as sufficient above 300amu.

2.4 VMI spectrometer design basics

The following sections will introduce the 3 plate VMI spectrometer as well as the improvements of the existing VMI spectrometer at the National Research Council.

2.4.1 3 plate VMI spectrometer

The original VMI spectrometer, designed by Eppink and Parker, consists of a three-plate open ring electrostatic lens system. The three plates are named the repeller, extractor and ground electrodes. Figure 2.6 shows a SIMION simulation of the Eppink and Parker 3 plate design where the repeller, extractor and ground electrodes are labelled as R, E, and G, respectively, and the detector is labelled D. The red lines in Fig. 2.6 represent equipotential surfaces, and the other coloured lines are the electron trajectories. The curved field lines (perpendicular to the equipotential surfaces) act like a lens that give VMI its focussing capabilities.

The potential applied to the repeller determines the maximum kinetic energy detectable. A higher voltage on the repeller pushes the electrons faster towards the detector, decreasing the time the Newton spheres have to expand which in turn allows higher energy electrons to be imaged. The extractor potential determines the focussing conditions, and the ground plate shields a field free flight region up to the detector. Under VMI conditions, the ratio of extractor to repeller potential is a constant. Thus, the maximum kinetic energy can be adjusted by scaling the potentials while maintaining their ratio. In the case below, it is 0.715, close to the experimental value of 0.71 reported by Eppink and Parker.

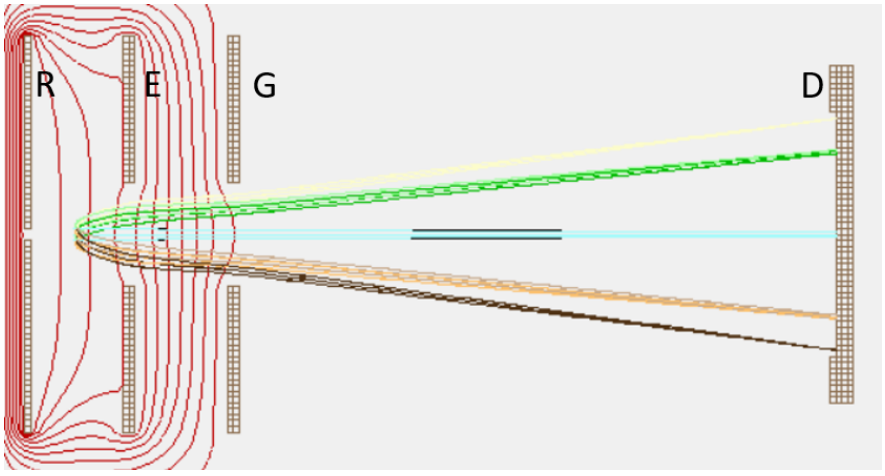

Figure 2.6: SIMION simulation of a 3 plate VMI spectrometer. The three electrodes are labelled as R: repeller, E: extractor and G: ground. The detector is labelled D. The red lines indicate equipotential surfaces. The other different coloured lines are 5eV electron trajectories ejected from the interaction region in 45 degree angle increments.

VMI is a large improvement over previous grid electrode imaging systems. The grid designs suffer from three major issues: transmission reduction due to electrons hitting the grids, large trajectory deflections due to electrons flying very close to the grid wires (which acts as a fish-eye lens), and blurring due to both the local field distortions around the grid and the finite volume of the interaction region. In contrast, the open lens design completely removes grid transmission and distortion effects. With the correct voltage settings, blurring effects are reduced to well below the size of the interaction region. To illustrate these differences,

Fig. 2.7 shows a simulation of the 3 plate VMI design with grids installed, to be compared with Fig. 2.6. In the grid design, the fields are flat which means there is no steering forces in the x-y direction and hence no focussing ability. The velocity distribution is imaged onto the detector and magnified by the distance travelled but is also convoluted with the volume of the interaction region. The curved field lines of the VMI design greatly reduce the effects of the interaction region volume by focussing electrons of the same initial velocity. Figure 2.8 shows 3D Monte-Carlo simulated images for (a) the three plate VMI design and (b) the grid design. Uniform spherical distributions of 1, 5 and 10eV electrons were flown that resulted in three distinct rings in the images. The blurring effect is abundantly clear for the grid design but is almost absent in the 3 plate VMI design. There is still a slight asymmetry visible in the central ring of Fig. 2.8 (the ring is slightly brighter on the sides than the top/bottom), indicating the volume of the interaction region is still not perfectly compensated.

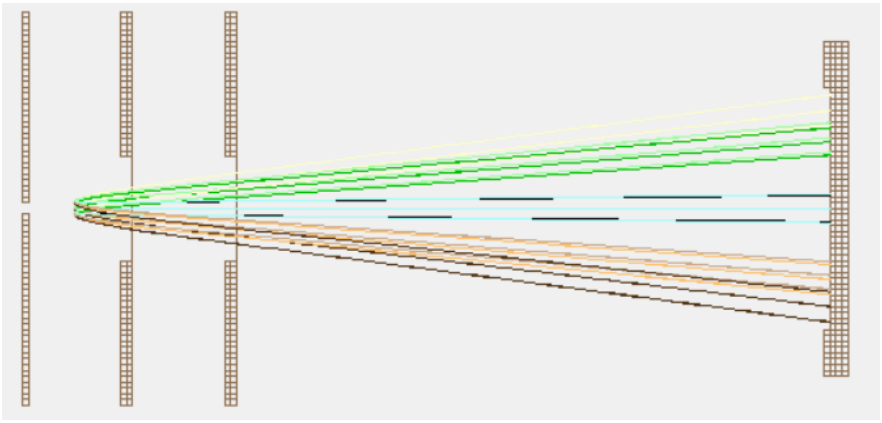

Figure 2.7: SIMION simulation of a 3 plate spectrometer modified with grids instead of open ring VMI electrodes.

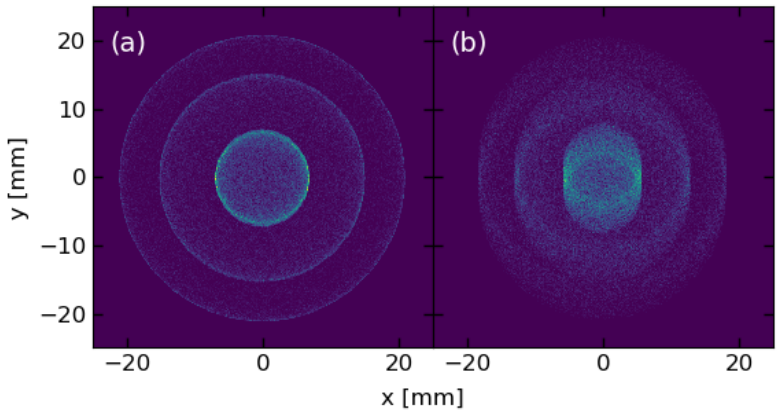

Figure 2.8: Comparison between simulated (non-inverted) images of (a) the three plate VMI design and (b) the grid design for uniform spherical distributions of 1, 5 and 10eV electrons. The grid design suffers from a large blurring effect due to the volume of the interaction region. Note the slight asymmetry in the central ring of the VMI image, indicating the volume of the interaction region still has a small effect.

2.4.2 Thick lens VMI spectrometer

Many resolution improvements to the 3 plate VMI spectrometer have been made, including the addition of refocussing einzel lenses[43], the shaping of the electrodes to tailor the field curvature[44], improvements for collection of slow[24] and fast electrons[25], and reduction of stray electrons from scattered light[45]. All these designs incorporate several more electrodes than just the standard 3 plates. The addition of these extra electrodes, called a thick lens spectrometer, allows for a softer focussing potential which increases the overall resolution and reduces chromatic aberration. While not often discussed, it also has the benefit of increasing the overall electron time spread, which is especially important for 3D VMI.

The VMI spectrometer currently in Femtolab 4 at the National Research Council, designed by Dr. Iain Wilkinson, is of this type. Figure 2.9 shows a SIMION simulation of the electrode

stack, with the electrodes and the wiring diagram labelled. A large issue with the 3 plate design is stray electrons caused by scattered light. The photon energies of the UV/VUV pulses used in our experiments are above the work function of the electrode metal so any incident light on the electrodes will generate electrons, with a typical photoelectron efficiency of about 1%. To reduce stray electrons the repeller plate was replaced with two electrically connected open ring repeller electrodes, labelled R, and a repeller grid further back from the interaction region, labelled RG. There is a small hole in the repeller grid where the molecular beam enters the spectrometer. With R and RG held at almost the same potential, this configuration mimics a flat repeller plate, while moving the large surface area of the grid much further away from the interaction region where scattered light is less likely to reach. The repeller grid is also held at a slightly more positive potential such that electrons ejected from its surface are pushed back towards the grid and away from the detector. The light port electrode, labelled LP, also minimizes stray electrons by separating the repeller and extractor electrodes such that their protruding rings are farther from the interaction region. The light port electrode has 2cm holes along the laser axis, providing sufficient clearance for the laser. The extractor, labelled E, is the thick lens element comprised of a set of 8 electrodes, followed by the ground electrode G which has a grid right before the detector. The spectrometer is controlled by four potentials: V_{RG}, V_R, V_E and V_G. V_{RG} independently controls the repeller grid potential. The two open ring repeller electrodes are controlled by V_R. The light port is set as the midpoint between V_R and V_E by a resistive voltage divider. The extractor electrodes that comprise the thick lens are set by a linearly stepped resistive voltage divider from V_E to V_G. The ground electrode potential V_G is used to change the offset potential between the grid and the MCP, to ensure the electrons are accelerated to 300-500eV for maximum detection efficiency by the MCP[46].

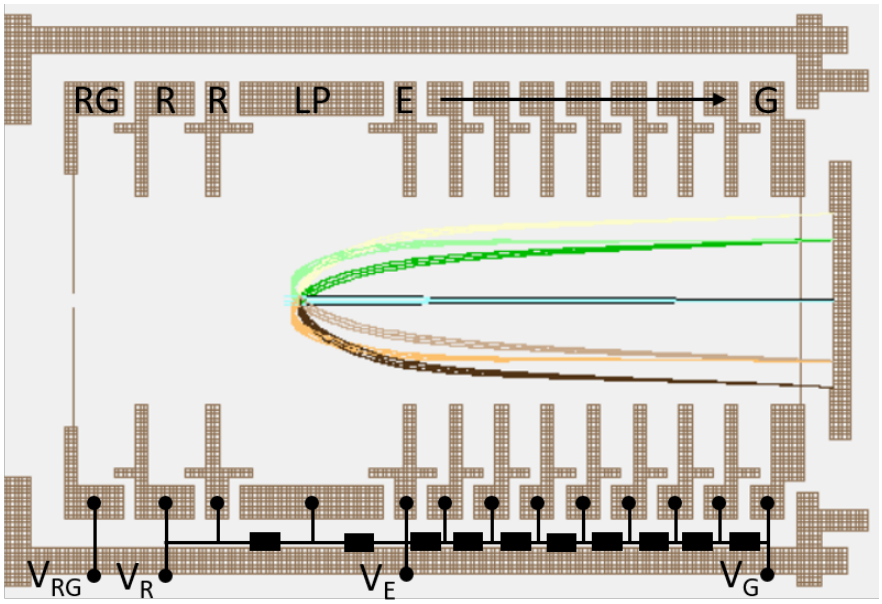

Figure 2.9: SIMION simulation of the thick lens VMI spectrometer in Femtolab 4 at the NRC. RG: repeller grid, R: repeller, LP: light port, E: extractor, G: ground. There are four adjustable potentials: V_RG, V_R, V_E and V_G. See text for details.

2.5 New spectrometer design options

The new spectrometer design options were heavily based on the NRC VMI spectrometer. Dr. Wilkinson was kind enough to provide three initial starting points for our analysis, in relation to our design goals listed in section VMI goals. In this section, the three design options will be presented along with explanations of their features and their performance in simulation will be evaluated. The 3 plate design will also be evaluated as a benchmark. Note that the spectrometer dimensions listed are only to give a sense of the scale of each spectrometer. They are not listed for accurate mechanical reproduction.

2.5.1 Design #0 – 3 plate benchmark

The 3 plate VMI spectrometer used as a benchmark is a copy similar to the design used by Eppink and Parker, with the main difference being the distance from the interaction region to the detector. In our case the distance matches the NRC spectrometer at 130mm, whereas

Eppink and Parker placed their detector at a distance of 360mm. The plates are 2mm thick with a 20mm internal diameter (ID) and are spaced 16mm apart. The detector is 40mm in diameter, situated 103mm from the last electrode. Figure 2.10 shows the 3 plate design used with dimensions in mm.

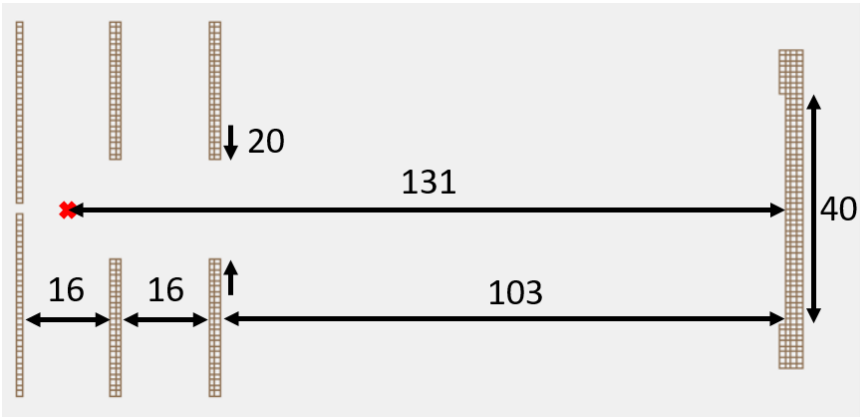

Figure 2.10: Dimensions of the 3 plate spectrometer used in SIMION simulations. The red cross indicates the interaction region. All units are in mm.

2.5.2 Design #1 – NRC copy

The first design we are considering is a copy of the NRC design. The question then becomes why remake the same design? "If it ain't broke don't fix it". The NRC VMI spectrometer was built on a tight budget and some of the machining tolerances suffered as a result. A set of concentric cones on the laser entrance and exit ports, called light baffles, were installed to reduce scatter. These baffles work very well, however, the entrance and exit sets are not concentric, making laser alignment difficult. The relay imaging system has a long focal length in vacuum lens that is difficult to align and impossible to adjust once the chamber is pumped down. The molecular beam is along the TOF axis, increasing the background gas to be pumped out and reducing the lifetime of the MCP. In short, there are many areas to improve on this design that do not involve the VMI electrode stack directly.

Figure 2.11 shows the NRC spectrometer with dimensions labelled in mm. It has a 40mm diameter detector placed 129mm from the center of the interaction region. All of the

electrostatic lenses are 3mm thick and have an ID of 50mm. The repeller electrodes are separated by 14mm face to face. The extractor electrodes are separated by 8mm face to face. The repeller and extractor are separated by 44mm.

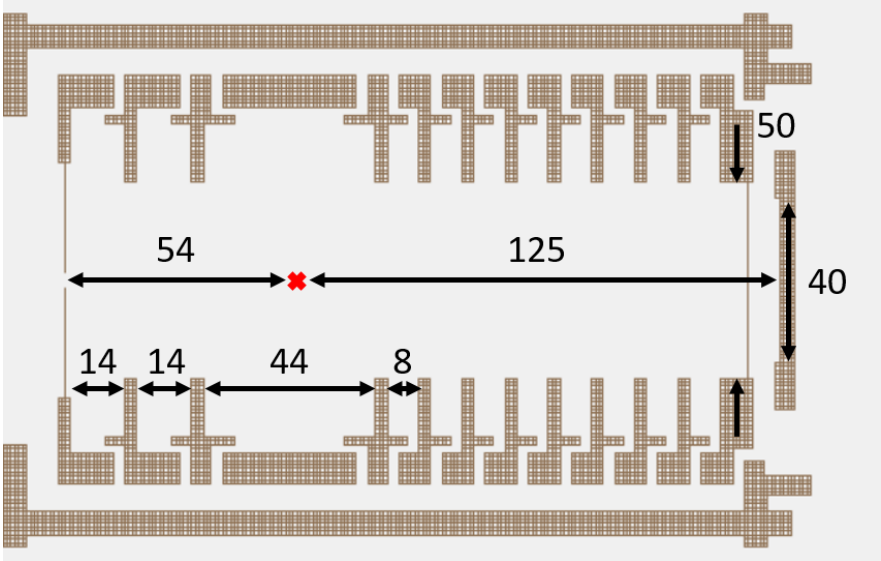

Figure 2.11: Dimensions of the NRC spectrometer used in SIMION simulations. The red cross indicates the interaction region. All units are in mm.

2.5.3 Design #2 – 20 lens VMI spectrometer

This option takes the NRC VMI and extends the thick lens to a total of 20 electrodes and expands the internal diameter of the electrodes to 84mm to accommodate a larger 80mm detector. Figure 2.12 shows the dimensions of the 20 lens spectrometer. The idea is to increase the flight length and size of the spectrometer to allow the electrons to spread out more for a larger TOF spread, while also increasing the 2D resolution with a larger detector. The increased flight length should also increase the mass resolution.

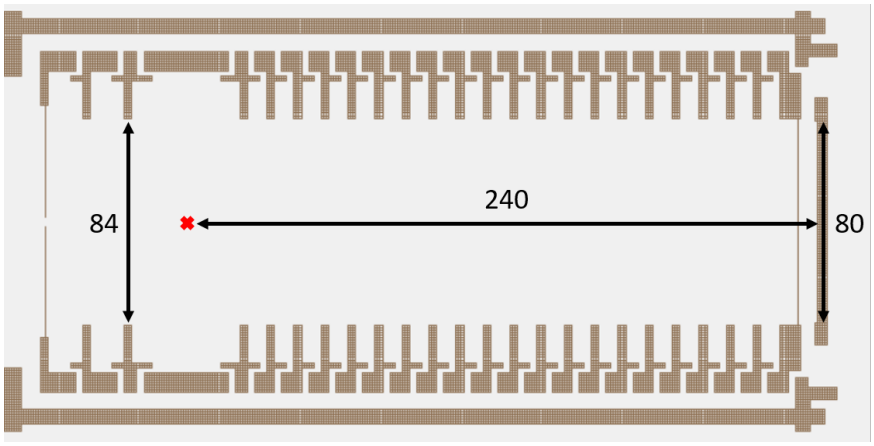

Figure 2.12: Dimensions of the 20 lens spectrometer used in SIMION simulations. The red cross indicates the interaction region. All units are in mm.

The 20 lens design has a few disadvantages, most notably in the cost. The larger 80mm MCP is much more expensive than the 40mm version. The precision machining of the extra electrodes will be more costly as well. A larger ID vacuum chamber will be required to house the larger electrode stack. The larger diameter of the spectrometer will also have an effect on its functionality. If the molecular beam is along the x-axis, the skimmer will be positioned further away from the interaction region due to the larger diameter electrodes. This will increase the molecular beam size and (quadratically) decrease its density in the interaction region, resulting in less overall signal. The magnitude of this effect is likely minor, however, it is difficult to assess. Overall, the 20 lens design would have to provide a significant improvement in energy resolution, electron time-spread, and ion mass resolution to justify the cost. As will be seen in the rest of this chapter, only slight improvements were shown in simulations and therefore we opted not to follow through with this design.

2.5.4 Design #3 – PEPICO electron VMI ion TOF spectrometer

The third option is to copy the NRC VMI for electrons while adding a flight tube for ions in the opposite direction to permit photoelectron-photoion coincidence spectroscopy (PEPICO). The design is shown in Fig. 2.13. For the electron VMI side, the spectrometer is the same

as the NRC design, except the ID of the lenses has been widened to 60mm instead of 50mm. This was done to increase the distance between the electrons and the edges of the lenses to reduce the effects of machining imperfections on the electron trajectories. The ion side now has two grids G_1 (previously the repeller grid) and G_2 and a 560mm long flight tube that make up an approximate Wiley-Mclaren TOF mass spectrometer[47]. The flight tube and grid spacing dimensions were chosen to satisfy second-order space focussing conditions, which is a geometric relationship that minimizes the effects of the finite volume interaction region. A succinct review of Wiley-McLaren mass spectrometers and the mathematics involved can be found in reference[48]. As both TOF directions are occupied, the molecular beam lies along the x-axis in this case. Two parallel deflector plates (not cylindrically symmetric), labelled DP, are placed along the molecular beam axis to counteract the initial parent centre of mass velocity of the heavy ion fragments. A second 40mm MCP detector is placed at the end of the flight tube to determine the ion TOFs. The clear advantage of this design is the ability to do covariance measurements. It also allows for individual optimization of electrode potentials to operate in "ion mass spectrometry mode" or "electron VMI mode". In terms of machining costs, it is not much more expensive than the NRC design as only two grids and a flight tube have to be added. The second MCP detector will double that price but will likely be less than a single 80mm detector. Overall, its versatility makes it a very promising option, and we decided this design was best suited for our purposes.

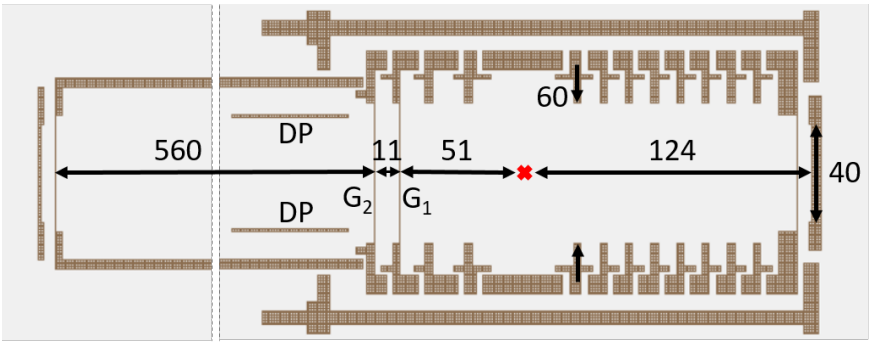

Figure 2.13: Dimensions of the PEPICO spectrometer used in SIMION simulations. DP: deflector plate, G_1/G_2: grids for ion TOF spectrometer. The red cross indicates the interaction region. All units are in mm.

2.6 Optimization

The optimized voltages for each spectrometer in VMI and mass spectrometry mode are listed in Appendix B. The electrode potentials for VMI were roughly optimized using 2D simulations and a built-in SIMION simplex optimizer routine (Nelder-Mead method back-end). As the NRC design was already close to optimized, its potentials were used as a starting point. The cost function used was

$$F(V) = \sum_i [R(E_i, V) - R_{NRC}(E_i)]^2,$$

where $R(E_i, V)$ is the radial position of an electron bunch with energy E_i and potentials V, and $R_{NRC}(E_i)$ were the close to optimized radial positions of the electrons from the NRC design. Electrode potentials were not adjusted individually; the system was parameterized by V_{RG}, V_R, V_E, and V_G, as shown in Fig. 2.9. Step sizes of 5V were taken with the simplex optimizer and fine adjustments were made by hand. The general procedure is to set the repeller potential such that the desired maximum kinetic energy electrons are hitting close to the edge of the detector, then adjust the extractor for the best focussing at the maximum kinetic energy. The maximum radius is coupled to V_R and V_E thus it is an iterative process to optimize the two. Small improvements to $\Delta E/E$ were made by slight adjustments to the repeller grid and the light port electrode as well. To give an idea of the sensitivity of the

resolution with respect to the extractor potential, Fig. 2.14 shows the extractor voltage V_E dependence of $\Delta E/E$ with the other parameters fixed for the NRC design. We see that each kinetic energy comes into focus at a different value of V_E, as illustrated by the vertex of each line. The slope on either side of the minimum of the 5eV line is roughly 0.13%/Volt. The mass spectrometry optimization was performed by hand using the Wiley-McLaren conditions as a starting point[48].

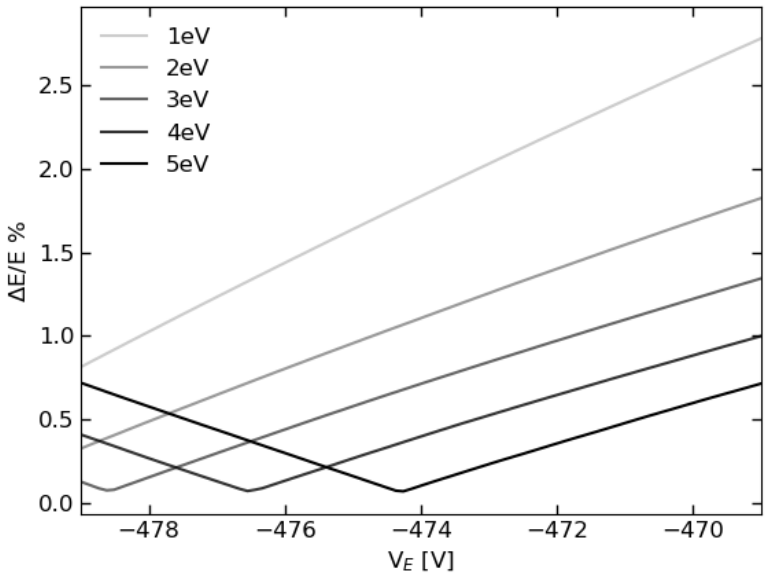

Figure 2.14: dE/E resolution dependence on the extractor voltage V_E for the NRC spectrometer design at 5eV settings. Each kinetic energy comes to a focus at a different value of V_E, as noted by the vertex of each line. $V_{RG} = 516.7$V, $V_R = 558.1$V, $V_G = 0$.

2.7 Energy resolution – 2D simulations

For each spectrometer design, the VMI voltages were optimized to focus 5eV electrons at the maximum detector radius, and the resolutions of 1, 2, 3, 4 and 5eV electrons, all flown at settings optimized for collection of 5eV electrons, were calculated. Figure 2.15 shows the resolution $\Delta E/E$ as a function of electron kinetic energy for each of the 4 designs. The resolution at 5eV of the 3 plate spectrometer is 0.87%, while the other 3 spectrometer designs

converge to a much improved 0.09%.

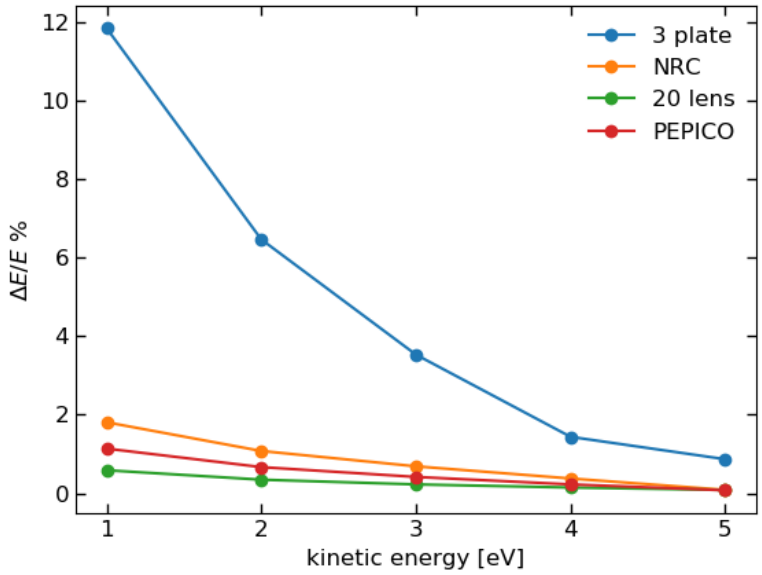

Figure 2.15: Relative energy resolution calculated from 2D simulations for the 4 different designs. Electrons from 1-5eV in steps of 1eV were flown with the spectrometers optimized for 5eV electrons.

The scale of chromatic aberration is easily distinguished in this plot. We see that the 3 plate design once again suffers the most, with a $\Delta E/E$ of nearly 12% at 1eV. The 20 lens design is the clear winner in this category, but the NRC and PEPICO designs are not far behind. It is interesting to note the difference between the NRC and PEPICO designs. At 1eV, the NRC spectrometer fares 0.6% worse than the PEPICO design. One would expect a slight difference in performance because the lensing effect is directly related to the ID of the electrodes (all else being equal), which is slightly larger in the PEPICO design. This effect could possibly be mitigated via optimization of the electrode potentials, however, this was not explored further.

2.8 Energy resolution – 3D simulations

For the 3D simulations, 10^5 electrons per kinetic energy were sampled from a uniform spherical distribution and given an initial position based on the cylindrical interaction region

described in section 2.3.3. The exact same initial distributions were used for each of the spectrometer designs. The resulting detector positions were binned into a 480×480 pixel image to approximate the same image size acquired with a camera. For the 20 lens design, the image was binned to 960×960 pixels to simulate the larger detector size. The raw images were then Abel inverted and the five peaks corresponding to the five kinetic energies were fit with Gaussians to determine their positions and widths. Figure 2.16 shows an example of the fits for the 3 plate design. Due to the resolution of the images and the Abel inversion code, there are only a few points to fit for each peak. With the exception of the 3 plate design, the peak widths are all 1.5 pixels or less. For this reason, the 3D simulations of the energy resolution may be more of an indicator of the limits of the inversion algorithm than of the instrument resolution. It may be instructive to assess the performance of different algorithms with these simulations. We have reproduced code from a different algorithm[49] but it has not been sufficiently tested at the time of writing this thesis.

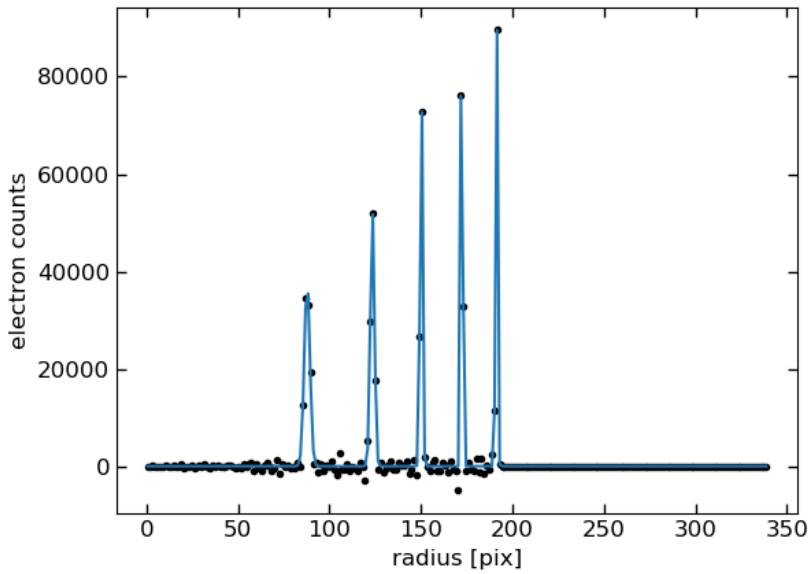

Figure 2.16: Sample fit of the Abel inverted radial component measured in image pixels from the 3D simulation of the 3 plate design. Each peak represents a different electron kinetic energy release from 1-5eV.

Figure 2.17 shows the energy resolution for the 3D simulations, which appear noisier in this case. The pattern of chromatic aberration is less apparent compared to the 2D simulation, especially for the NRC design. This may be caused by insufficient sampling of the distribution or, as stated earlier, degradation of resolution from the Abel inversion algorithm. The 20 lens design still performs the best at 5eV with a $\Delta E/E$ of 0.48%, the NRC and PEPICO designs are tied at 0.85% and the 3 plate design is last at 1.3%. The NRC design has a relatively flat response indicating low chromatic aberration whereas the 20 lens and PEPICO designs have a jump between 2 and 3 eV. The 3 plate and the PEPICO designs show their best resolution at 4eV instead of 5eV, which could indicate improper focussing.

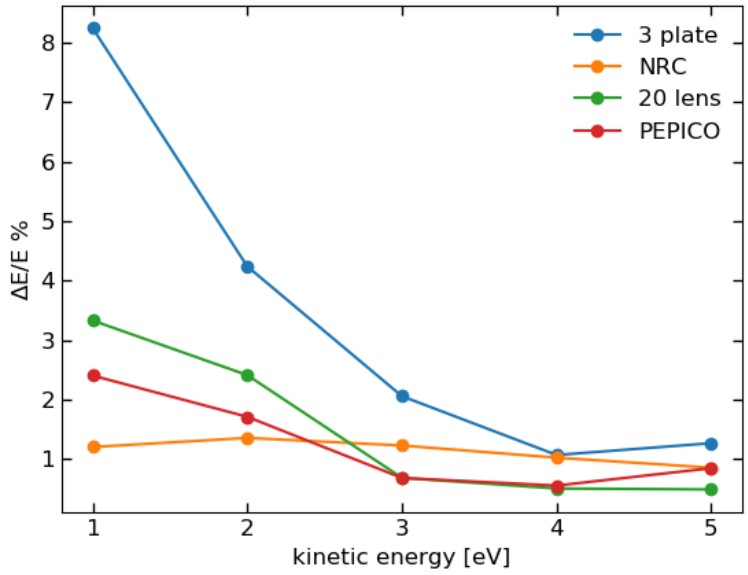

Figure 2.17: Relative energy resolution calculated from 3D simulations for the 4 different designs. Electrons from 1-5eV in steps of 1eV were sampled from a uniform spherical distribution with the spectrometers optimized for 5eV electrons. The resulting images were then Abel inverted and fit with gaussians. The FWHM was taken as the ΔR spread.

Overall, the conclusions drawn about the energy resolution from the 3D simulations cannot be uncoupled from the inversion algorithm issues discussed above. They do, however, indicate that a better inversion method is required if higher resolution is to be achieved.

More work is required to determine whether the 3D simulation is an accurate description of the energy resolution and therefore the 2D simulations will take precedence here.

2.9 Radius to energy conversion

Exploring the relationship between hit position on the detector and kinetic energy, Fig. 2.18 shows a plot of electron kinetic energy as a function of hit radius from the 2D simulations. The 3 plate, NRC and PEPICO designs lie on top of each other, with almost no discerning between them. The 20 lens is predictably different as it has a larger detector size. As we expect an R^2 dependence, fits to the function

$$E = kR^2 + E_0 \tag{2.3}$$

were performed to test the relationship. To quantify the deviations, the fit residuals weighted by the kinetic energy were calculated as shown in Fig. 2.19. The deviation follows the same trend as the resolution in that the 3plate design performs the worst and the 20 lens design performs the best. The inclusion of the offset E_0 is nonphysical as the kinetic energy should be zero at the center of the detector, however a worse fit is obtained without it. Even still, the residuals have a clear quadratic pattern indicating that a 4^{th} order term is present.

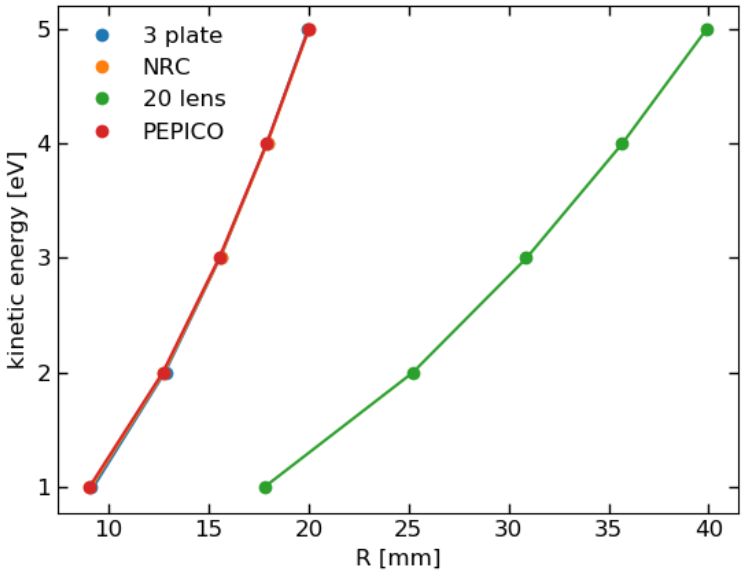

Figure 2.18: Electron kinetic energy as a function of hit radius from the 2D simulations, with quadratic curve fits. The 3 plate, NRC and PEPICO designs are superimposed on each other.

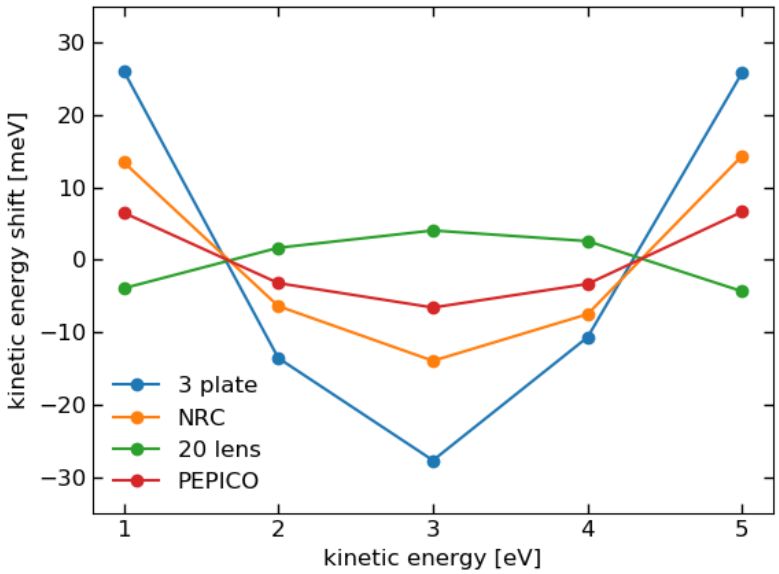

Figure 2.19: Residuals of the linear fits in Fig. 2.18

Taking the NRC design as an example, a deviation of 14meV at 1eV is comparable to the $\Delta E/E$ spread of 18meV at that energy. At 5eV the 14meV shift is three times larger than

the $\Delta E/E$ spread of 4.5meV. As the shifts will contribute to the overall energy resolution if high resolution is to be achieved a better calibration is required. Given the quadratic nature of the residuals, the shift could be improved by adding a second term to equation 2.3

$$E = k_1 R^2 + k_2 R^4 + E_0, \tag{2.4}$$

and using at least four well-known energies of photoelectron emissions for the calibration. Fits of equation 2.4 with E_0 (a) fixed at zero, and (b) floating are shown in Fig. 2.20. The shifts are vastly improved in both cases. In either case, the PEPICO design performed the best with less than 0.25meV shifts at all energies. The E_0 offsets are listed in Table 2.1 for the fits of both equation 2.3 and 2.4. Fitting to equation 2.4 improved the E_0 offsets to below 8meV across the board and less than 1eV for the PEPICO design. The floating E_0 is unsurprisingly superior, however, fixing $E_0 = 0$ has physical meaning and requires one less data point to fit, which is significant as photoelectron emissions with well-defined kinetic energies (to be used for calibration) are hard to come by. As an example, using xenon as the calibration gas with 154.5nm pump and 200nm probe pulses, only three sharp calibration peaks are usable. For more details on such calibrations using xenon see Section 3.5.2.

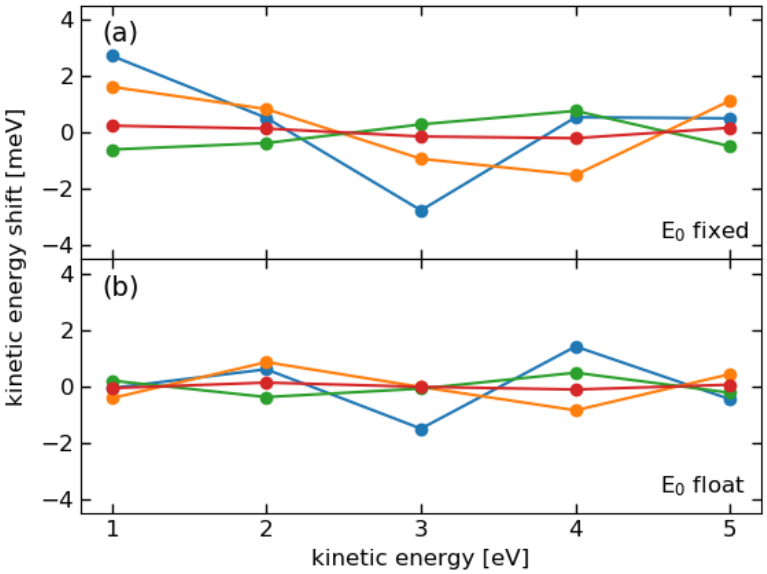

Figure 2.20: Residuals of the fit to equation 2.4 for each of the spectrometer designs. Colour scheme is the same as Fig. 2.19.

Table 2.1: Fitted values of the E_0 parameter from equations 2.3 and 2.4.

E_0 [meV]	3 plate	NRC	20 lens	PEPICO
R^2 fit	-89.2	-44.7	12.3	-22.5
R^4 fit	7.4	5.3	-2.1	0.8

2.10 Electron time spread

Table 2.2 lists the time spreads for each of the four designs. There was good agreement between the 2D and 3D simulations. The 3 plate design performs the worst in this category with a 1.8ns spread. With the estimated 100ps time resolution, this corresponds to 18 time slices of a 3D distribution. The 20 lens design is the best performer with a spread of 10.0ns, which corresponds to 100 time slices. Contrary to our predictions, it is not a large improvement over the NRC and PEPICO designs. The restrictions on the potentials required to maintain VMI conditions do not allow for significant reduction in interaction region field strengths to increase the time spread.

Table 2.2: Tabulated electron time spreads calculated from 2D and 3D simulations for each of the spectrometer designs. Units are in nanoseconds.

Simulation type	3 plate	NRC	20 lens	PEPICO
2D	1.8	8.6	10.0	8.0
3D	1.8	8.6	10.0	8.0

2.10.1 Time spread improvements

Using the explanation that the field strength in the interaction region determines the time spread, we sought to increase the time spread by reducing the field strength while still maintaining VMI conditions. We were able to achieve this by changing the linear stepped potentials of the thick lens extractor to a quadratic (nonlinear) stepped potential. To the best of my knowledge this has never been proposed before. To illustrate this difference, Fig. 2.21 shows the potential energy surface of (a) the quadratic stepped potential and (b) the linear stepped potential for the PEPICO design. The curved surface of (a) gives the electrons more time to spread out in the interaction region while the faster acceleration near the detector maintains VMI conditions. The potentials were optimized by hand by adjusting the repeller, light port and extractor voltages, and a curvature parameter to adjust the nonlinearity of the extractor electrode steps. The time spread achieved was 15.5ns, which is nearly double that of the linearly stepped PEPICO counterpart.

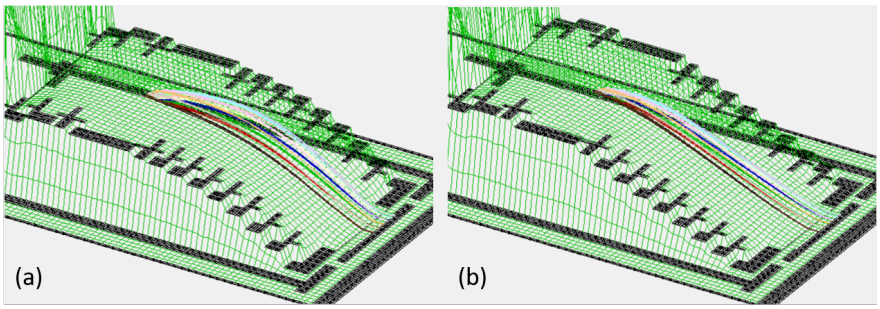

Figure 2.21: Potential energy surfaces of the PEPICO spectrometer using (a) quadratic stepped potential and (b) linear stepped potential for the thick lens extractor electrodes. The quadratic potential allows for a softer acceleration in the interaction region leading to a longer time spread while still maintaining VMI conditions.

The 2D simulation performance of the quadratic potential is shown in Figs. 2.22 and 2.23, with the previous results for comparison. The energy resolution is the same as the PEPICO design at 5eV with slightly less chromatic aberration at lower electron energies. The residuals show the shifts are the largest but comparable to the other designs. The resolution results along with the residuals indicate that this quadratic potential step will effectively maintain VMI conditions while increasing the time spread with little to no drawbacks. A major advantage of the quadratic potential step is that it requires no physical changes to the spectrometer, aside from having individual control of each electrode potential, and in principle can be applied to all three design options. The potentials used for this simulation are likely not maximally stretching the time spread and with full control over each electrode potential the parameter space to explore is enormous. With a powerful optimization routine, such as a genetic algorithm, a motivated student may be able to further increase spectrometer performance in one or more categories. For this reason, we have opted to install individual feedthroughs for each electrode to house the resistive voltage dividers outside the vacuum chamber.

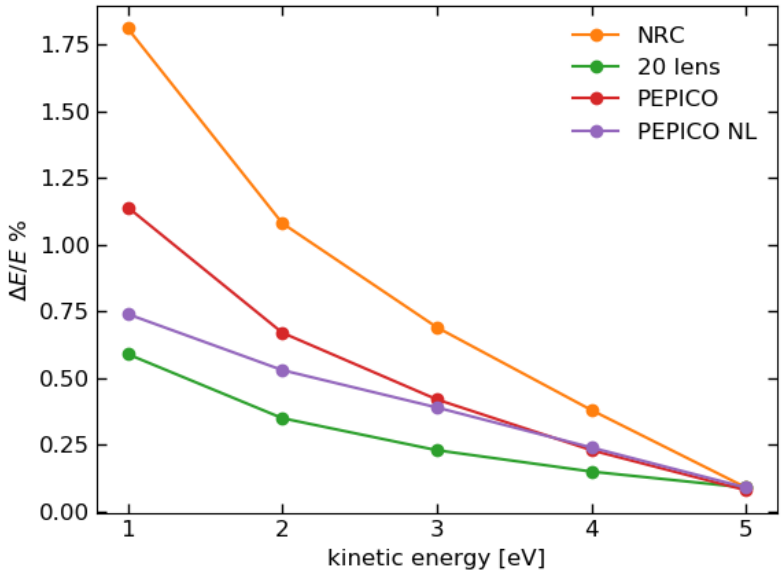

Figure 2.22: Same as Fig. 2.15, but with the quadratic stepped potential added for comparison, labelled PEPICO NL. The 3 plate design was removed to show the other designs more closely.

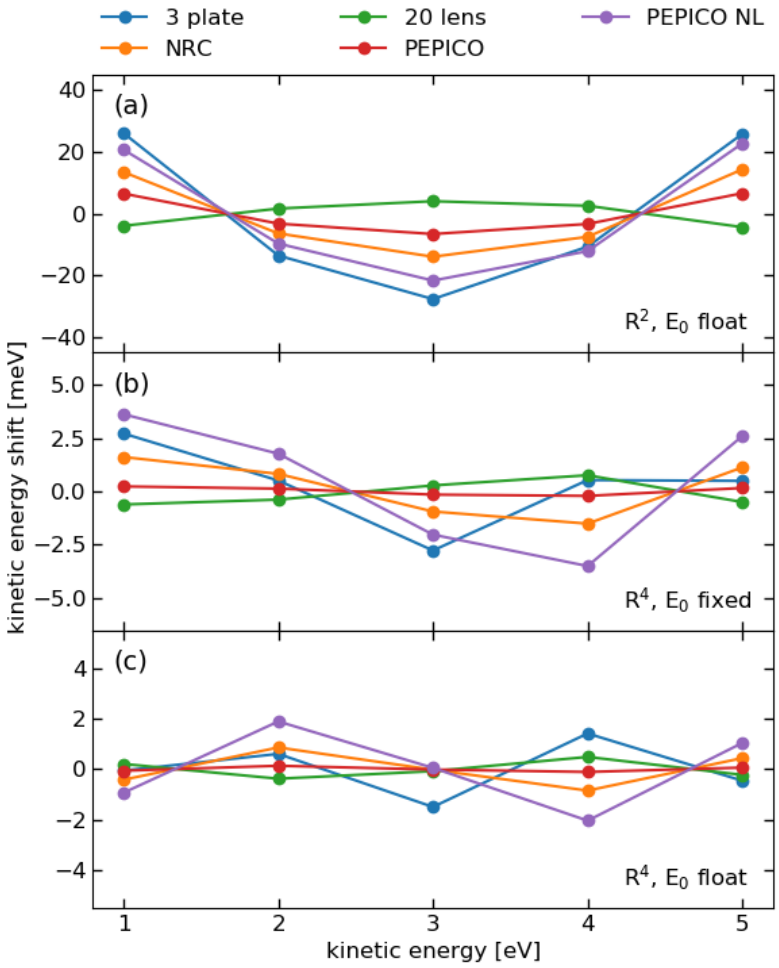

Figure 2.23: Residuals of fits to (a) equation 2.3, (b) equation 2.4 with fixed $E_0 = 0$ and (c) equation 2.4 with floating E_0. The quadratic stepped potential was added for comparison, labelled PEPICO NL.

2.11 TOF linearity

For ease of calibration, it is ideal to have a linear relationship between the TOF and initial velocity v_0 in the TOF direction. In a VMI spectrometer this is difficult to achieve as parameters such as flight length and curvature of field lines cannot be adjusted. Using again

the simple model of an electron in a uniform electric field, the equation of motion is

$$\Delta z = v_0 t + \frac{1}{2}\frac{eE}{m_e}t^2, \tag{2.5}$$

where Δz is the flight distance, e is the electron charge, m_e is the electron mass and E is the electric field. Solving for t, we obtain

$$t = \frac{-v_0 + (v_0^2 + 2a\Delta z)^{1/2}}{a}, \tag{2.6}$$

where $a = eE/m_e$. In the limit $v_0^2 << 2a\Delta z$, which implies the field strength is much greater than the electron initial kinetic energy, the TOF becomes linear in v_0. In the case of $v_0^2 >> 2a\Delta z$, we use the binomial approximation to reduce equation 2.6 to

$$t = \frac{\Delta z}{v_0},$$

where an inverse relationship between t and v_0 becomes apparent. In the case where v_0^2 is comparable to $2a\Delta z$, it is more instructive to solve equation 2.5 for v_0:

$$v_0 = \frac{\Delta z}{t} + \frac{1}{2}at.$$

From this equation we see that there is both an inverse and a linear component in time. Using a field of 500 Volts over 0.1m, which is approximately the total potential drop over the flight length of the NRC spectrometer for collection of 5eV electrons, the $\Delta z/t$ term is dominant over the range of 20-40ns. Thus, we expect to see an inverse relationship between v_0 and t using this model. While the constant field picture is a large oversimplification of the VMI spectrometers, it is a good starting point for energy calibration of the TOF axis.

The electron TOFs were investigated by recording the initial velocity v_0 and the TOF for

each electron using the same 3D Monte Carlo simulations as described earlier. Figure 2.24 shows a plot of the initial velocity v_0 as a function of the TOF for each design with linear fits in black. The only design that appears linear is the 3 plate design, which may also be due to its relatively short time spread compared to the other designs. The residuals are shown in Fig. 2.25, where a Δv_0 was calculated as the difference between v_0 and the fit, and then converted to an energy shift using $\Delta E = m_e v_0 \Delta v_0$. The 3 plate design is the most linear with a maximum energy shift of 183meV. The other designs are clearly nonlinear in TOF, with energy shifts above 1eV, which makes a linear calibration function unusable.

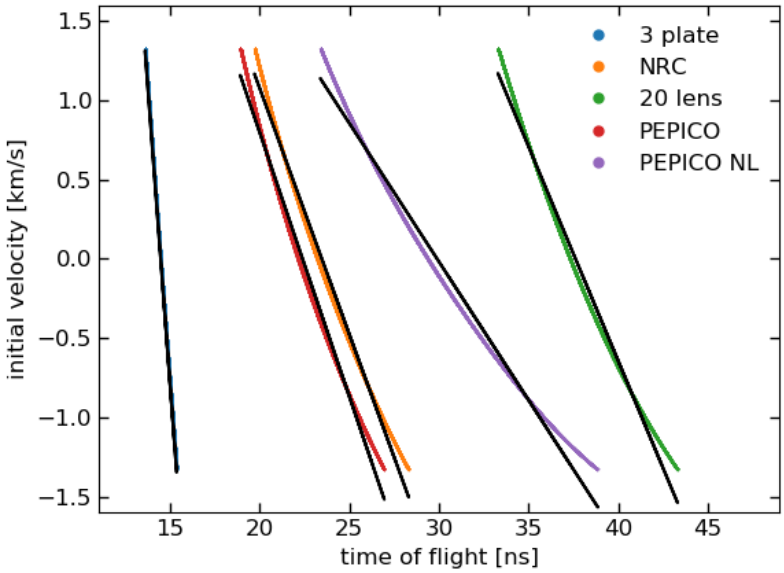

Figure 2.24: Electron initial velocities in the TOF direction as a function of TOF, with linear fits in black. Data are taken from 3D Monte-Carlo simulations.

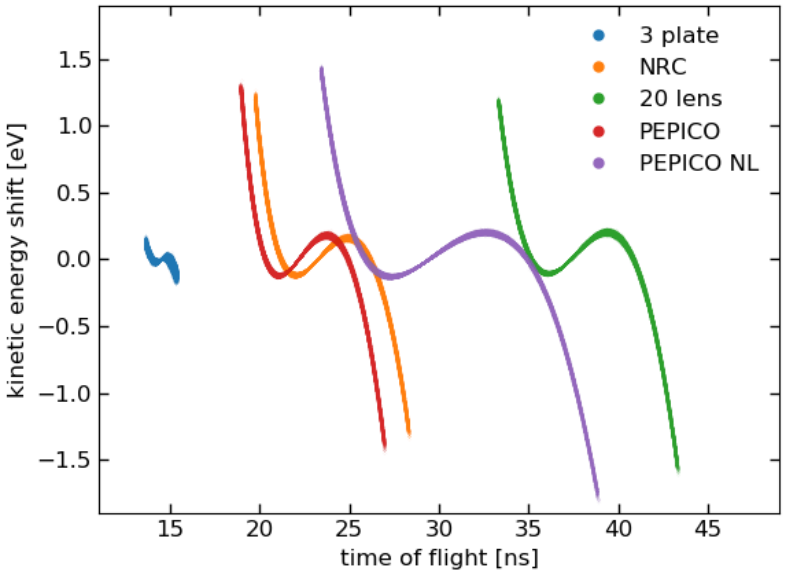

Figure 2.25: Residuals of the linear fits in Fig. 2.24 converted to energy shifts. The thickness of the line is due to the sampling of the interaction region volume.

Inverting the TOF axis and repeating the linear fit yields Fig. 2.26 with residuals shown in Fig. 2.27. Here the fits look more linear and the kinetic energy shifts are much smaller compared to the previous model. The NRC design behaves the most linear with a maximum shift of 146meV. The 20 lens design has the worst performance with a maximum shift of 600meV.

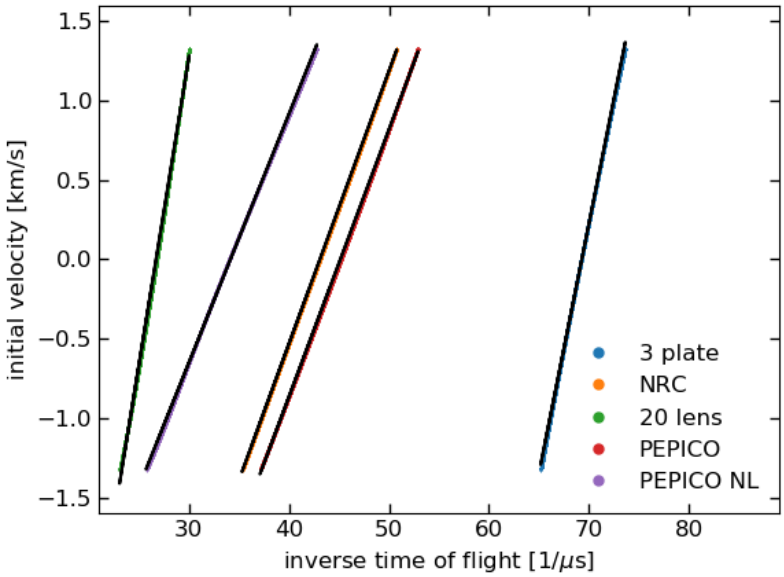

Figure 2.26: Electron initial velocities in the TOF direction as a function of 1/TOF, with linear fits in black. Data are taken from 3D Monte-Carlo simulations.

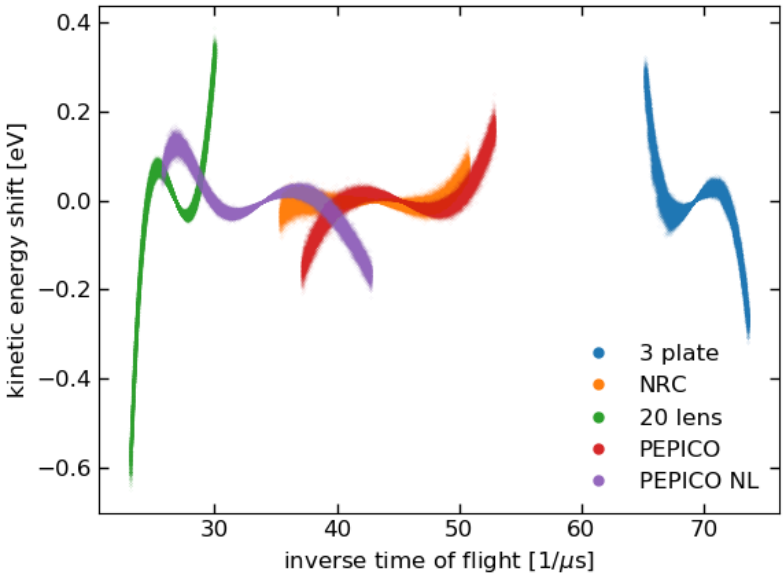

Figure 2.27: Residuals of the fits in Fig. 2.26 converted to energy shifts. The thickness of the line is due to the sampling of the interaction region volume.

It is clear from these simulations that the TOF is not a simple function of the initial

velocity. A more complicated, likely phenomenological relationship will be required to convert the electron TOF to initial velocity v_z.

2.12 Mass spectrometry resolution

Fast simulations were performed that sampled 8 points on the corners of a box of dimension 0.1×0.1×2mm with two initial velocities of 1710m/s and 1890m/s for each point. The initial velocities were arbitrarily chosen as a separation of twice the FWHM to represent the tails of the speed distribution. In these simulations mass M was defined as resolved if the last ion of mass m arrived earlier than the first ion of mass m+1. This is a very conservative estimate of the mass resolution as overlapping peaks can still be resolved even if their bases are partially overlapping (i.e. Rayleigh criterion). As the molecular beam geometry has a significant impact on the mass resolution, both geometries were simulated with the exception being the PEPICO design which does not allow for a molecular beam along the TOF axis.

Table 2.3 summarizes the mass resolutions up to 500amu. The parallel and perpendicular labels denote the molecular beam orientation relative to the TOF axis. From these results, it is clear that the perpendicular geometry significantly improves the mass resolution due to the negligible velocity spread along the TOF axis direction, the main limitation of the parallel geometry. The perpendicular configuration is limited by a combination of initial velocity, detector size and accelerating field strength. The initial velocity offsets the ion hit position on the detector and as the ion mass increases this effect becomes more pronounced. A larger detector or increasing the accelerating field strength would increase the mass resolution. In practice the detector size is fixed and increasing the electrode potentials above 5kV requires more serious consideration of electrical insulation to avoid arcing. Regardless, all perpendicular geometries had a mass resolution greater than 500amu, which satisfy our design goal of 300amu.

Table 2.3: Mass resolution for the NRC, 20 lens and PEPICO designs as determined by "fast" simulations. The NRC and 20 lens designs were tested with two molecular beam orientations: parallel (para) and perpendicular (perp) to the TOF axis.

	NRC para	NRC perp	20 lens para	20 lens perp	PEPICO
Mass resolution [amu]	205	>500	251	>500	>500

Monte-Carlo simulations were also performed around the fast simulation maximum resolution in order to visualize the peak overlap. These simulations sampled the 3D interaction region previously described, along with a normal distribution of initial velocities with a mean of 1800m/s and a FWHM of 90m/s. A sample of 10^4 ions were flown at each mass. These simulations give a better approximation to the overall mass resolution. As an example, the NRC parallel and perpendicular configurations at 300amu are shown in Fig. 2.28 (a) and (b), respectively. The black line in (a) represents the combination of the two peaks. If the peaks are of comparable height, a mass resolution of 300amu is possible in the parallel configuration, however the perpendicular configuration is clearly superior, as noted by the wide TOF separation between the peaks in (b). Simulations of the 20 lens design show the same behaviour.

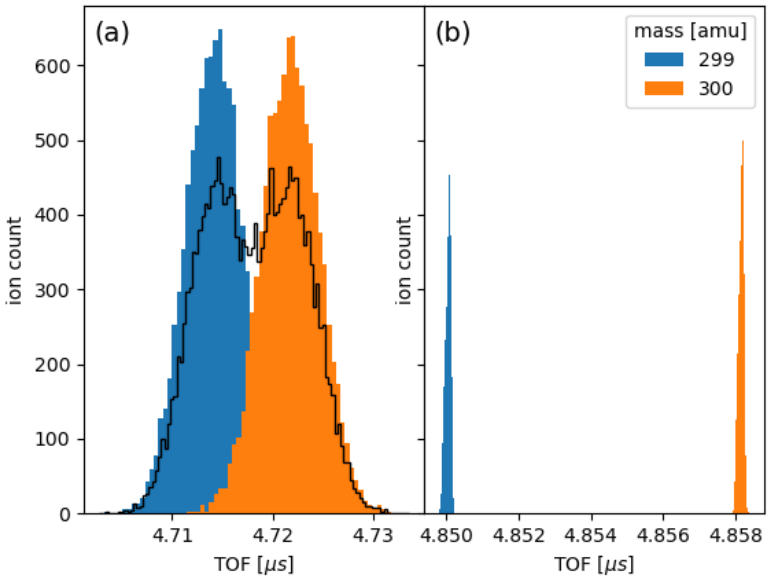

Figure 2.28: Monte-Carlo simulation of the mass spectrum at 300amu for the NRC design with molecular beam orientation (a) parallel and (b) perpendicular to the TOF axis. The black line in (a) represents both peaks binned together.

The conclusion drawn from the mass spectrometry resolution simulations is that the electrostatic lens design is much less of a factor than the choice of molecular beam geometry. A molecular beam perpendicular to the TOF axis will provide significantly higher mass resolution than its parallel counterpart.

2.13 PEPICO covariance performance

Previous simulations of photoelectron kinetic energy and mass spectrometry resolution of the PEPICO design were carried out with potentials chosen for the specific application. The true power of the PEPICO design lies in its ability to perform both functions simultaneously. Complexity comes hand in hand with measuring photoelectrons and photoions at the same time and, as such, the optimization in this mode of operation proved to be difficult. It was achieved by hand but by no means is it perfectly optimized. The trouble arises in that the ions require a minimum acceleration field which interferes with the optimization of the electron

VMI conditions. The maximum mass measurable is thus affected by the chosen maximum kinetic energy of electrons to be measured. If the spectrometer is optimized for low energy electrons at the maximum radius of the detector, the velocity of the molecular beam will have ions collide into the edges of the repeller plates before they can be accelerated through the repeller grid. At 5eV VMI conditions, the maximum measurable mass is 350amu. At 3eV conditions, the maximum measurable mass is 220amu. To avoid these issues, the difference in TOF timescales between electrons (ns) and ions (μs) could be leveraged by applying a voltage pulse to push the ions after the electrons have already reached the detector.

The VMI resolution is 0.5% at 5eV and follows the same trend as the other spectrometers. Figure 2.29 shows the relative resolution of the PEPICO design in covariance mode, labelled COV. Under these conditions, the covariance mode falls between the 3 plate and the other designs. A possible workaround to achieve maximum resolution is to perform the experiment once in covariance mode to associate the electrons with their parent ions and then to run the experiment again under high VMI resolution conditions, assuming that high resolution is not required to discern the electron-ion correlation.

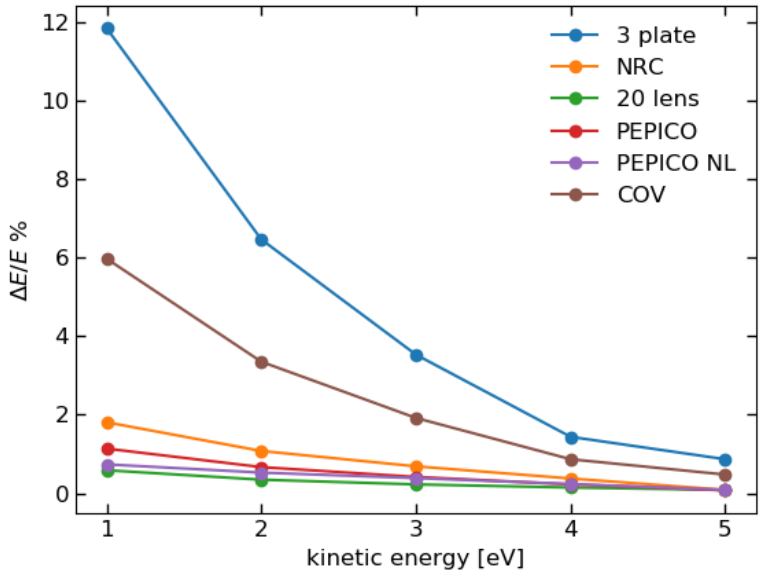

Figure 2.29: Relative energy resolutions with the PEPICO in covariance mode added, labelled COV.

2.14 The design choice

After careful consideration, we decided that the covariance capabilities of the PEPICO design outweighed the slightly better performance of the 20 lens design. The ability to measure photoelectrons and photoions simultaneously will likely provide more insight into the ultrafast molecular dynamics we are studying, as compared to a small improvement in time and energy resolution. The 3D VMI capabilities of all spectrometers considered are comparable and no major argument could be made for one over the other. The perpendicular molecular beam geometry is superior in terms of mass resolution, which means that the 20 lens design will have a more diffuse molecular beam due to the longer distance it must travel. For all of these reasons, we finalized our decision on the PEPICO design, and this instrument is currently under construction.

2.15 Conclusion

The technique of velocity map imaging is a powerful tool for photoelectron spectroscopy experiments because it measures both the photoelectron kinetic energy and angular distributions. Recent developments in the 3D VMI technique offer new experimental configurations such as crossed and magic angle polarizations, previously unavailable due to the cylindrical symmetry requirements of 2D VMI. With this advent, the considerations when designing a VMI spectrometer expand to include the time spread resolution alongside the photoelectron kinetic energy resolution and ion mass resolution. Different VMI spectrometer designs were compared with respect to these categories and a PEPICO design was chosen for its versatility and resolution capabilities. Modifications to the electrode potentials with the goal of increasing the time spread were also explored and a doubling of the time spread was achieved with almost no loss in photoelectron kinetic energy resolution. As of the writing of this thesis, the spectrometer design is finalized, and we are waiting for parts to arrive to begin assembly. We hope to collect our first images in the next year.

Chapter 3

Experimental Setup

3.1 Introduction

As stated in Chapter 1, time-resolved VMI photoelectron spectroscopy is a very powerful tool for the study of excited state molecular dynamics. When combined with the use of ultrafast VUV laser pulses, the experimental setup becomes very complex. When dealing with tunable VUV sources such as this one, it is a challenge to maintain the stability of ultrafast amplified laser systems to the required degree for the many hours needed for a typical experiment. This chapter will discuss the VUV generation setup, the VMI instrument, sources of instability, and calibration of the equipment. It is the technical foundation for the experiments described in chapter 4. I acknowledge Dr. Ruaridh Forbes and Dr. Rune Lausten for building the light source, Dr. Iain Wilkinson for designing and building the VMI instrument, and Dr. Andrey Boguslavskiy for writing the VMI data collection software. Their contributions have made this work possible.

3.2 Tuneable Vacuum Ultraviolet Source

A tunable vacuum ultraviolet (VUV) source leveraging non-collinear difference frequency four-wave mixing (DFFWM) in argon was built based on the work of Noack et al.[50]. Ultrafast VUV pulses near the fifth harmonic of Ti:Sapphire (152.5-154.5nm) were generated by mixing two photons of the third harmonic (pump, 267nm) with the output of an optical parametric

amplifier (OPA) tuned to the near infrared (seed, 980-1070nm) at a small angle in low pressure argon. By tuning the OPA output, the VUV wavelength can be tuned based on energy conservation. The non-collinear geometry is very favourable in that it allows for phase matching at higher pressures, providing an increase in flux by up to an order of magnitude over a collinear arrangement. Figure 3.1 (a) shows an energy diagram of the four-wave mixing process and Fig.3.1 (b) shows the wavevector phase matching conditions.

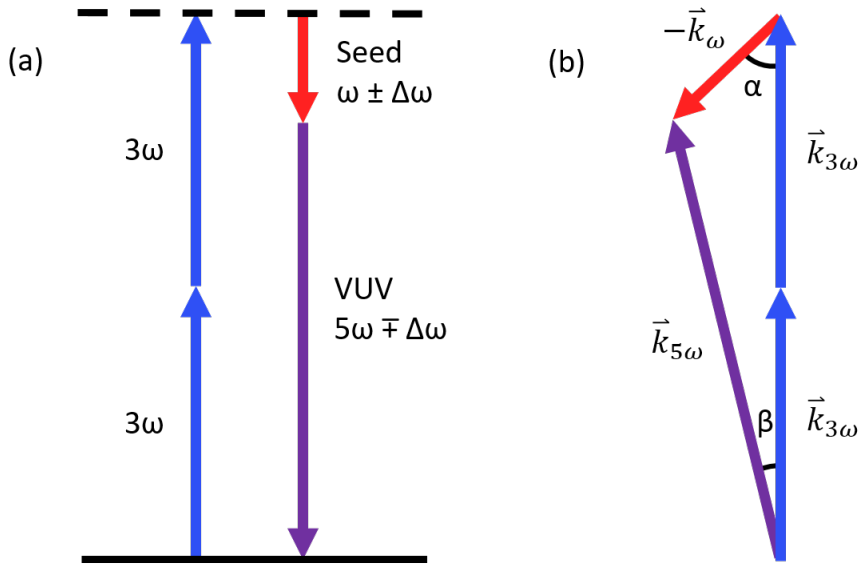

Figure 3.1: (a) Energy diagram of the difference frequency four-wave mixing process. Two photons of the third harmonic minus one photon of the tunable seed generates tunable VUV near the fifth harmonic. (b) Phase matching diagram of the relevant wavevectors.

In a collinear geometry ($\alpha = 0$), the optimal phase matching pressure is zero. As the angle α increases, so does the optimal phase matching pressure. This corresponds to more gas density in the interaction region, quadratically increasing the VUV flux. At larger angles, however, the interaction path length becomes the limiting factor and flux decreases[51]. At a fixed angle, the VUV flux increases as the pressure increases, up to the optimal phase matching pressure. Increasing the pressure beyond the optimal pressure decreases the flux, most likely due to pump depletion and multiphoton processes[50].

3.3 Our Source

Figure 3.2 shows a schematic of the femtosecond laser setup. The source started with 3.25mJ, 35fs pulses at 800nm from a 1 kHz Ti:Sapphire regenerative amplifier (Coherent Legend Elite Duo). A 70/30 beam splitter picked off 1mJ to pump an OPA (Light conversion TOPAS-C) that generated the tunable seed pulse for DFFWM (path 1). A second 70/30 beam splitter reflected 1.6mJ, used for third harmonic generation (path 2). The remaining 0.7mJ was used to generate a fourth harmonic (200nm) probe pulse used for time-resolved pump-probe experiments (path 3).

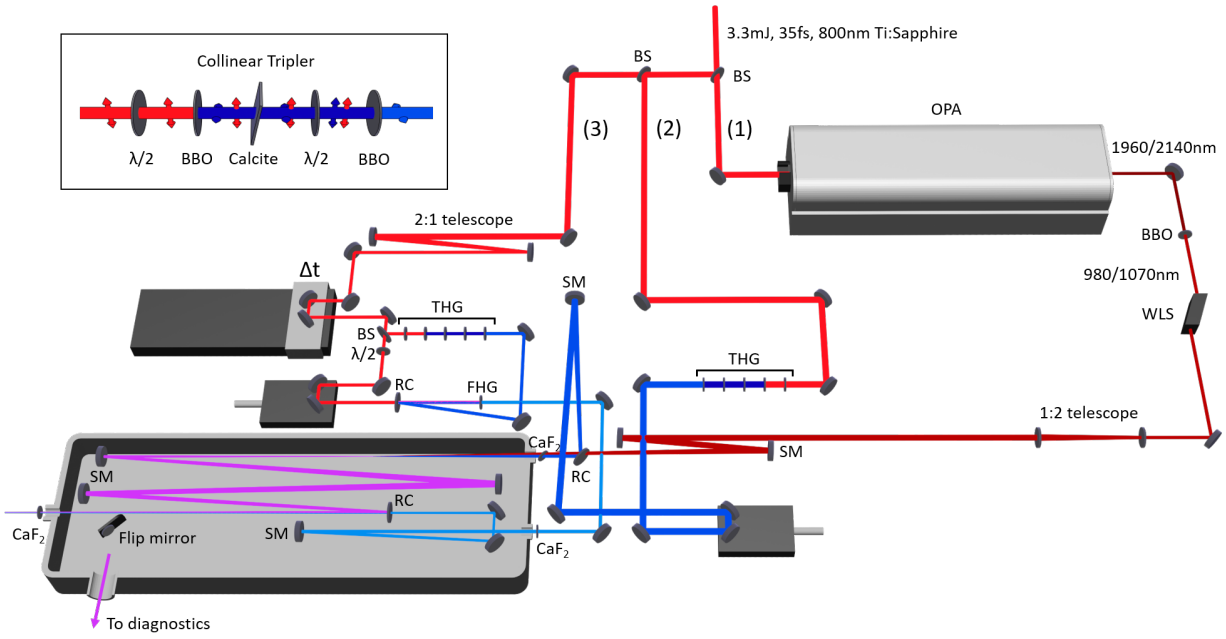

Figure 3.2: VUV pump-UV probe laser schematic. BS: beam splitter, OPA: optical parametric amplifier, BBO: beta-barium borate nonlinear crystal, THG: third harmonic generation, FHG: fourth harmonic generation, $\lambda/2$: half-wave plate, WLS: wavelength separator, SM: spherical mirror, RC: recombiner, CaF_2: calcium fluoride window. See text for details.

3.3.1 OPA seed

To generate the 152.5nm and 154.5nm VUV pulses, seed wavelengths of 980nm and 1070nm were required. To achieve this, the p-polarized idler output of the OPA was tuned to 1960nm (2140nm) and frequency doubled in 10×10×0.1mm beta-barium borate (BBO) cut at 21.0 degrees for type 1 phase matching. A wavelength separator (light conversion 955-1130nm) isolated the doubled idler from the signal and a periscope switched the output from s to p-polarization. A 1:2 telescope expanded the beam to mode match the third harmonic. A radius of curvature (ROC) = 2m spherical mirror focussed through a second dichroic beamsplitter used as a recombining optic (HR 267nm, HT 800nm). The beam passed through a 0.5mm CaF_2 window at Brewster's angle (55.6 degrees for 267nm) and into a vacuum chamber (VUV box) backfilled with argon. Typical pulse energies obtained were 14uJ at 1070nm and 18uJ at 980nm.

3.3.2 Third harmonic pump

A collinear tripler setup was used to generate the third harmonic. The p-polarized fundamental is doubled in a 10×10×0.2mm BBO cut at 29.2 degrees for type 1 phase matching. A 20×20×0.75mm calcite delay plate was used to compensate the group velocity mismatch between the residual fundamental (p-polarized) and second harmonic (s-polarized), thus temporally overlapping them in the third harmonic generation crystal. The polarization of the fundamental was then rotated by a 0^{th} order waveplate (phi = 15mm, λ @ 400nm, $\lambda/2$ @ 800nm) to permit Type 1 phase matching in the following nonlinear crystal. The fundamental and second harmonic were sum frequency mixed in 10×10×0.1mm BBO cut at 44.3 degrees for type-1 phase matching, generating the third harmonic. An additional half wave plate was placed before the first BBO crystal, making it possible to attenuate the third harmonic by rotating the incoming polarization, since the tripler only acts on one polarization component of the fundamental. This setup produced 0.18mJ, 35 fs pulses centered at 267nm. Several

dielectric mirrors were used to isolate the third harmonic and a manual delay stage was used to adjust time delay with respect to the seed. It is then focussed by an ROC = 1.5mm spherical dielectric mirror, reflected off the recombining optic described above, and through the same $CaF2_2$ window into the VUV box.

3.3.3 200nm probe

The 0.7mJ reserved for the probe was reduced by a 2:1 reflective telescope, passed through a computer-controlled optical delay line (Newport XML210) and was split 85/15 on a dielectric mirror. The 85% split, 0.6mJ, was sent to another tripler (with the last BBO crystal being 0.1mm thick rather than 0.05mm), while the remaining 15%, 0.1mJ, was rotated by a half-wave plate and passed through a manual delay line to permit type-1 sum frequency mixing with the third harmonic in a 7×7×0.1mm BBO crystal cut at 65 degrees. The fourth harmonic thus generated was isolated with a pair of dielectric mirrors and entered the VUV box through a separate 0.5mm CaF_2 window. This scheme generated 1.3uJ pulses at 200nm, measured before the window.

3.3.4 The box and VUV generation

The VUV box was a custom machined aluminum box with an O-ring sealed plexiglass lid made to fit a 24"×8" breadboard (Thorlabs MB824), which was bolted to the bottom of the box to mount the optics for the VUV pump/200nm probe pulses entering the VMI chamber. The box pumped down to roughly 10mTorr and was backfilled with argon for VUV generation. All parts mounted in the box were cleaned to ultra high vacuum standards, as minimizing outgassing is important for the longevity of expensive optical components and for long-term stability of the VUV flux.

Inside the VUV box, the 267nm pump and OPA seed beams were focussed to the same spot and were crossed at an angle of approximately 10mrad. A glass tube was placed around the foci as a sacrificial surface to adsorb any background molecules ionized by the plasma.

The box was backfilled with 40 Torr argon, which was the optimal phase matching pressure at this angle and provided more than enough flux for the present experiment. In order to achieve stable VUV flux over many hours, a continuous flow of argon through the VUV box was achieved using two needle valves on the gas input and pump out lines. This significantly reduced VUV absorption by background molecules arising from outgassing from components and residual leaks.

The generated VUV was separated from the drivers by two dielectric mirrors (HR 150-160 nm, p-pol, Layertec GmbH), refocussed by an ROC = 2.8m spherical dielectric mirror (HR 150-160nm, p-pol, Layertec GmbH), and reflected off a CaF_2 window substrate beam combiner coated HR 160nm. The fourth harmonic was focussed by an ROC = 4m VUVA coated spherical Al mirror and recombined collinearly with the VUV. Both beams entered the VMI chamber through a 0.5mm thick CaF_2 window.

A VUVA coated aluminum flip mirror was placed before the exit window to reroute the beams for diagnostics, all under vacuum. Figure 3.3 shows the setup of the diagnostic equipment. When the flip mirror is in place, the beam is routed to a motorized VUVA coated Al mirror (called the pinhole mirror), through a 200um pinhole and into a VUV monochromator (McPherson model 502). The pinhole was positioned at roughly the same distance as the molecular beam (MB) inside the VMI chamber so that forcing both beams through the pinhole will guarantee their spatial overlap at the MB. A VUV photodiode (OSI Optoelectronics XUV 100) was attached to one output of the monochromator. The photodiode was connected to an oscilloscope (tektronix 7104) via a photodiode amplifier (Thorlabs PDA200C). A VUV spectrometer (Resonance VS7550) was attached to the other output of the monochromator with a manual flip mirror to switch between the two. The spectrometer was controlled with the provided laptop and software from Resonance[52]. All the slits on the monochromator were opened completely. The photodiode was used with first order reflections from the monochromator grating for rough (not calibrated) separation of

colours (i.e. to isolate VUV, 200nm or 267nm). This allows for individual alignment of beams through the pinhole, flux optimization and day to day flux comparisons. The spectrometer was used to estimate VUV wavelength/bandwidth and to monitor wavelength drift over time if the 267nm/OPA time delay drifted. A more detailed description of spectrometer operation/limitations is given in the next section.

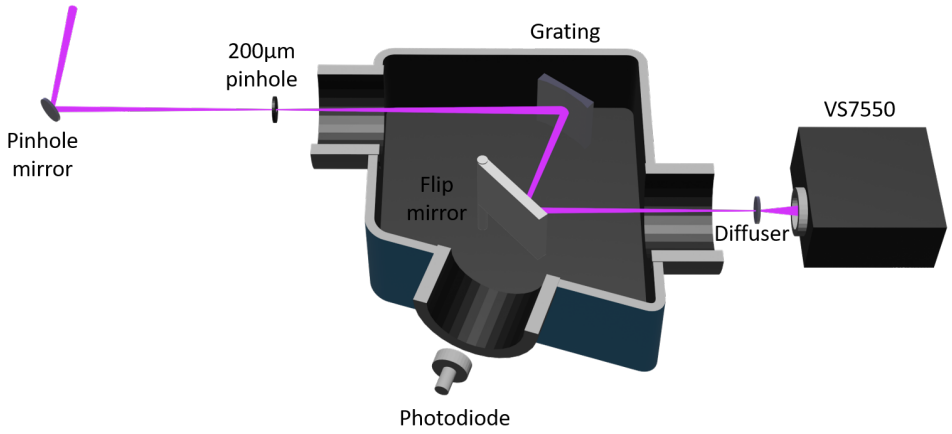

Figure 3.3: Schematic of the laser diagnostics. When the flip mirror in the VUV box is in place (not shown) the beams reflect off the motorized pinhole mirror through a 200um pinhole and into the McPherson 502 monochromator. Inside the monochromator, the beams reflect off a grating and either go straight to a photodiode (1st order reflection) or reflect off a flip mirror to the Resonance VS7550 VUV spectrometer through a diffuser (0th order reflection).

3.3.5 VS7550 VUV spectrometer

The Resonance VS7550 VUV mini spectrometer with installed 3600 lines/mm grating was used for measurement of the VUV wavelength/bandwidth and to monitor the wavelength drift over the course of an experiment. Unlike the photodiode, the spectrometer is not under vacuum. It is attached to the monochromator via an MgF_2 window. A continuous flow of nitrogen is used to purge the spectrometer for VUV operation. To use the spectrometer,

the monochromator grating is set to 0th order reflection and the flip mirror is moved into position. The slit width was set to $200\mu m$ and the grating position to -10 using the VS7550 software. A $200\mu s$ integration time was usually sufficient to collect a VUV peak height of >1000 counts with this slit width. The monochromator grating angle was then adjusted to maximize signal on the spectrometer.

While the stated wavelength accuracy with this grating is $\pm$0.12nm (using the $25\mu m$ slit), in practice we found the spectrometer to be unreliable. The servo motors that control the slit width, aperture size and grating position do not always return to the correct positions. In addition, the input beam to the spectrometer must follow the same beam path from day to day for reproducible results. In our case, the daily adjustment of the beam pointing through the pinhole changes the incident angle into the spectrometer. To mitigate these effects, an MgF_2 diffuser window with a roughened surface was placed in front of the spectrometer input to diffuse the beam for uniform illumination of the slits. This improved performance, but there were still discrepancies between the wavelength measured by the spectrometer and by xenon. For this reason, we deferred to the xenon photoelectron spectrum for absolute VUV wavelength calibration.

3.3.6 Setting up VUV

To first find VUV, a collinear geometry was used as it is much easier to find spatiotemporal overlap. With an open box, the 267nm pump was attenuated to low power for alignment. The pump and OPA seed were roughly collinearly aligned using a business card in the focal plane and an iris in the far field. For more accurate alignment at the focus, two successful methods will be discussed. The first method was to align both beams through a pinhole. The second was to place a glass slide at the focus of the pump, increasing the power past the damage threshold (watching for specular reflections from the slide), then blocking the pump and aligning the seed for maximum specular reflection on the damage spot. I prefer the

second method as it does not require adjusting the height of the pinhole to perfectly match the beam heights; the pump will burn its own pinhole position. Both methods requires several iterations aligning at the focus and in the far field to achieve collinearity.

The next step is to find time overlap of the pump and seed. Below we will discuss two methods we normally apply to do so. The first method is to sum frequency mix the pump and probe by placing a BBO crystal (theta = 50 degrees, type 1 phase matching) in the focus, followed by a CaF_2 prism to separate the colours and project them onto the box wall. When the pulses are overlapped in space and time the 267nm and 1070nm sum frequency mix to 214nm and a new spot appears. This method worked very well provided one is careful choosing the correct phase matching angle as it varies considerably over the OPA tuning ranges. This can be mitigated by using a thin crystal which allows for more broadband phase matching.

The second method that can be used to find time overlap leverages plasma defocussing of the seed by the intense pump pulse in air. The same prism setup is used to separate the colours and an infrared (IR) viewer is used to monitor the seed spot on the wall. It is important to cover the box (without pumping down) as air currents on the table will make the defocussing effect much harder to see. Time delay is varied manually until a small flaring of the seed is seen. I will note that this method was much more difficult to use, and I spent several days looking to no avail. It is hard to see minute changes in a small spot through an IR viewer, especially when staring at it for long periods of time. I only saw the defocussing effect after I knew they were overlapped in time using the first method.

After finding overlap, the crystal and prism were removed. The 200nm and 267nm were routed through the VMI chamber by roughly aligning them on the center of the entrance and exit windows, ensuring there is minimal clipping. The flip mirror before the VMI was flipped into place and both beams were routed through the pinhole at the entrance to the monochromator using the motorized pinhole mirror. The box was then closed and pumped

down overnight.

The OPA was turned on for at least an hour before operation to minimize path length drift as the breadboard thermalizes (the reflections dumped inside the OPA are significant enough to cause the baseplate to thermally expand). Because the k vectors of the two photons of 267nm and the VUV are pointing in almost the same direction, the 267nm is used as a tracer for the VUV. The monochromator grating was set to 0th order reflection onto the photodiode and the 267nm tracer was maximized through the pinhole. The monochromator grating was set to 152.5-154.5nm. The VUV box was backfilled with an excess of argon (70Torr) and evacuated at least three times to purge residual gas that absorbs VUV. After purging, the box was filled to 10Torr argon since the VUV phasematches at low pressures for a collinear setup. Timing between the 267nm and OPA pulses was adjusted until VUV signal appeared on the oscilloscope. If signal did not appear the timing was set to the previous position with known overlap, the monochromator was set to 0^{th} order, the 267nm was realigned through the pinhole and the VUV was looked for again. We would typically find signal on the first try with this method.

The angle between the pump and the seed was opened by walking the seed while maintaining signal on the photodiode. The argon pressure and timing were adjusted for maximum VUV signal after small increments to the angle. Iteration was stopped after maximum signal was achieved at 40Torr, which corresponds to an angle of 10mrad. This provided more than enough flux for the experiment, while also avoiding effects arising from higher argon pressures.

3.3.7 VUV wavelength tuning

Large steps in VUV wavelength were made by tuning the OPA. Figure 3.4 shows the VUV tuning curve for a 267nm pump. The VUV wavelength is calculated with basic energy

conservation using the formula

$$\lambda_{VUV} = \frac{1}{\left(\frac{2}{267nm} - \frac{1}{\lambda_{OPA}}\right)}.$$

For more information on OPA tuning see Appendix C.

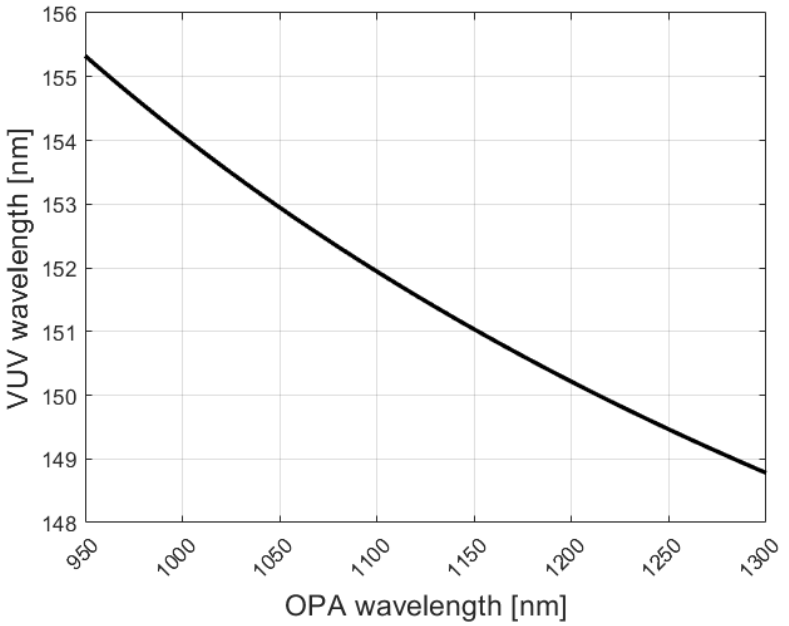

Figure 3.4: VUV wavelength dependence on OPA wavelength, based on energy conservation. The pump wavelength was fixed at 267nm.

For fine tuning, it turns out that small adjustments to the 267nm pump time delay with respect to the OPA seed also changes the VUV wavelength by a small amount. We attribute this to a longer, chirped OPA pulse being gated by a shorter 267nm pulse. At different time delays the 267nm is mixing with different frequency components of the OPA pulse. We can tune approximately ±1nm from the theoretical VUV wavelength without significant drop in flux using only timing.

3.4 VMI setup

The experiment in chapter 4 was performed in a thick lens VMI spectrometer designed and built by Dr. Iain Wilkinson in 2014. It was the precursor to the new VMI instrument and the function of the electrode stack was described in chapter 2. In short, the VMI consists of two main chambers: the source chamber and the experimental chamber. The source chamber houses a pulsed valve that fires gas pulses through a molecular beam skimmer into the experimental chamber. The laser enters the experimental chamber through a calcium fluoride window followed by a set of laser baffles to minimize scatter. The gas pulse intersects the laser in the center of a set of concentric electrodes that make up the VMI stack. The electrodes push the emitted photoelectrons to an MCP detector with attached phosphor screen. A CCD camera outside the chamber collects images from the phosphor screen through a viewing window.

3.4.1 Pulsed valve operation

The molecular beam was generated with an Even-Lavie pulsed valve. The Even-Lavie pulsed valve is a specialty valve capable of generating short ($20\mu s$), supercooled (by supersonic expansion through a nozzle) gas pulses at a 1kHz repetition rate[53]. Typically, the mixture used is a small concentration of target molecules (around 1%) seeded in high pressure (>25 PSI) helium. There are several parameters that affect the pulsed valve operation: valve temperature, valve opening time, and backing pressure on the valve. This section will describe how the valve was operated and the different parameters that affect the generation of stable, short, cold gas pulses.

The pulsed valve heater was set to 40 °C for all gases. Warming up the pulsed valve increases the temperature of the gas before the hard expansion to reduce cluster formation. If clusters are present, increasing the valve temperature can disfavour the formation of these

weakly (typically van der Waals) bound species. Decreasing the concentration of target molecules will quadratically reduce cluster formation but also linearly reduce the monomer signal.

The valve opening time was set between 16.8-18μs, depending on the gas. The opening time was set as short as possible to reduce background gas in the experimental chamber. There is a lower limit of 15μs for stable valve operation; below 15μs the valve begins to stick. A longer opening time was used to increase gas density for weaker photoelectron signals.

The backing pressure on the valve affects how hard the gas expands out of the nozzle, which determines the rotational temperature of the target molecules[53]. A higher backing pressure is typically preferred as having the molecules in their ground state reduces the number of different possible excited state transitions. The downside to higher backing pressures is an increase in background gas, increased risk of cluster formation and an increase in gas consumption. The valve is rated for 0-1450 PSI, but pressures of 25-70 PSI were typically used.

3.4.2 VMI alignment procedure

Once the pump and probe beams were aligned on the pinhole, optimal overlap in the center of the molecular beam (jet) was found: the basic idea is to choose a target molecule that only has a one-colour signal (pump or probe), then to walk the beam to find maximum photoelectron yield on the camera while simultaneously minimizing the scatter and maintaining overlap on the pinhole. After overlapping with the jet, rough time zero must be found using a molecule that has a two-colour signal (pump + probe). The steps to turn on the VMI spectrometer and align the beams on the jet were performed as follows:

1. The gate valve was opened, paying close attention to the ion gauges in both the source and experimental chambers. The base pressure was typically 10^{-7} Torr in the source chamber and 10^{-9} Torr in the experimental chamber. When the gate valve was repo-

sitioned, it was normal for the pressure inside both chambers to increase by around two orders of magnitude. It is important that the gate valve arm be pushed in as far as possible so that the skimmer is properly aligned with the pulsed valve. When the gate valve is seated in place the pressures should quickly return to base level. If it is over/under tightened the O-ring will not make good contact and the chamber pressures will not drop back to baseline.

2. The VMI Live TV interface (real-time image display of the MCP camera) was opened with a three frame running average by typing vmilivetv2(3) from the MATLAB command line, where the argument is the number of running average frames. This was to ensure the MCP was not damaged while other systems were turned on.

3. The ion gauge in the experimental chamber was turned off. If it is left on while the pulsed valve is running, the background gas will be ionized by the gauge and contribute a large background signal. This can be useful for measuring detector gain spatial inhomogeneity but for experiments it must be turned off.

4. The power supplies for the MCP were turned on. The voltage on the back MCP was gradually ramped up to +1600V and the phosphor screen to +4000V. Voltage settings for the electrode stack are given in Table 3.1. The most common setting used was for 10eV electrons.

5. For the wavelengths of 200nm and 152.5-154.5nm, four gases are very useful for alignment and finding time zero overlap:

   (a) Butadiene has a large absorption cross section at 200nm. It shows a strong two-photon 200nm signal and is useful for finding the gas jet.

   (b) OCS has a large absorption cross section in the 157-146nm (VUV) range. It shows both a strong two-photon VUV signal and a strong 200nm + VUV signal.

It is useful for initially finding the jet with VUV only, as well as roughly finding time-zero by eye.

(c) Xenon has a weaker non-resonant 2×200nm signal that is useful for finding the exact center of the jet. It also has non-resonant 200nm + VUV signal that is used for VMI energy calibration, VUV wavelength calibration, and pump-probe cross-correlation. These aspects will be discussed in detail in section xenon.

(d) SO2 has a nice 200nm + VUV step function signal useful for finding time-zero overlap. When the 200nm precedes the VUV there is a strong signal. At time-zero the signal is halved. When the VUV precedes the 200nm the signal disappears. A detailed list of the gas properties and the relevant settings is shown in Table 3.2.

6. Butadiene was used first to find the jet with 200nm. The pulsed valve was turned on using the parameters listed in Table 3.2. Assuming both beams were already on the pinhole and roughly aligned through the VMI, the 200nm was unblocked while monitoring the LiveTV video ensuring that the scatter was not too intense. The back MCP voltage was then ramped up to +1700V.

7. The 200nm was fanned left/right by hand with the last mirror before the VUV box to find the jet, taking note of the direction that the beam moved. The 200nm was moved back onto the pinhole. In incremental steps without losing signal on the photodiode, the 200nm was moved in the direction of the jet, then the pinhole was "moved" onto the 200nm (by moving the pinhole mirror), then the VUV was moved onto the pinhole. One beam was moved at a time and only on one axis to avoid completely losing transmission through the pinhole. If alignment through the pinhole was lost, the VUV box was vented and the 200nm and 267nm pump were aligned through the pinhole using a business card.

8. Once the 200nm, the VUV and the pinhole were roughly on the jet, the gas was switched

to xenon. The weaker two-photon 200nm signal from xenon had better contrast between the center of the jet and the background gas in the chamber. The MCP voltage was ramped up to 1800-1900V and step 7 was repeated until the pinhole was positioned on the center of the jet. Once the pinhole is centered the pinhole mirror was not moved anymore. Note that when switching gases, the MCP voltage should be lowered to roughly 1600V before the pulsed valve is switched back on. There is a high-pressure transient "puff" of gas from the pulsed valve when it is turned on that can cause arcing on the MCP if the voltage is too high. This lasts about one second.

9. The goal now is to try to center the beam on the entrance and exit baffles. The 200nm was fanned left/right to find where it starts scattering on the baffles, taking note of how far from the jet scattering occurs in each direction. Using the last two mirrors outside the box, the beam was walked in both directions until the scattering edges were equidistant from the jet. Walking was done with the beam on the pinhole, steering both mirrors at the same time in small increments while maintaining maximum signal on the photodiode. The flip mirror was lowered periodically, and the beam was fanned to check the scattering limits. Note that the NRC VMI has baffles that are not perfectly straight and a jet that is not perfectly centered. Perfect alignment was not possible. The best course of action was to walk the beam around to get the most signal from the jet while minimizing the scatter. This was done by eye, but an integrated photoelectron yield could easily be calculated on the fly and would be a more quantitative solution.

10. Once the horizontal plane was optimized, the vertical plane was optimized in the same manner. Since the jet axis is vertical in the NRC VMI, it was more difficult to find the center in this plane. Consequently, it is also less critical in terms of signal strength as the gas density does not vary as much along the vertical direction of the gas "slug".

11. The VUV was optimized in the same manner as the 200nm. The gas was switched

to OCS and the MCP voltage is changed to 1600V. Steps 9 and 10 were repeated, except the VUV was beam-walked using the motorized recombination mirror and the aptly labelled "not-recombination" mirror until scatter was minimized. The VMI is now ready for experiments.

Table 3.1: VMI electrode voltage settings for different photoelectron maximum kinetic energies. The last row are the voltage settings for ion mass spectrometry.

KE_{max} [eV]	V_{RG} [V]	V_R [V]	V_E [V]	V_{DG} [V]
10	-1030	-1040	-905	0
5	-510	-520	-452	0
1	-488	-508	-486	-389
Mass Spec.	+1710	+1720	+1395	0

Table 3.2: List of useful gases and their properties for VUV pump and 200nm probe pulses.

Gas	Mixture	Backing pressure	Valve opening time [μs]	MCP gain [V]	Signal
Butadiene	1%	1.45 kTorr	16.8	1600-1700	2×200nm
OCS	1%	1.45 kTorr	16.8	1600-1700	200nm+VUV 2×VUV
Xenon	5%	3.7 kTorr	18.0	1800-1900	2×200nm
SO_2	1%	3.7 kTorr	16.8	1700	200nm+VUV

3.4.3 Stability

Laser stability over the course of an experiment that lasts several hours is always a concern. In Femtolab 4 at the National Research Council Canada it has been a challenge to keep the laser system stable over the course of the OCS experiments. These types of experiments, involving many stages of nonlinear conversion to generate the ultrafast pulses, are difficult and require the very best in lab stability with respect to vibration, temperature, and humidity. Despite these requirements, we were able to successfully run experiments without active stabilization measures. This section will highlight some of the laser stability issues encountered while attempting the OCS experiment. These instabilities arise in several forms, including:

- Laser amplifier intensity fluctuations
- VUV wavelength drift
- VUV intensity decay
- Pump-probe spatial overlap drift
- Pump-probe cross-correlation drift
- Pump-probe time-zero overlap drift

The following sections will briefly describe each point on the list above.

Laser amplifier intensity fluctuations

Laser amplifier intensity fluctuations can cause much more severe fluctuations in later nonlinear conversion stages. The VUV intensity is dependent on a four-wave mixing (FWM) process involving two photons of the third harmonic and one photon from a frequency doubled OPA idler output. The third harmonic intensity scales as the cube of the fundamental and since two photons are required in the FWM process, the VUV intensity is dependent on the fundamental to the sixth power, i.e., $I(5w) \propto (I(\omega)^3)^2 = I(\omega)^6$ in the 267nm pump arm of the VUV generation scheme.

The OPA output intensity dependence is a little more complicated. The OPA (Light Conversion TOPAS-C) is a two-stage amplifier seeded by white light generation. While white light generation is a third order process, there is some intensity clamping and the white light intensity is not strictly third order in pump intensity. I will estimate it to be linear. The two amplification stages are second order difference frequency mixing processes, but only require one extra pump photon per stage as the other photon comes from the white light seed or the previous amplification stage. Adding these up, the OPA output is third order in input intensity. Combined with the frequency doubling of the output just after the

OPA, the intensity dependence is estimated to be $I(\omega_{2idler}) \propto I(\omega)^6$. The VUV FWM process is linear in OPA seed intensity, so in total, the VUV intensity dependence is estimated to be $I(\omega_{VUV}) \propto I(\omega)^{12}$. To give a sense of the effect, a 1% fluctuation in laser amplifier intensity will result in roughly an 11% fluctuation in VUV intensity.

Large VUV fluctuations were sometimes observed. If the VUV flux was very unstable (±20%, as measured by the photodiode), it was often caused by a poor laser compressor setting, which affected the OPA output which in turn affected the VUV flux. This was diagnosed by looking at the power fluctuation of the OPA output, or by checking the white light generation stage inside the OPA. For further details see Appendix C.

VUV wavelength drift

As mentioned in section 3.3.7, the VUV wavelength can be tuned by changing the time delay between the 267nm pump and the OPA seed. While this was very convenient for fine tuning, it was also subject to drift during experiments. The OPA in particular is highly subject to timing drifts as it has a long internal path length (1.5m) with many components affixed to a small breadboard. With 1W of input power, the internal breadboard must thermalize before stable output can be expected. We diagnose VUV wavelength drift with either xenon wavelength measurements before/after the experiment, or by comparing with a reference spectrum using the VS7550 VUV spectrometer.

VUV intensity decay

VUV intensity decay is due to outgassing or leaks in the VUV box. Oxygen is highly absorbing in the VUV[54] and we see a rapid decay in signal if the box is filled with argon once and left alone. Therefore, to achieve stable VUV flux over many hours, a continuous flow of argon through the VUV box was achieved using two needle valves on the gas input and pump out lines. This significantly reduced VUV absorption by background molecules arising from residual leaks. For similar reasons, the box is filled to roughly 70 Torr of argon and

subsequently evacuated three times before setting the final pressure, a process we call purging. If the timing is correct between the 267nm pump and OPA seed this step increases the VUV flux observed by orders of magnitude. Note that there is always a leak rate of air into the box, as well as outgassing from various sources inside the box. After the box has been purged and set to the correct pressure, there will be a transient change in the argon/air ratio until the leak rate reaches equilibrium with the needle valve flow. Therefore, for stable VUV output, it is important to allow the system to equilibrate. As the system settles down, the overall VUV flux decreases, which can be detrimental for overall photoelectron signal but removes the necessity to correct for the decay in the data analysis, and will only increase flux until the system equilibrates. VUV intensity decay due to leaks is diagnosed by measuring VUV flux while purging and refilling the box with argon.

Pump-probe spatial overlap drift

Pump-probe spatial overlap can change when the pointing of the laser drifts over time. This is a thermal effect that is inherently coupled with the time-zero overlap. It only happens on longer time scales though as air currents only modify the refractive index and not the propagation direction. We diagnose pointing changes by optimizing spatial overlap on the pinhole.

Both the VUV decay and the spatial overlap drift will manifest as a decrease in photoelectron yield as a function of time. Figure 3.5 shows two examples of photoelectron yield versus collected data point for (a) no photoelectron yield decay and (b) apparent photoelectron yield decay. This is a clear warning sign to reoptimize the setup and restart data collection.

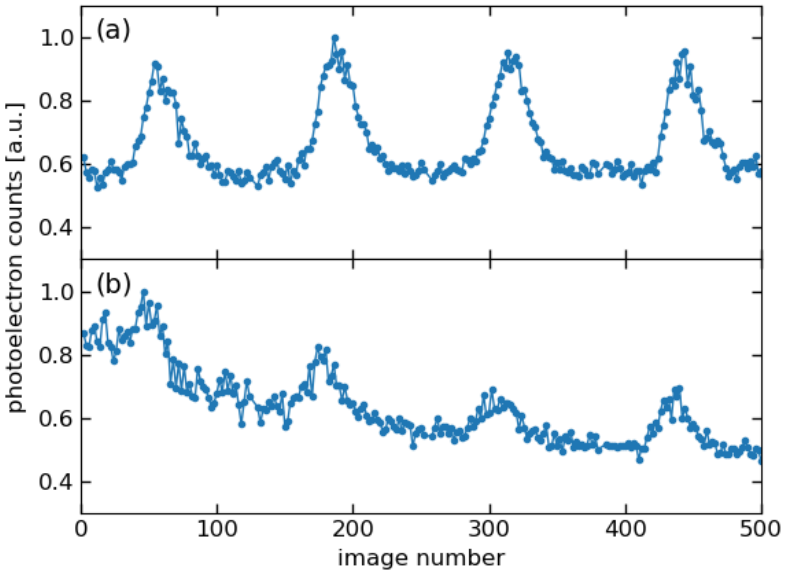

Figure 3.5: Total photoelectron yield as a function of image number (time) for (a) no photoelectron yield decay, and (b) photoelectron yield decay.

Pump-probe cross-correlation drift

Pump-probe cross-correlation drift occurs when the durations of the VUV pump and/or 200nm probe pulses change. This is a direct cause of a change in the compression of the 800nm pulse. I have found that throughout the day the compressor needs to be adjusted slightly, and around 6pm the pulse compression will almost certainly drift. This not only affects the durations of the pump and probe pulses; it can also have a severe impact on the function of the OPA (discussed more in Appendix C). The most likely cause of compression change is changes in pointing of the regenerative amplifier into the compressor. We diagnose this drift with xenon cross-correlation measurements before and after the experiment.

Pump-probe time-zero overlap drift

Pump-probe time-zero overlap is determined by the total path length between the pump and probe. As both paths are several meters long, this opens the door to path length instabilities. Small changes to path length, caused by air currents on short time scales, as well as thermal

expansion/contraction on long time scales, spoils the overlap. Air currents are mitigated by encasing the entire optical setup with plexiglass boxes. In the experimental data, time-zero drift will manifest as a timing jitter where each data point will have a time-zero uncertainty. If the uncertainty is comparable to the timescales of the molecular dynamics, the measured time constants become irrelevant. We diagnose time-zero overlap drift with xenon cross-correlation measurements before and after each experiment.

3.4.4 Strategies for reducing instabilities

There are several steps that can be taken to defend against these instabilities when one is interested in collecting a "good" dataset:

1. Experiments are most stable when run at night, and during the summer or winter seasons when temperature and humidity fluctuate the least.

2. Turn the laser on early in the morning. Ensure that the build-up trace is at the correct level. If it is not, small cavity adjustments may be necessary. Allow it to warm up for at least one hour. Check the build-up trace again before proceeding.

3. Ensure that the compression is set correctly. Turn on the OPA. Allow the OPA to warm up for at least one hour.

4. Optimize the 200nm and the VUV through the pinhole.

5. Make small adjustments throughout the day to keep pointing aligned and OPA/266nm timing overlapped. If the VUV flux is unstable, the most likely cause is improper pulse compression.

6. The NRC HVAC system changes to night mode around 6pm. This has a significant impact on stability. Repeat optimization of compression, pointing and timing overlap. Ensure that the continuous argon flow has equilibrated (roughly one hour).

7. Aim to start the xenon wavelength calibration around 7pm. Fine tune the wavelength with the 267nm/OPA timing and repeat xenon wavelength calibration until the wavelength is correct. Save a VUV spectrum with the VS7550 spectrometer.

8. Perform a time-resolved xenon scan and process the data right away. Write down the cross-correlation and the time-zero offset. Double check the wavelength with this dataset. Save a VUV spectrum with the VS7550 spectrometer.

9. Perform actual experiment. Keep an eye on the total photoelectron yield as a function of scan number. It should look like Fig. 3.5 (a). Pause from time to time to verify the VUV spectrum has not changed on the VS7550. Do not adjust pointing, 266nm/OPA timing, or refill the VUV box with argon. These can all influence the cross-correlation and the time-zero offset.

10. Perform another time-resolved xenon scan for the post experiment cross-correlation and time-zero offset. Check the VUV wavelength again. *Pray that nothing has changed.*

3.5 VMI data acquisition

The structure of the VMI data acquisition is as follows: a list of time delays is made. At each time delay two images are collected. The first is an image with the molecular beam overlapped in time with the laser pulse, which is the signal of interest. The second image is taken with the molecular beam delays $200\mu s$ from the laser to measure the background gas signal, which is the fraction of gas leftover from the previous pulse that has not been pumped out yet. After images have been collected for all delays, six more images are collected. One with the pump beam blocked, one with the probe beam blocked, and one with both beams blocked, and their corresponding background images as well. These images allow for subtraction of different background signals, such as unwanted two or three photon contributions to the photoelectron spectrum from a single laser pulse. The collected set of images is called a scan,

and scans are repeated indefinitely until a sufficient signal-to-noise ratio is achieved.

3.5.1 VMI data pre-processing

The images were loaded into memory. The total photoelectron yield for each image is calculated by integrating over the whole image. A plot of total yield versus image number was created for diagnostics. Unusable scans (i.e. if the laser was accidentally blocked, if the pulsed valve malfunctioned etc.) can be removed from the dataset.

The image center was found in a two step process. First, an estimate was found by averaging the image stack into one image and finding its center of mass. This method works well on its own unless there is large detector inhomogeneity, which was the case for OCS. Figure 3.6 shows the average image stack, where the inhomogeneity is visible. Near the center, the bottom half of the image is more intense than the top half. The inhomogeneity is likely due to detector degradation from constant molecular beam bombardment.

In the second step, the average image was converted to polar coordinates, choosing several image centers in the neighbourhood of the estimate. The polar images are then examined for "waviness" and the center with the least wavy polar plot was chosen. Figure 3.7 shows an example polar plot for OCS with (a) minimal waviness and (b) severe waviness, with white dashed lines to guide the eye.

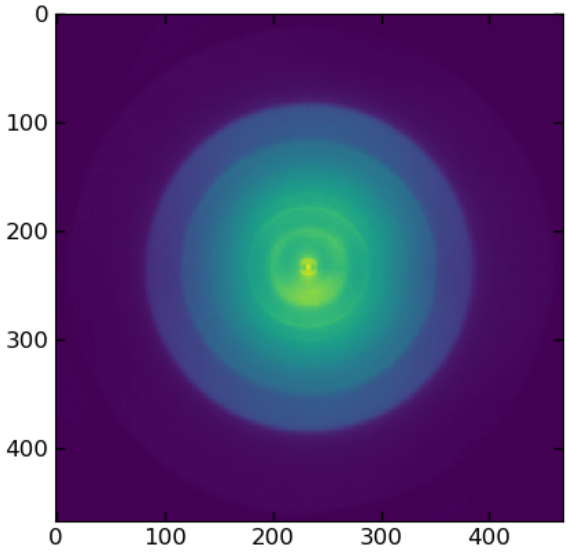

Figure 3.6: Raw VMI image of OCS averaged over all time delays. Note the vertical asymmetry near the center of the image, possibly caused by detector inhomogeneity.

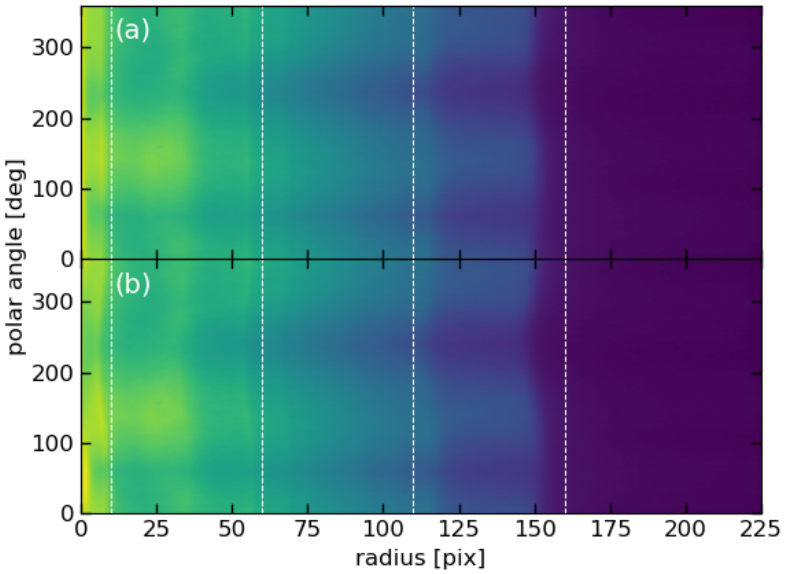

Figure 3.7: Polar plots of raw VMI images with (a) a good image center, and (b) a poor image center. Note the waviness in (b) compared to (a). White dashed lines are a guide for the eye.

The images were background subtracted by the "no-beam" image (where both lasers were

blocked) collected at the end of each scan. They were then cropped to 480×480 pixel square images and rotated such that the laser polarization axis was vertical. This further reduced the images to 468×468 pixels. They were then 4-fold symmetrized by summing the four quadrants together in the correct orientation and dividing by 4, in preparation for the Abel inversion.

A fast matrix inversion algorithm[42] was used to Abel invert the images. Since the image is 4-fold symmetric, only the upper right quadrant was inverted to reduce calculation time. Figure 3.8 shows the (a) non-inverted and (b) inverted images averaged over the image stack. Inverted images were then integrated angularly to retrieve the radial (velocity) spectrum. The spectra were then plotted as a function of time delay to produce a 2D photoelectron spectrum.

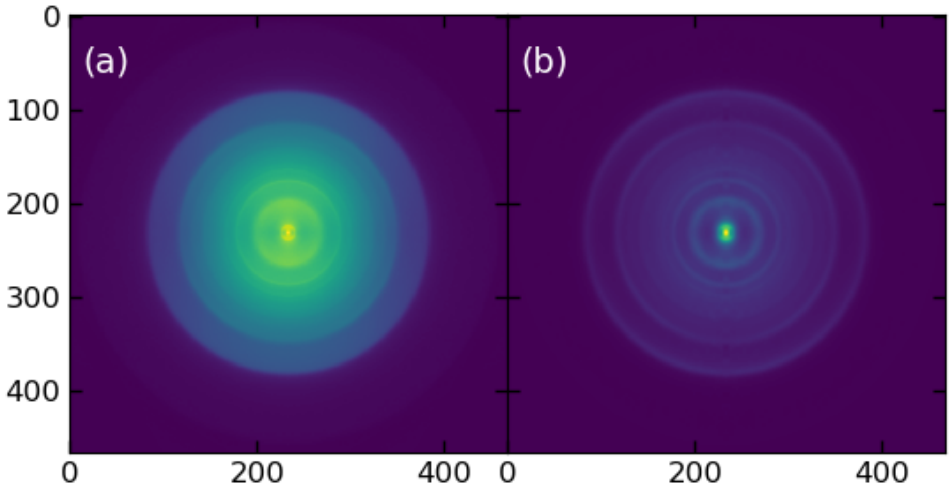

Figure 3.8: (a) Symmetrized image of OCS and (b) image after Abel inversion.

3.5.2 Xenon calibration

Xenon was used to calibrate the VMI pixel-to-energy conversion, the VUV wavelength, the absolute time-zero, and the cross-correlation (instrument response function). It was chosen for its relatively high ionization potential and its non-resonant nature at the wavelengths of interest. In this section the electronic structure of xenon will be described, followed by the calibration methods.

Xenon has a first excited state at 8.315eV (149.1nm), which is above the energy of both the VUV wavelengths as well as the 200nm. This makes two-photon ionization non-resonant for all possible pulse combinations in our setup. The emitted photoelectron energy will be exactly the difference between the ionization potential and the total photon energy. The non-resonant signal is useful for absolute time-zero and cross-correlation calibrations. In the time-dependent picture, the pump-probe photoelectron spectrum will be Gaussian with a maximum exactly when both pulses are perfectly overlapped in time, and whose full width at half maximum is the cross-correlation of the pulses.

The first ionization potential of xenon is 12.1298eV to the ground ionic state[55]. Xenon also has a well-known spin-orbit splitting between the $Xe^+(^2P_{3/2})$ and $Xe^+(^2P_{1/2})$ states, with the latter being 1.3064eV higher in energy[56]. Given the photon energies of 6.212eV (200nm), 8.025eV (154.5nm) and 8.130eV (152.5nm) used in the experiments, we expect no single photon transitions and all possible two-photon transitions, with the exception of two photons of 200nm to the $Xe^+(^2P_{1/2})$ state, as the energy is less than the ionization potential plus the spin-orbit splitting energy. A diagram of xenon's electronic structure and the relevant transitions is shown in Fig. 3.9.

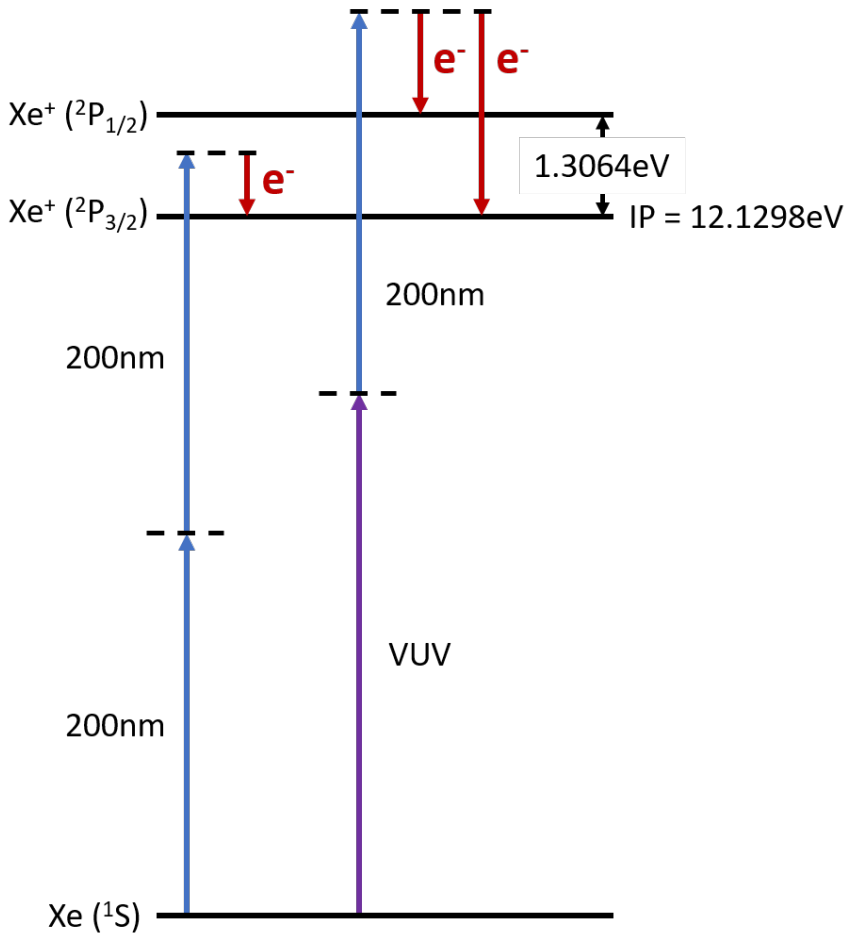

Figure 3.9: Energy diagram of xenon electronic structure, as well as the relevant transitions for our laser source.

The pixel-to-energy conversion was performed using pump-probe signal and the known xenon spin-orbit splitting energy. Since the radial position on the detector is proportional to the electron velocity, and energy is proportional to the velocity squared, the relation $E = Kr^2$ was used to convert detector radial position r to energy E, where K is the calibration constant. K was determined by fitting the two peaks with a Gaussian and solving the equation

$$K = \frac{\Delta E}{(r_2^2 - r_1^2)},$$

where ΔE is the spin-orbit splitting energy and r_1,r_2 are the radial positions obtained from

the Gaussian fits. Since the pixel-to-energy conversion is sensitive to the position of the interaction region, and the pointing of the lasers was reoptimized between experiments, a different K value was calculated for each individual experiment.

Two types of xenon scans were used to calculate the K value: an on/off scan and a time-resolved scan. The on/off scan was much faster than the time-resolved scan and has a much better signal-to-noise ratio. It was used to quickly determine and adjust the VUV wavelength, but the full time-resolved scan was necessary to determine the time-zero offset and the cross-correlation.

The on/off scan samples the photoelectron spectrum at two time delays. The first delay was at time-zero where maximum pump-probe signal is observed, while the second was sufficiently far away from any pump-probe signal (+260fs in our case). The off scan was used to background subtract the 2×200nm photoelectron signal for better contrast. Figure 3.10 shows a sample on/off scan with (a) no background subtraction and (b) background subtraction. Note the same peaks as labelled in Fig. 3.11. After background subtraction, a 1D spectrum is taken from the time-zero delay and Gaussians were fit to the pump-probe $^2P_{1/2}$ and $^2P_{3/2}$ peaks, followed by the pixel-to-energy conversion as stated above.

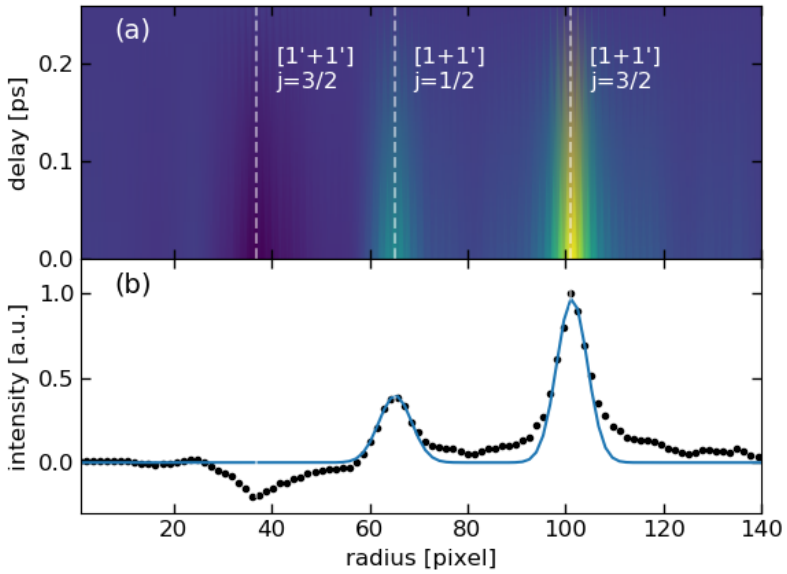

Figure 3.10: (a) Xenon background subtracted on/off scan, with excitations by 2×200nm [1'+1'] and VUV + 200nm [1+1'] labelled. (b) Background subtracted 1D slice of on/off scan, with Gaussian fits to the $^2P_{1/2}$ and $^2P_{3/2}$ peaks.

The wavelength calibration was done using the 1D spectrum converted to an energy scale and the equations

$$E_{VUV} + E_{200nm} - IP_{Xe} = E_{electron}$$

and

$$E_{VUV} + E_{200nm} - IP_{Xe} - E_{split} = E_{electron}$$

for $^2P_{3/2}$ and $^2P_{1/2}$ states, respectively. Both states were used as independent checks of the VUV wavelength. The non-background subtracted 2×200nm $^2P_{3/2}$ peak was used to verify the 200nm wavelength.

A sample time-resolved xenon photoelectron spectrum is shown in Fig. 3.11, partially background subtracted to highlight the contributions from 2×200nm [1'+1'] to $^2P_{3/2}$, and 152.5nm + 200nm [1+1'] to $^2P_{1/2}$ and $^2P_{3/2}$. Note the apparent large fluctuations in the [1'+1'] signal are small compared to the peak height and are only amplified by the background

subtraction. The pixel-to-energy conversion was performed in almost the same manner as the on/off scan. The data was background corrected by averaging negative time delays between -0.5ps and -0.25ps and subtracting it from the whole data set. A horizontal stripe was taken through the center of the time-resolved peaks and time-averaged to generate a 1D plot, where the same treatment as the on/off scan was used for pixel-to-energy conversion. Wavelength was calibrated in the same manner as well.

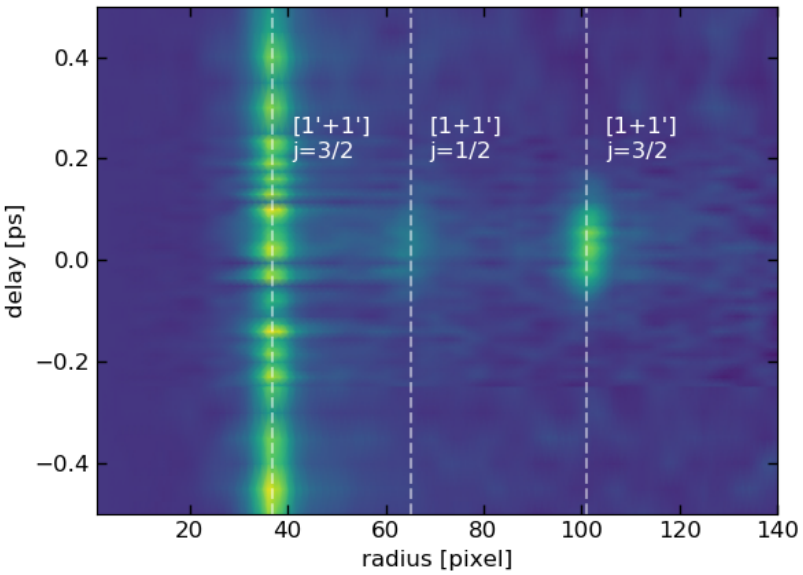

Figure 3.11: Sample xenon photoelectron spectrum with partial background subtraction to highlight the three observable states. Note the apparent large fluctuations in the [1'+1'] signal are small compared to the peak height and are only amplified by the background subtraction.

The cross-correlation and the time-zero offset were measured by taking a vertical (time) stripe along the [1+1'] $^2P_{3/2}$ peak. The stripe was energy averaged into a 1D time-trace and a Gaussian fit was performed. The position of the Gaussian peak was the time-zero offset and the full width at half maximum was the cross-correlation duration of the VUV pump with the 200nm probe. Figure 3.12 shows a sample cross-correlation trace and Gaussian fit.

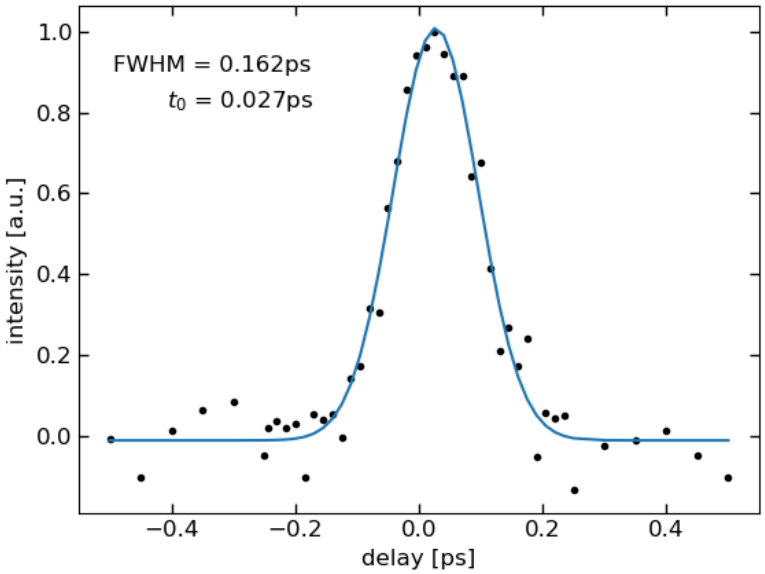

Figure 3.12: Sample time-zero offset (t_0) and cross-correlation (FWHM) from a Gaussian fit (blue line) to the [1+1'] $^2P_{3/2}$ peak (black dots).

3.6 Conclusion

The ultrafast tunable VUV source, coupled to a thick lens VMI spectrometer at the NRC was described. Procedures for using this source, including first finding VUV, optimizing generation, pump-probe alignment through the VMI spectrometer, sources of instability, strategies to mitigate them, data preprocessing and calibration of the VMI instrument were presented. The following chapter presents a TRPES study of OCS using the source and VMI spectrometer described in this chapter.

Chapter 4

VUV excited state dynamics of Carbonyl Sulfide

4.1 Introduction

Carbonyl sulfide (OCS) is a linear triatomic molecule, comprised of a central carbon atom double bonded to both a sulfur and an oxygen. It is the most abundant sulfur containing compound naturally occurring in the Earth's atmosphere[57–59] and thus plays an important role in the sulfur cycle[60]. As a long-lived species in the troposphere[61], it can ascend into the stratosphere to become a dominant source of sulfur to the stratospheric aerosol layer[62]. These aerosols have a significant impact on the Earth's radiative equilibrium, and thus understanding of the photochemical reactions of OCS subject to UV and VUV radiation is of scientific interest. Here we apply femtosecond Time-resolved Photoelectron Spectroscopy (TRPES) using a novel ultrafast VUV source to directly observe the excited state dynamics of OCS in the 8 eV region relevant to the upper atmosphere.

For our purposes, OCS will be a valuable test molecule for the new VMI instrument described in chapter 2. As will be seen later in this chapter, photoelectron photoion covariance measurements would have been a huge benefit to the understanding of the OCS photoelectron spectrum. We found strong evidence that part of the observed TRPES originates, unusually, from atomic sulfur autoionization. The ability to differentiate which electrons correlate to

which ions would give definitive proof to our hypothesis. We plan to use the OCS experiment presented in this chapter as a benchmark in the new machine, followed by a new covariance measurement to directly verify our sulfur autoionization assignment.

OCS is also an appealing candidate as a test molecule for time-resolved x-ray spectroscopy, which is emerging as a powerful approach to study molecular dynamics[63,64]. As x-ray spectroscopy is based on core shell transitions, it is sensitive to atom-specific local charge density variations of the dynamics. It is often argued in ultrafast X-ray science that the ability to tune to an atomic edge is a key advance. We propose to test this hypothesis directly, using OCS as a benchmark case. OCS is comprised of three distinct atoms each having different core shell transition energies. Tuning the x-ray energy to the 1s K-edge of each atom would provide three distinct perspectives of the overall excited state dynamics, in contrast to conventional valence shell spectroscopy which is sensitive to global changes in charge distribution. It would be very informative to explore the advantages and disadvantages of each type of spectroscopy. The aim of this chapter is to report a valence shell VMI study of the excited state dynamics of OCS, to be used as a benchmark for the direct comparison to x-ray spectroscopy measurements in future work.

4.2 Experimental Overview

The $^1\Sigma^+$ excited state dynamics of OCS were directly observed using time-resolved velocity map imaging (VMI) photoelectron spectroscopy. An ultrafast tunable VUV source was tuned to two different vibrational transitions of the $^1\Sigma^+$ excited state: the (1,1,0) state at 8.025eV (154.5nm) and the (2,1,0) state at 8.130eV (152.5nm), where (ν_1, ν_2, ν_3) are the symmetric stretch, bend, and asymmetric stretch modes respectively. The dynamics were then probed with an ultrafast photoionization pulse at 200nm (6.2 eV). The possible two-photon (termed a 1+1' process) signals are VUV+200nm, 2×VUV, and 2×200nm. The VUV pulse will be denoted as 1 and the 200nm as 1'. The relevant energy regions in OCS to examine are

at 1' = 6.212eV, 1 = 8.025eV (8.130eV), 1'+1' = 12.425eV, 1+1' = 14.238eV (14.344eV) and 1+1 = 16.052eV (16.262eV), where the numbers in parentheses correspond to the higher energy VUV pulse. In order to understand the TRPES spectra, it is important to understand the underlying electronic structure of the energetically allowed excited states and final ionic states. The following section will outline the relevant electronic structure and dipole-allowed transitions of OCS and OCS^+.

4.3 Literature Review

The neutral X $^1\Sigma^+$ ground state of OCS has a valence electronic structure of $(6\sigma)^2(7\sigma)^2(8\sigma)^2(9\sigma)^2(2\pi)^4(3\pi)^4$. The lowest unoccupied molecular orbitals are $(4\pi)^0$, $(10\sigma)^0$ and $(11\sigma)^0$, detailed by Feng and coworkers[65]. The first absorption spectrum of OCS was recorded by Lochte-Holtgreven and Bawn in 1932[66]. Since then, several photoabsorption studies have identified transitions to valence states as well as low lying Rydberg series converging on different states of the ion[67–71]. The most recent high resolution absorption spectra was measured by Limão-Vieira et al.[72]. They reported the absolute photoabsorption cross section of room temperature OCS from 4-10.8eV using synchrotron radiation, and will be the assignments used in this work. Figure 4.1 shows the absolute photoabsorption cross section of OCS with the three lowest energy electronic transitions labelled.

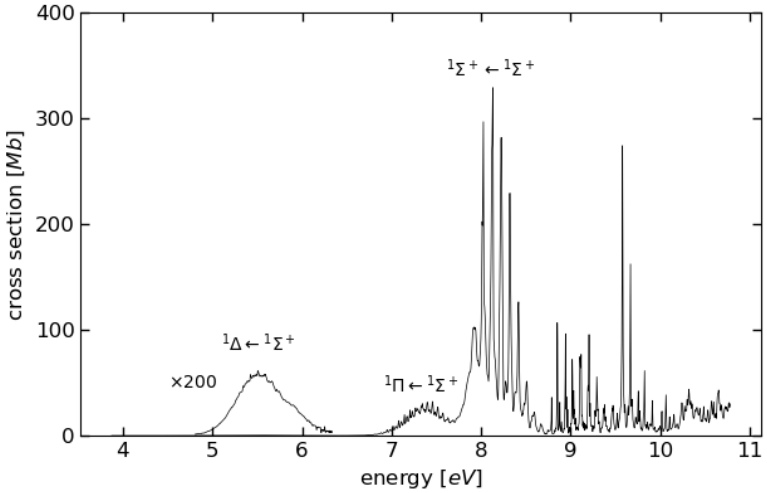

Figure 4.1: Absolute photoabsorption cross section of OCS in the 4-10.8eV range. The three lowest electronic transitions are labelled. Data are from Limão-Vieira et al[72].

The lowest energy transition is the dipole forbidden ($4\pi \leftarrow 3\pi$) ($^1\Delta \leftarrow^1 \Sigma^+$) transition, centered at 5.506eV with an absolute absorption cross section of 0.3Mb[72]. This state has gathered considerable interest due to its activity in the UV region, relevant to atmospheric chemistry. Several photodissociation experiments have been performed[73–77]. The state readily dissociates into S and CO fragments, with the sulfur produced exclusively in the S(^{1}D) state[78]. CO fragment vibrational distributions have also been measured, along with angular distributions of the photoproducts[79]. In our experiment, the 200nm probe pulse sits on the upper edge of this region which may contribute to the measured signal. However, given the relatively small cross section of this dipole forbidden transition, we assume no 200nm pumping contribution to the photoelectron spectrum.

The next transition is the ($10\sigma \leftarrow 3\pi$) ($^1\Pi \leftarrow^1 \Sigma^+$), centered at 7.458eV with a weakly allowed absolute absorption cross section of 32.3Mb[72]. Little information was found regarding this state, possibly due to the difficulty in producing photons in this energy region. This state is energetically inaccessible in our current experiments.

The electronic state of interest here is the strongly allowed ($4\pi \leftarrow 3\pi$) ($^1\Sigma^+ \leftarrow^1 \Sigma^+$)

transition that spans the energy range 7.7-8.7eV. A large cross section (329.2Mb) electronic transition exhibits a symmetric stretch vibrational progression (ν_1 = 0-8), combined with one quantum of the ν_2 bending mode[72]. Figure 4.2 shows the absorption spectrum of this band with red and blue dashed lines indicating the vibrational states (1,1,0) and (2,1,0) explored in the present work. The smaller peaks and shoulders are assigned to a ν_1 progression in the absence of the bending mode. The $^1\Sigma^+$ state is well-known to dissociate into S + CO. Black et al.[80] reported a high quantum yield (>0.8) of S(^{1}S) photoproducts in 140-160nm region, corroborated by Yamanouchi et al.[81,82]. The first transition at 157nm has been widely studied[83–86], mostly due to the easily accessible F_2 excimer laser emission at that wavelength. The development of tunable VUV sources using resonant four-wave mixing allowed Yamanouchi and coworkers to investigate the dynamics of the $^1\Sigma^+$ excited state by pumping with this method and probing the S(^{1}S) photoproduct yield via laser induced fluorescence[87]. They reported the indirect measurement of vibrationally-resolved excited state lifetimes between 27-133fs, based on the linewidths of the S(^{1}S) photofragment action spectrum (i.e. the yield as a function of wavelength). The Fourier transform of the S(^{1}S) action spectrum yielded a vibrational period of 42fs for the transition state, which was defined as the unstable periodic orbit along the reaction coordinate perpendicular to the dissociation coordinate. Data were supported by ab-initio calculations of the $^1\Sigma^+$ excited state potential energy surface, which resulted in a repulsive surface along the C-S coordinate and a wide plateau along the C-O stretching coordinate. Wavepacket simulations resulted in a symmetric stretch vibrational motion with a period of 48fs orthogonal to dissociation, in good agreement with experiment. However, no mention of the bending mode is made, in possible disagreement with the assignment of one quanta of bend to the vibrational progression by Limao-Vieira et al. Xie and coworkers investigated S photofragments in the same wavelength region using time-sliced velocity map ion imaging[88]. They noted that the dissociation of OCS from the $^1\Sigma^+$ state adiabatically correlates to the S($^1S_0$) + CO(X $^1\Sigma_g^+$) channel, while the

calculated anisotropy parameters are positive and decrease from nearly 2 to 0 with increasing CO product vibrational state, suggesting that a bent transition state may be involved in the formation of products at higher vibrational states of CO products.

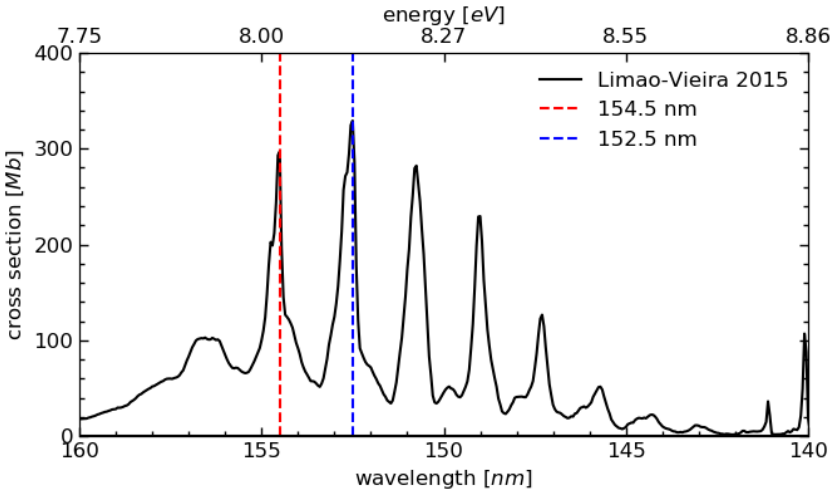

Figure 4.2: Absolute absorption cross section of OCS in the 7.7-8.7eV range, corresponding to the $(4\pi \leftarrow 3\pi)$ $(^1\Sigma^+ \leftarrow ^1\Sigma^+)$ transition. The VUV pump wavelengths of 154.5nm and 152.5nm used here are denoted by the red and blue dashed lines, respectively. Data are from Limão-Vieira et al[72].

From 8.7-10.8eV there are several vibrational progressions with Rydberg states superimposed. Yang et al. reported a multiphoton ionization study combined with photoelectron spectroscopy to investigate these vibronic bands and their mixing with the Rydberg states[89]. These higher lying states are energetically inaccessible in our experiment and therefore beyond the scope of this work.

In pump-probe experiments, it is important to note that the projection of the excited state dynamics is onto a final state: the probability of being in a given final state is measured as a function of the pump-probe delay. For the case of photoionization, the final state is the molecular ionization continuum. This is often approximated as a direct product state of a cation quantum state times a free electron quantum state. In a sense, the electron is often

treated as a 'spectator', there to conserve energy and angular momentum. However, this direct product continuum approximation is not always applicable. As will be shown for the case of OCS, there can be a rich structure with different electronic states of the ion, each with their own vibrational progressions, as well as many superexcited Rydberg states (quasi-bound autoionizing or predissociating states above the ionization potential). It is therefore necessary to understand the energetic structure of the molecular ionization continuum in order to understand the projection of the excited state onto the final state by the probe laser.

The energetically accessible electronic states of OCS^+ are: X $^2\Pi$, which has a spin-orbit splitting with ionization energies of 11.1824eV and 11.2279eV for the j =3/2 and j=1/2 states, respectively[90]; A $^2\Pi$, which also has spin-orbit splitting with ionization energies of 15.0759eV for j=3/2 and 15.0901eV for j=1/2[91]; and B $^2\Sigma^+$, which has an ionization energy of 16.0403eV[91]. As the spin-orbit splitting is roughly 40meV for the X $^2\Pi$ state and 20meV for the A $^2\Pi$ state, we do not expect to resolve these features in our broad band femtosecond experiments. Rather, we expect the splitting to broaden and redshift the electronic origin peaks in our photoelectron spectra.

A large variety of photoelectron studies have been performed above the ionization potential of OCS. Y. T. Lee et al. reported high resolution HeI (21.4eV) photoelectron spectrum of OCS^+[92]. They found a very large singly peaked absorption line associated with the B $^2\Sigma^+$ state, indicating that the neutral ground state shares very similar geometry. Eland et al. performed a PEPICO experiment measuring ion yield in coincidence with photoelectron yield[93]. They found that photoelectrons associated with the X $^2\Pi$ state to correlate almost exclusively with OCS^+ ions, whereas the A $^2\Pi$ and B $^2\Sigma^+$ states correlate almost exclusively with S^+ ions. Superexcited Rydberg states have been extensively studied[70,94–97]. Holland and Shaw report the most recent absolute photoabsorption, photoionisation and photodissociation cross sections in the 11-24eV region using synchrotron radiation and a double ion

chamber[98]. They identified several Rydberg series converging to the B $^2\Sigma^+$ state of the ion but found none converging to the A $^2\Pi$ state. The final states closest to our 1+1' energy of 14.238eV (14.343eV) are Holland's series IV n=3 ndσ at 13.9-14eV, and the series V n=4 nsσ at 14.4eV, using their notation. The series IV n=3 state has 3 peaks attributed to a vibrational progression in the bending mode. While the energies of the observed Rydberg states do not match our 1+1' photon energy exactly, we note that the initial state in Holland and Shaw differs from ours. They reported a direct single photon transition from the neutral ground state to the superexcited Rydberg states. In our case, we have an intermediate transition to the vibrationally excited $^1\Sigma^+$ state, which was subsequently photoionized, in other words a resonant two-photon ionization. The initial vibrational wavefunction (i.e. the state being ionized) differ in these cases, implying different Franck-Condon factors must be involved. In our case, we expect that there will be transitions to superexcited Rydberg states with a higher vibrational quantum numbers than seen in the ground state absorption spectra of Holland and Shaw. Direct transitions from the ground state will likely have poor overlap with higher vibrational quantum numbers of the superexcited Rydberg states compared to transitions from the vibrationally excited intermediate state. For a more detailed discussion of the Franck-Condon factors involved, see section 4.4.1.

Molecular and photoproduct autoionization was studied in superexcited OCS by Hikosaka et al.[97,99]. They employed a 2D photoelectron spectrum measurement technique using synchrotron radiation and a hemispherical analyzer. They plotted the photoelectron yield as a function of the photon energy on the vertical axis and the photoelectron kinetic energy on the horizontal axis, which allowed for a clear distinction of three different ionization mechanisms. Direct ionization appeared as a diagonal stripe in the spectrum as the photoelectron kinetic energy is directly proportional to the photon energy minus the ionization potential. Horizontal stripes (constant photon energy) indicated autoionization of OCS* Rydberg states. This likely occurs through internal conversion to other autoionizing states which emit photo-

electrons of different kinetic energy at the same photon wavelength. Vertical stripes, where photoelectrons were emitted with a fixed kinetic energy independent of photon energy, indicated an S* atomic autoionization process. The mechanism of action in this case is the excitation of OCS*, predissociation into S* + CO fragments followed by autoionization of S* into S^+. Several vertical stripes were reported and assigned to superexcited sulfur Rydberg states converging on the first excited state S^+ (^2D_o) of the ion.

To the best of our knowledge, no femtosecond time-resolved experiments have been performed on the OCS $^1\Sigma^+$ excited state. This is likely due to the difficulties in producing the tuneable femtosecond VUV pulses, as described in the previous chapter. Our VUV source places us in a unique position to perform the first time-resolved photoelectron VMI experiments which directly measure the OCS $^1\Sigma^+$ excited state lifetimes for different vibrational states.

4.4 Basic TRPES Theory

The following sections describe some basic theory surrounding TRPES and VMI relevant to the OCS experiments.

4.4.1 The Born-Oppenheimer and Franck-Condon Approximations

When dealing with electronic and nuclear (vibrational) dynamics in molecules and solids, the Born-Oppenheimer approximation (BOA) is often used. The BOA is an adiabatic approximation wherein certain degrees of freedom are treated as being 'slow' with respect to others. Conceptually, since the mass of the electrons is much smaller than that of the nuclei, the electrons are able to 'instantaneously' adjust the the slow-moving nuclei. Mathematically, the BOA allows for the approximate separation of the electronic and nuclear variables wherein the electronic degrees of freedom depend only parametrically on those of the nuclei. We can write the total wavefunction (ignoring spin) as a function of the electronic coordinates r and

nuclear coordinates R as

$$\Psi_{total}(r, R) = \chi(r, R)\phi(R),$$

where Ψ_{total}, χ and ϕ are the total, electronic and nuclear wavefunctions, respectively. The separation of electronic and nuclear wavefunctions allows the calculation of the potential energy surfaces by solving the electronic Schrödinger equation over the electronic coordinates, while parametrically varying the nuclear coordinates to map out the potential energy surface. The BOA is only valid if the potential energy surfaces are well separated in energy, and thus breaks down at curve crossings where non-adiabatic coupling between electronic and nuclear degrees of freedom becomes large, such as in the vicinity of conical intersections.

The Franck-Condon principle builds on the BOA, further stating that electronic dipole transitions are instantaneous compared to the timescales of nuclear motion. This means that the nuclei are 'frozen' during the electronic transition and therefore the nuclear wavefunctions of the initial and final states must overlap to some degree for a transition to occur. In a semiclassical picture, these transitions occur at the stationary phase points of the nuclear (radial) overlap integral. In other words, the value of the Franck-Condon overlap integral accumulates predominantly when the phase of the integrand (product of vibrational wavefunctions) is stationary: this occurs when the nuclear kinetic energy is 'instantaneously' the same in the initial and final vibrational states. Using ket notation, the generalized transition dipole moment is

$$\langle \Psi'_{total}(r, R)|\mu_e(r, R)|\Psi_{total}(r, R)\rangle \,,$$

where μ_e is the electronic dipole operator and the prime denotes the final state. Rewriting in terms of the BOA where $\phi(R)$ are the nuclear wavefunctions and $\chi(r, R)$ are the electronic wavefunctions:

$$\langle \phi'(R)| \langle \chi'(r, R)|\mu_e(r, R)|\phi(R)\rangle |\chi(r, R)\rangle \,.$$

Integrating first over the electronic degrees of freedom, we can write

$$\langle \phi'(R)|\mu_e(r,R)|\phi(R)\rangle = \mu_e(R),$$

where $\mu_e(R)$ is now parametrically dependent on nuclear coordinates. In the Franck-Condon approximation, we replace $\mu_e(R)$ by its expectation value $\langle \mu_e \rangle$ which is now coordinate independent. This therefore leave the transition probability is the form

$$\langle \mu_e \rangle \langle \phi'(R)|\phi(R)\rangle .$$

The part of the expression involving only $\phi(R)$ is the overlap integral of the nuclear wavefunctions between the initial and final state, the square of which is called a Franck-Condon factor. The Franck-Condon factors determine which vibrational states of the excited electronic state are accessible given the initial vibrational states. As an example, most photoelectron studies of OCS are based on single photon ionization from the ground state. In our experiment, OCS is ionized in a two-photon process, resonantly passing through a vibrationally and electronically excited state before being ionized. In the single photon case, the overlap is between the geometry of the neutral ground state and the final ionic state. With two photon ionization, there is an intermediate geometry change which will affect results in different Franck-Condon factors and thus different vibrational transition probabilities to the final states of the molecular ionization continuum.

4.4.2 Group Theory and Symmetries

One of the reasons VMI is a powerful tool is that it allows for the measurement of the photoelectron angular distributions (PADs). Typically, when an outgoing photoelectron is far away from the ion from which it originated, it 'feels' only the long range monopole term in the otherwise complex molecular potential – the Coulomb 1/r potential. As the Coulomb

potential is spherically symmetric, it is appropriate to describe the outgoing photoelectron in a spherical basis: these are the angular momentum states, spanned by the spherical harmonics, and are typically called the partial waves. The PADs provide information on the partial wave characteristics of the outgoing electrons. The final ion electronic state determines which partial waves symmetries are allowed (i.e. the non-zero matrix elements of the dipole transition operator), given the symmetries of the initial excited neutral state and the dipole operator. As will be shown for OCS, we can use this information to determine, for example, whether the observed photoelectrons were emitted from true continuum or Rydberg final states.

OCS belongs to the $C_{\infty v}$ point group. In this point group, the ground state, the $^1\Sigma^+$ excited state, and the parallel (z) dipole operator are all A1 symmetry. For the overall symmetry product to be A_1 (i.e. totally symmetric for an allowed transition) , the dipole transition must be parallel (The perpendicular (x,y) dipole is E_1). Since the probe laser is polarized parallel to the pump, we can assume the probe dipole operator is also parallel. Starting from the A_1 excited state, with an A_1 dipole transition, the symmetry allowed electron partial waves are:

- To ion X $^2\Pi$ state (E_1 symmetry): E_1 photoelectrons
- To ion A $^2\Pi$ state (E_1 symmetry): E_1 photoelectrons
- To ion B $^2\Sigma^+$ state (A_1 symmetry): A_1 photoelectrons

Decomposing the point group symmetry into atomic species, E_1 yields p and d waves whereas A_1 yields s and d waves. Therefore, a transition to the X $^2\Pi$ or A $^2\Pi$ cation electronic states correlates with p and/or d electron waves, whereas a transition to the cation electronic B state correlates with s and/or d waves. In terms of superexcited Rydberg states converging on B $^2\Sigma^+$, we would expect transitions to states with ns or nd character. However, the

angular momentum of autoionized photoelectrons from these states depends on the nature of the autoionization process and may not reflect the character of the state it originated from.

For further reading on the topic of point group symmetry and group theory, Appendix D of the book *Electronic and Photoelectron Spectroscopy* provides a useful summary and was the basis for this section[100].

4.4.3 Anisotropy Parameters

VMI does not measure the photoelectron partial waves directly. As stated earlier, it measures the PADs, which are only related to the partial waves. For the case of parallel pump and probe laser polarizations, cylindrical symmetry applies. The PADs are characterized by the phenomenological anisotropy parameters, which are defined by the equation

$$I(\theta) = \sum_{L=0}^{2N} \beta_L P_L(\cos\theta), \tag{4.1}$$

where $I(\theta)$ is the angular dependent intensity in cylindrical symmetry, β_L is the L^{th} anisotropy parameter and $P_L(\cos\theta)$ is the L^{th} legendre polynomial. Only even terms in the sum are required as linear (in the field) dipole interactions guarantee left-right (or up-down) symmetry. The sum is terminated at 2N, where N is the number of photons in the interaction, according to Yang's Theorem[22].

To fit the anisotropy parameters, the Abel inverted images were transformed to polar coordinates. Equation 4.1 was then fit to the polar image using a least squares fitting routine. Even terms up to β_6 were included even though we have a two-photon process. β_6 was used therefore as an estimate of the systematic errors in the fits, since three photon processes should not contribute. If β_6 is nonzero either three photon processes are actually contributing or there are systematic errors in the image which contributes to anisotropy. We note that the particular Abel inversion algorithm used concentrates noise along a central vertical stripe in the image, which may contribute to the anisotropy.

The mapping of the anisotropy parameters to electron partial waves is not one-to-one. s waves contribute to β_0 only, p waves can contribute to β_2 and β_0, and d waves can contribute to β_4, β_2 and β_0. Symmetry arguments say nothing about the amplitudes and phases of each partial wave and how they contribute to each anisotropy parameter: group theory only states only which ones will vanish. Therefore, one must be careful not to assume, for example, that a β_2 contribution in the absence of β_4 is definitive proof for p wave over d wave photoemission.

4.5 Laser and VMI Parameters

Table 4.1 summarizes the measured laser parameters for both VUV wavelengths before and after the OCS data collection. The laser conditions did not change drastically during the experiment, indicating stable operation. In the fitting procedure, the average time-zero offset was used to correct the time delay axis and the average cross-correlation FWHM was used for the instrument response function.

Table 4.1: Laser parameters for both VUV wavelengths measured before and after OCS data collection.

Pump			Probe		Cross-Correlation	
λ_{target} [nm]	$\lambda_{meas.}$ [nm]	$\Delta\lambda_{FWHM}$ [nm]	$\lambda_{meas.}$ [nm]	$\Delta\lambda_{FWHM}$ [nm]	t_0 [fs]	FWHM [fs]
152.5 before	152.52	1.5 (80meV)	199.59	1.7 (50meV)	27.4	163.5
152.5 after	152.46	1.5 (80meV)	199.60	1.7 (50meV)	27.1	158.3
154.5 before	154.49	1.5 (80meV)	199.92	1.7 (50meV)	-13.2	153.9
154.5 after	154.40	1.5 (80meV)	199.87	1.7 (50meV)	-11.3	149.7

The VUV bandwidth was measured using the VS7550 VUV spectrometer and the 200nm bandwidth was measured with the Ocean Optics HR4000 spectrometer. The combined bandwidth of the pump + probe was 94meV and the combined bandwidth of two photons of VUV was 113meV (calculated by adding the bandwidths in quadrature). These combined bandwidths are only estimates as both pulses are chirped, as evidenced by a cross-correlation much longer than expected for transform limited pulses of the listed bandwidths, predominantly due to the input window on the VMI apparatus. This is unsurprising as neither pulse is chirp

compensated following its generation.

A 1% OCS seeded in helium gas mixture was used with a backing pressure of 28PSI in the pulsed valve. The valve was heated to 50 °C with a 16.8 µs opening time. The VMI voltages were set to collect 10eV electrons at the maximum radius of the detector (see Table 3.1). The MCP gain was set at 1700V and the phosphor screen at 4000V.

4.6 Mass Spectra

Mass spectra were recorded to check for molecular clusters in the gas jet. This was done in-situ in the VMI instrument. The electrode potentials were reversed and adjusted to accelerate ions towards the MCP in a spatial imaging mode. The potentials used are listed in Table 3.1. The ion arrival times were measured using a fast oscilloscope (Tektronix DPO 7354) via a capacitive pickoff attached to the phosphor screen.

OCS has an atomic weight of 60amu. We found that a 1% mixture of OCS seeded in He provided adequate signal without the formation of clusters whereas a 2% mixture showed the onset of clusters. Figure 4.3 shows the mass spectra recorded for (a) 1% mixture and (b) 2% mixture. The main feature observed is a large peak at 60amu indicating a large production of OCS^+ cations. There is a small neighbouring peak at 62amu assigned to OCS^+ with the ^{34}S sulfur isotope, which occurs naturally at an abundance of 4.2%. In panel (b) there is onset of a peak at 120amu indicating the formation of the $(OCS)_2^+$ dimer. A small amount of SO_2 contamination was observed but deemed insignificant. The small peaks labelled x are unknown contaminations. Note that the dimer peak is not exactly at 120amu, likely due to calibration error.

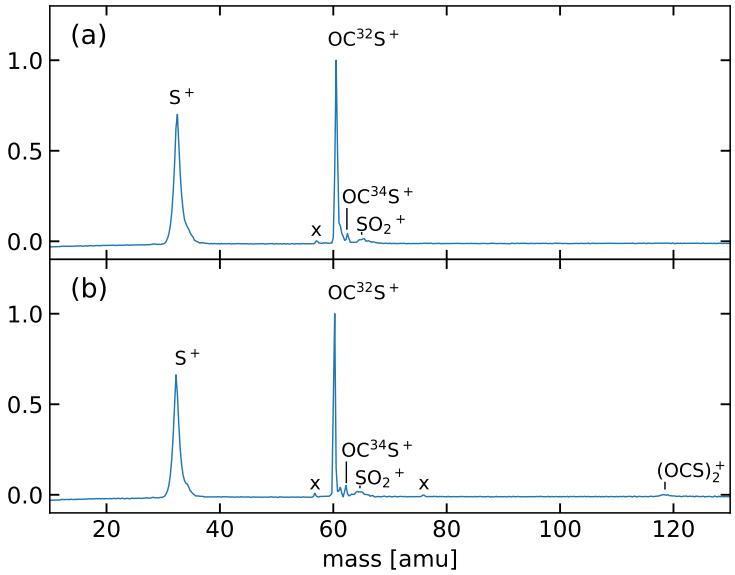

Figure 4.3: Mass spectrum of OCS at 154.5nm at (a) 1% concentration and (b) 2% concentration. The onset of OCS dimers can be seen at 120amu in (b). We also see a small peak corresponding to SO2 contaminations as well as two unknown peaks labelled x.

There are two potential mechanisms which lead to sulfur ionization after VUV excitation to the $^1\Sigma^+$ state. The first possibility is dissociation into CO and S(^{1}S) fragments followed by absorption of a second photon by the sulfur atom. The ionization energy from the S(^{1}S) state is 7.61eV, which means sulfur ionization is only accessible by another VUV photon and not a 6.2eV 200nm photon. As the VUV pulse duration is on the order of 50fs, the probability that OCS absorbs a VUV photon, dissociates, then the dissociation product sulfur atom absorbs another VUV photon from the same 50fs laser pulse seems rather unlikely. The second possibility is absorption of two photons by the OCS molecule, resonantly passing through the $^1\Sigma^+$ excited state into a superexcited Rydberg state. The superexcited state subsequently either autoionizes to form OCS^+ or dissociates into CO and S*, where S* is a superexcited state of sulfur. S* can then autoionize to S^+. We believe the latter is the relevant mechanism in our experiment.

CO fragments were not observed in the mass spectrum as their ionization potential from

the ground state is 14eV, energetically inaccessible in this experiment.

4.7 Results and Discussion

In this section we analyze the time-resolved photoelectron spectrum of OCS in three different energetic regions. Figure 4.4 shows an example raw 2D photoelectron spectrum with no background subtraction for the 152.5nm dataset, from which the three categories were assigned. The first category will be the 1+1 VUV only 1D spectrum, which comes from summing over negative time delays i.e. when the 200nm arrives before the VUV. Since there is no resonant transition at 200nm, only the two-photon VUV photoelectron spectrum is observed. This will be called the background spectrum. The second category will be the 1+1' time-integrated spectrum, which comes from background subtracting and then time-averaging the time-dependent 2D TRPES spectrum into a 1D energy-resolved photoelectron spectrum. This will be used to discuss the energetics and the proposed ionization mechanisms. The third category will be the 1+1' time-resolved 2D spectrum, which contains the details of the excited state dynamics.

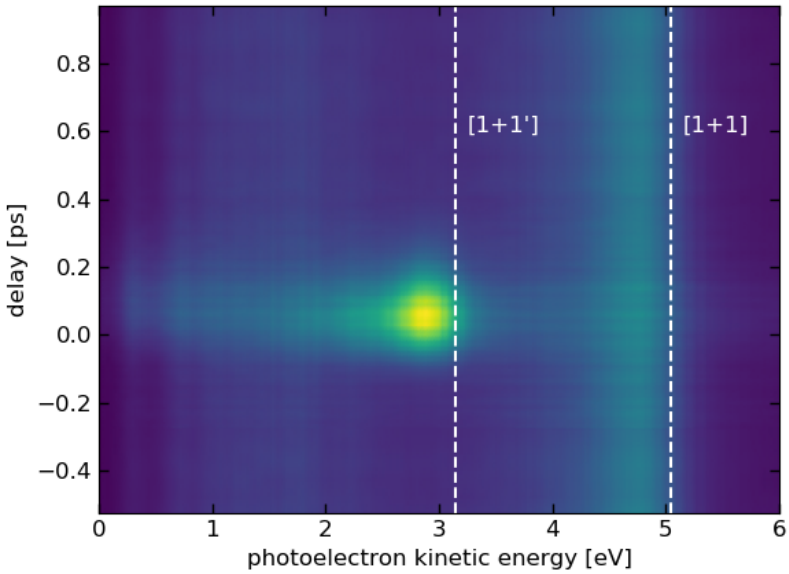

Figure 4.4: Non-background subtracted time-resolved photoelectron spectrum of OCS pumped at 152.5nm. The white dashed lines indicated cut offs for the 1+1' and 1+1 photon energies.

4.7.1 1+1 VUV only Static Photoelectron Spectra

The 1+1 VUV only photoelectron spectra were extracted from the time-resolved spectrum by averaging over negative time delays from -0.5ps to -0.25ps. The negative time delays correspond to the 200nm probe pulse arriving before the VUV pump, where the probe alone does not contribute to the photoelectron signal. The spectra are shown in Fig. 4.5.

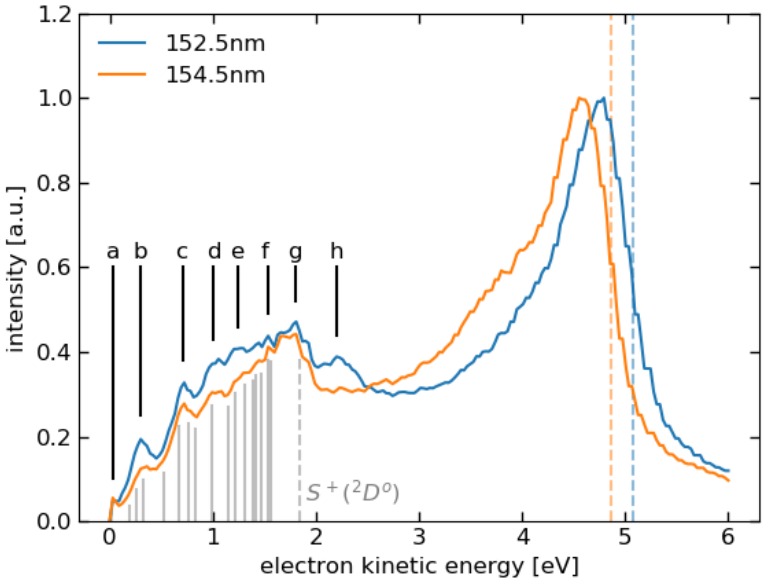

Figure 4.5: 1+1 VUV only background photoelectron spectrum for 154.5nm and 152.5nm pump wavelengths. Dashed orange and blue lines represent the two-photon VUV energy cut off. The grey lines represent sulfur Rydberg states converging on the S^+ (^2D_o) state, as measured by Hikosaka et al.[97]. The grey dashed line is the S^+ (^2D_o) state energy. Peaks a-h are discussed in the text.

The largest feature we observe is a peak at 4.6eV (4.8eV) for the 154.5nm (152.5nm) pump. That these peaks occur at different energies indicates that the mechanism is direct ionization to the continuum and not a resonant transition to a superexcited Rydberg state. The photoelectron kinetic energy cutoff for a two-photon VUV excitation is 4.9eV (5.1eV), which is 300meV greater than the observed peaks. A possible contribution to this apparent shift is the unresolved spin-orbit splitting of the $^2\Pi_{3/2}$ and $^2\Pi_{1/2}$ cationic ground states, which are expected to be populated equally. The splitting is 50meV which remains unresolved in our experiment but will appear as a peak broadening and red shifting. This does not account for the full 300meV shift. Thus, a second explanation is proposed: the $^1\Sigma^+$ vibrationally excited states will have transition probabilities to vibrationally excited states of the X $^2\Pi$ cation electronic ground state. A calculation of the Franck-Condon factors could verify this hypothesis.

Figure 4.6 shows the anisotropy parameters (a) β_2, (b) β_4 and (c) β_6 for the VUV only background. Focussing on the 4.6eV (4.8eV) peak, there is a β_2 contribution of 0.4 and no β_4 contribution. Pure s-wave photoemission is isotropic and would correspond to $\beta_2 = \beta_4 = 0$. The observed β_2 is consistent with a p wave, but does not rule out d wave emission. A p wave emission is consistent with direct ionization to the X $^2\Pi$ ionic ground state. Phenomenologically, it is often observed that the lower angular momentum partial wave has a larger contribution, as less torque has to be transferred to the departing photoelectron. Therefore the observed β_2 contribution supports the evidence for direct ionization over a transition to a superexcited Rydberg state.

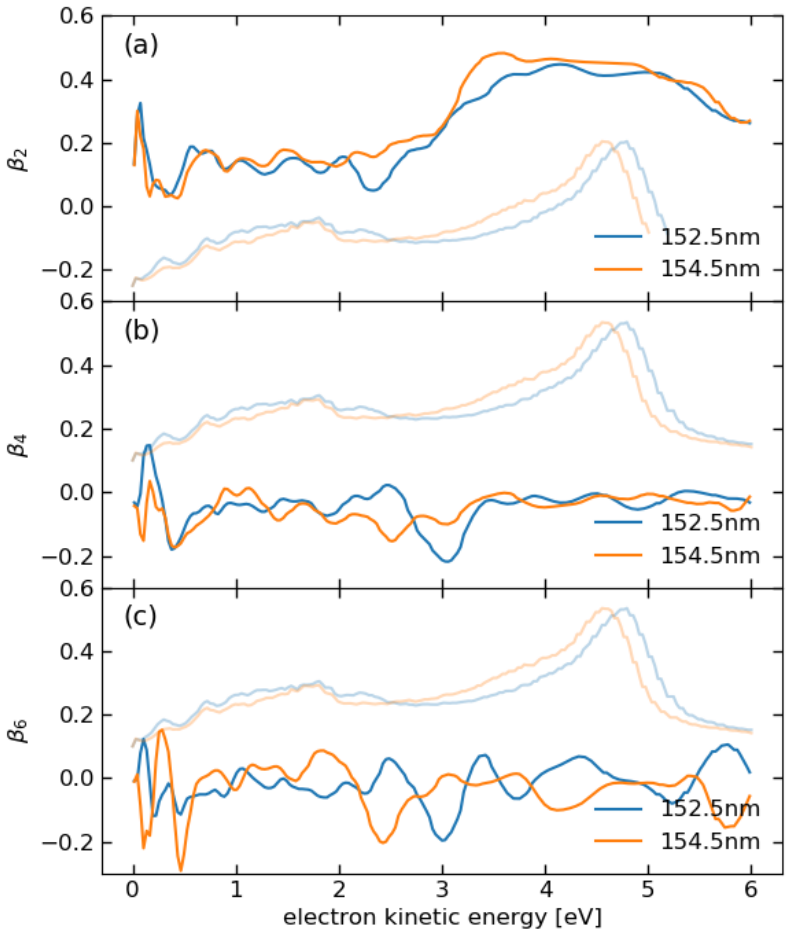

Figure 4.6: Anisotropy parameters (a) β_2, (b) β_4 and (c) β_6 for both wavelengths of the VUV only background photoelectron spectrum [-0.5,-0.25] ps. The transparent coloured lines are the corresponding VUV only background photoelectron spectra for reference only.

From 0 to 2eV, the photoelectron spectrum in Fig. 4.5 appears invariant with respect to the VUV wavelength. Four mechanisms possibly explain this behaviour:

1. Direct ionization to a vibrationless cationic state, where both pump-probe pair bandwidths overlap with the same cationic state. This is unlikely as the bandwidths do not overlap significantly.

2. Direct ionization to vibrationally excited ionic states. This has the possibility of projecting the different vibrational excitations of the $^1\Sigma^+$ state onto vibrationally excited ionic states that could release electrons with the same kinetic energy. An example of this would be (1,1,0) B $^2\Sigma^+ \leftarrow$ (1,1,0) $^1\Sigma^+$ and (2,1,0) B $^2\Sigma^+ \leftarrow$ (2,1,0) $^1\Sigma^+$, provided ν_1 and ν_2 are similar in both electronic states. This case is plausible for a small number of peaks, but unlikely for a series of peaks as the vibrational constants will differ causing some of the peaks to offset.

3. Molecular autoionization based on a non-radiative transition in the molecular ion. Here we would expect to observe OCS^+ ions, and correlated photoelectrons having kinetic energies independent of wavelength.

4. Molecular predissociation followed by atomic autoionization. As stated in section 4.3, sulfur autoionization from superexcited OCS* were observed[97,99]. A superexcited state OCS* can dissociate into neutral CO (X $^1\Sigma^+$) and superexcited S*, which subsequently autoionizes into $S^+ + e^-$. The emitted photoelectrons will have specific kinetic energies dependent on which superexcited S* state they originated from and not on the total 1+1' photon energy.

The assignment of the photoelectron peaks a-h in relation to mechanisms 1-4 above are discussed in the following paragraphs.

There is a small peak at close to zero kinetic energy (0.045eV, labelled a) in Fig. 4.5. Given that the energy of the B state of the ion is 16.04eV and the total photon energy is 16.05eV (16.26eV), this peak could correspond to a resonant ionization to the B state of the ion via mechanism 2, to account for the different VUV wavelengths. Since the photon energy is at or above the B state, transitions to Rydberg states converging on the B state are ruled out (mechanism 3). Furthermore, there are no sulfur Rydberg states close to the sulfur ionic ground state, thus mechanism 4 is ruled out as well. Eland et al.[93] reported a

very large singly peaked photoelectron yield for direct ionization from the neutral ground state to the B state. This would indicate very similar geometry between the neutral ground and ionic B state. We may then expect a much larger yield than seen in Fig. 4.5, however, the two-photon ionization process through an intermediate excited state will have different Franck-Condon probabilities compared to the single-photon ionization scheme of Eland and coworkers. The $^1\Sigma^+$ excited state clearly has a geometry different from the neutral ground state, as evidenced by the vibrational progression in the VUV absorption spectrum Fig. 4.2.

In Fig. 4.6, we see a positive β_2 contribution in this energy region, similar to the energy range of 3-5eV, as well as a β_4 contribution, which provide some evidence of d waves and hence direct ionization to the B state. Care must be taken when interpreting the anisotropy parameters, however, as there appears to be a noisy β_6 in the same energy region: a three photon process with nearly zero kinetic energy electrons may be contributing to this peak. There may also be a noise contribution from the inverse Abel transform. Since the peak is near the center of the image, a much smaller number of pixels are involved in the fit than are at larger radii. Coupled with the inherent centerline noise of the Abel inversion algorithm, this could be the source of the β_6 contribution. The assignment of this peak is therefore deemed speculative. Repeating the experiment at different VUV intensities would help to confirm or refute the posited three photon contribution.

There is a series of sharp peaks at 0.30eV, 0.72eV, 1.06eV, 1.24eV, 1.54eV and 1.81eV labelled b-g in Fig. 4.5. We believe these peaks are due to sulfur autoionization via mechanism 4. The peaks are independent of VUV wavelength, indicating an autoionization process. They are relatively sharp compared to the other structure in the PES, possibly indicating an atomic origin of the features. As noted earlier, a mass spectrum was measured with significant sulfur ion species observed. The vertical gray lines in Fig. 4.5 represent superexcited sulfur Rydberg states as measured by Hikosaka et al.[97]. The sulfur Rydberg states are converging on the first excited state S^+ (^2D_o) and autoionizing to the $S^+(^4S_o)$ ground state.

The maximum electron kinetic energy release in this process is the energy difference between $S^+(^2D_o)$ and $S^+(^4S_o)$, which is 1.84eV[101], and is indicated by the dashed gray line. This cutoff is just above peak g and where the spectrum starts to depend on VUV wavelength. The peaks appear to blend together as they approach the cutoff, which is consistent with the fact that a Rydberg series has inifinitely many states which approach an infinitessimal energy spacing as they converge to the ionic state. Given the energy resolution of our VMI spectrometer (estimated at 50meV) and the resolution of 50meV of Hikosaka et al., we do not expect the states to be perfectly aligned and we do not expect to resolve closely spaced Rydberg states.

Peak h only appears at the 152.5nm pump wavelength. We do not have a proposed assignment at this time.

4.7.2 1+1' Pump-probe time-averaged signal

Figure 4.7 shows the background subtracted, time-integrated VUV + 200nm (1+1') photoelectron spectrum. Similar to the low kinetic energy region of the two-photon VUV spectrum, the pump-probe spectrum is also invariant with respect to VUV wavelength. There is a large peak centered at 2.9eV with a shoulder extending to 0.3eV. For the 2.9eV peak we propose two possible explanations: Direct ionization to vibrationally excited ground states of the ion, or resonant transition to a vibrationally excited Rydberg state.

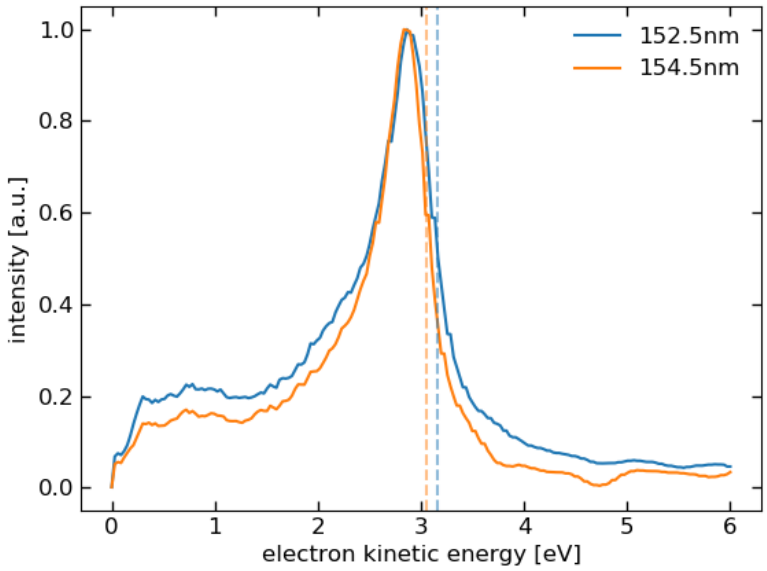

Figure 4.7: Background subtracted 1+1' 1D photoelectron spectrum of OCS. The dashed orange and blue lines indicate the 1+1' cut off energy.

For direct ionization to the vibrationless ground state of the ion, the expected photoelectron kinetic energy would be 3.05eV (3.16eV), which is both higher than observed and, critically, not independent of VUV wavelength. However, if the vibrational quanta of the excited state are preserved (i.e. Franck-Condon diagonality) in the photoionization transition (i.e. (1,1,0) ← (1,1,0) and (2,1,0) ← (2,1,0)), the photoelectron kinetic energy would be 2.91eV (2.92eV).

Figure 4.8 shows the anisotropy parameters (a) β_2, (b) β_4 and (c) β_6 for the non-background subtracted photoelectron spectra integrated over all time delays. They will be used here to investigate the 1+1' anisotropies, as the background subtracted fits were too noisy. The transparent traces are the corresponding photoelectron spectra, used as a reference only. In the 2.9eV energy range, there is a β_4 contribution of -0.2, a supression of the β_2 contribution, and no significant β_6 contribution. This suggests that the outgoing photoelectrons have d wave character, as s and p waves can not contribute to β_4. While direct ionization to the X $^2\Pi$ state allows for both p and d waves, it is interesting that a direct

ionization process here would contribute to β_4 only, whereas the direct ionization with two photons of VUV contributed to β_2 only. If direct ionization is the mechanism, it contradicts the previous angular momentum transfer argument that lower angular momentum will have a higher probability. However, this is not conclusive evidence that rules out direct ionization. Calculation of the Franck-Condon factors involved would help provide more insight.

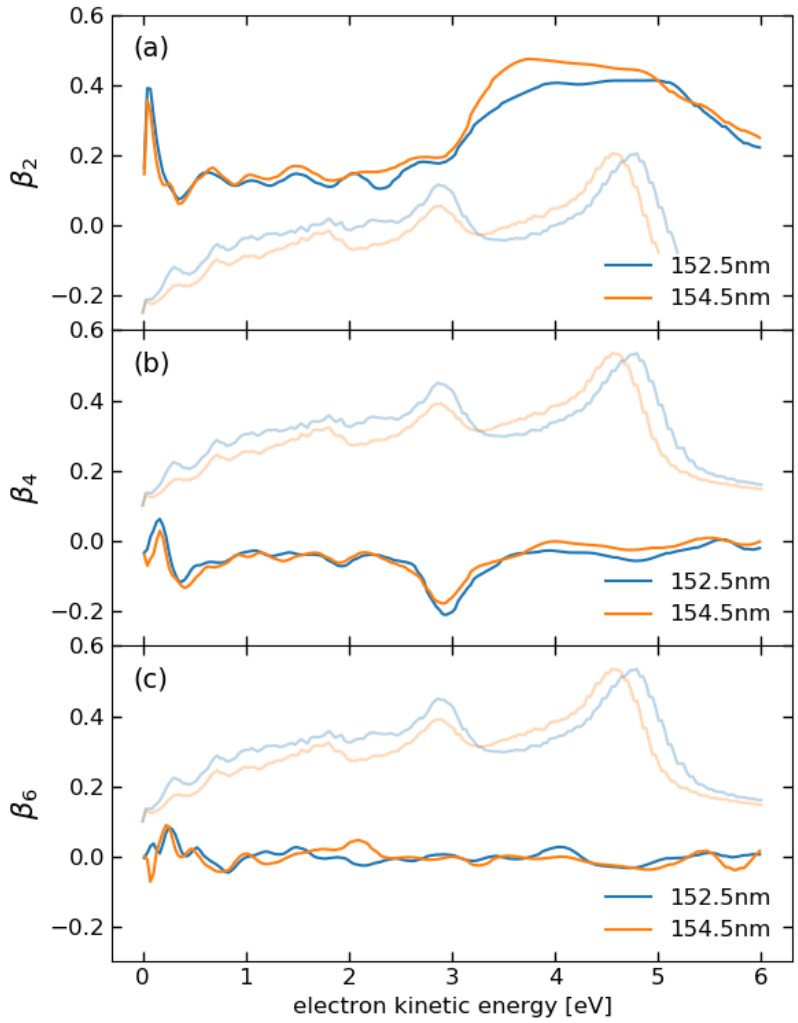

Figure 4.8: Anisotropy parameters (a) β_2, (b) β_4 and (c) β_6 for the non-background subtracted photoelectron spectra integrated over all time delays for both VUV wavelengths. The transparent traces are the corresponding photoelectron spectra for reference only.

The other possible mechanism here is resonant excitation of a superexcited Rydberg state. As discussed in the electronic structure section, there are two Rydberg states converging on the B state of the ion which are close to the total pump-probe photon energy of 14.24eV (14.34eV). The series V, n=4 nsσ state at 14.4eV is possibly accessible by the 14.34eV pump-

probe pair within its bandwidth, but the lower energy pump-pair does not reach this energy. In addition, this Rydberg series has s character which does not support the β_4 observation. We therefore exclude this mechanism. The series IV, n=3 ndσ state covers the energy range of 13.9-14eV, which becomes accessible to both pump-probe transitions only if the final Rydberg state was vibrationally excited. The symmetric stretch and bend of the B state core have fundamental constants of $\nu_1 = 0.092$eV and $\nu_2 = 0.064$eV, respectively[92]. Inclusion of various combinations of these modes allows both pump-probe transitions to access this state. Based on energetics alone, the most probable transitions are (3,1,0) $\leftarrow$ (1,1,0) or (1,4,0) $\leftarrow$ (1,1,0) at 14.24eV and (4,1,0) $\leftarrow$ (2,1,0) or (2,4,0) $\leftarrow$ (2,1,0) at 14.34eV. Calculation of the Franck-Condon factors would provide more insight. What happens during the autoionization process of the superexcited Rydberg state is unknown, but for this mechanism it must produce 2.9eV photoelectrons for both pump wavelengths. The observed β_4 and symmetry arguments are supported by the d character of this state.

The observed shoulder could arise from an unresolved vibrational progression in the direct ionization case. In the resonant Rydberg state picture, either an unresolved vibrational progression or radiationless transitions followed by autoionization could perhaps also account for the shoulder. This will be discussed in the time resolved section, below. There are also two small peaks at 0.3eV and 0.7eV. These could be due to the same sulfur autoionization processes mentioned in the VUV background analysis. As the energy of formation of S^+ (^4S_o) + CO(X $^1\Sigma^+$) is 13.54eV, sulfur superexcited states up to 0.72eV (0.82eV) are accessible with the VUV + 200nm photons. Alternatively, they could arise from imperfect background subtraction of the two-photon VUV signal.

4.7.3 Time-resolved Experiments

In this section the 1+1' time resolved 2D photoelectron spectra will be analysed. The fitting procedure and uncertainty analysis will be outlined followed by a discussion of the excited

state dynamics of the $^1\Sigma^+$ excited state of OCS.

Fitting procedure

In TRPES experiments, it is typical to fit the 2D photoelectron spectra using a global fitting routine[102,103]. Global fitting assumes that the 2D TRPES data may be represented by a set of time-independent photoelectron spectra, each having a specific time dependence according to a fit function chosen based on a hypothesized kinetic rate equation model. For example, the fit function may be a mono-, bi-, or tri-exponential decay, in a sequential or parallel mechanism, depending on how many and what kind of competing decay pathways are thought to exist. The fit function is convoluted with a gaussian instrument response function (the measured cross-correlation) in order to account for the finite laser pulse durations. In the case of OCS, a mono exponential decay gave the best fit results. The form of the fit function was

$$S(t) = A \exp\left(\frac{1}{2}(\nu\sigma)^2 - \nu(t - t_0)\right) \operatorname{erfc}\left(\frac{-(t - t_0) + \nu\sigma^2}{\sqrt{2}\sigma}\right),$$

where A is the amplitude, ν is the inverse lifetime, σ is the standard deviation of the instrument response function, t_0 is the time-zero offset, and erfc is the complimentary error function. The time-zero offset, instrument response function and the decay constant were fit simultaneously across all kinetic energies and time delays. Figure 4.9 shows the residuals for a global fit of the 152.5nm dataset, with a clear crossing pattern visible, indicating a poor fit. Noting that the residuals were defined as the fit subtracted from the experimental data, the crossing pattern indicates that the onset of photoelectron signal was delayed at lower kinetic energies. The next attempt was to use a global fit with a floating time-zero offset for each kinetic energy slice. This was also unsuccessful, as seen by the large magnitude of the residuals, shown in Fig. 4.10. This indicated that both the time-zero offset and the decay constant were not shared globally across the photoelectron spectrum. The final method used was to fit each kinetic energy slice independently.

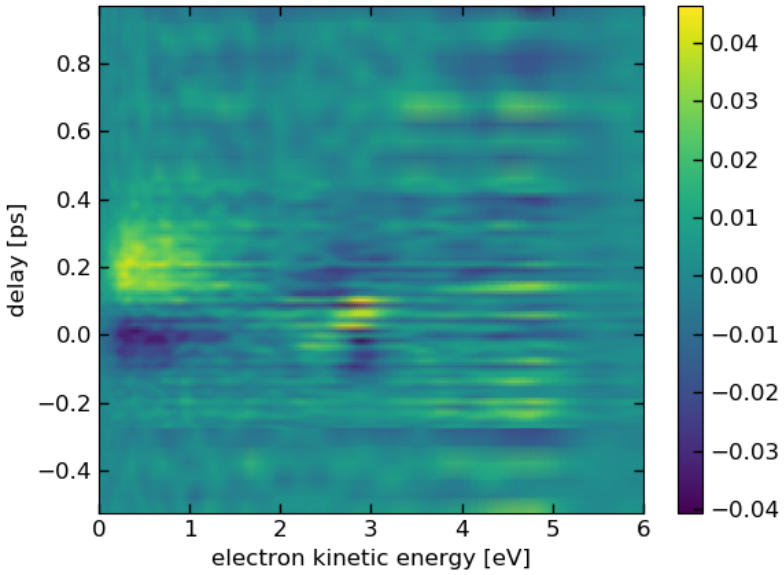

Figure 4.9: Residuals for a global fit with a common lifetime and time-zero offset. Note the clear pattern at low kinetic energies, indicating a poor fit.

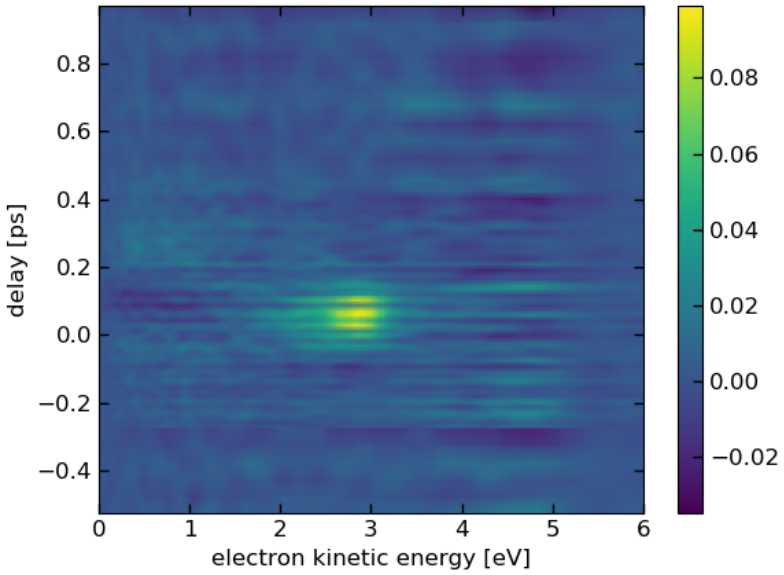

Figure 4.10: Residuals for a global fit with a common lifetime and a floating time-zero offset. Note the large peak at 2.9eV (roughly 9%), which indicates a poor fit.

A sensitivity analysis based on a χ^2 surface search algorithm was used to determine

the parameter uncertainties. First, a minimum χ^2 value was calculated to find the best fit parameters. A threshold χ^2 value for a 95% confidence interval was then calculated using the MATLAB built-in finv function. Each fit parameter was then individually incremented (e.g. in the positive direction) from its fitted value in one direction, held constant, and the fit routine was run again. This process was repeated until the χ^2 value converged to within 10^{-4} of the 95% threshold. Once convergence was reached, the difference between the threshold value of the parameter and its best fit value determined the width of the uncertainty in that (positive) direction. Both positive and negative directions of each parameter were searched in order to determine all confidence interval parameter uncertainties. This method was used over the conventional second derivative approximation of fit uncertainties as it is more accurate and is helpful in determining the degree of coupling between fit parameters. The increased accuracy arises from directly searching the χ^2 hypersurface near the minimum, rather than approximating the surface as a parabola and then using the second derivative test. Figure 4.11 shows an example 2D cut of the χ^2 hypersurface along the (i) time-zero offset parameter and (ii) lifetime fit parameter axes for the 3eV slice of the 152.5nm dataset. The dashed black line is the calculated χ^2 threshold and the red crosses indicate the calculated uncertainties. Coupling between these parameters is deduced by the major axis of the ellipse-like shape of the threshold contour. A perfectly horizontal or vertical major axis would indicate no coupling between parameters, as well as the smallest uncertainties. As the major axis becomes more sloped the coupling increases, along with the uncertainties. Here we see a negative slope indicating an inverse coupling between the time-zero offset and the lifetime fit parameters.

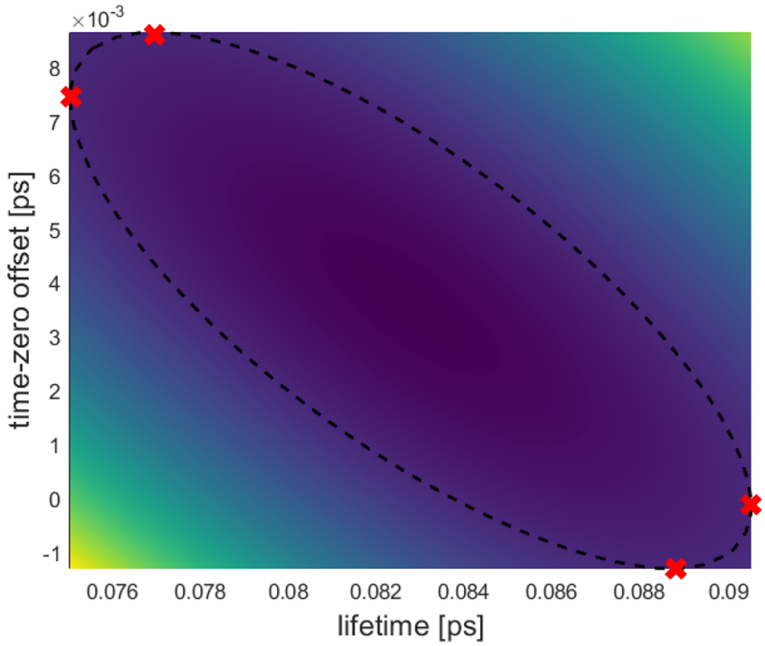

Figure 4.11: Sample χ^2 surface used to calculate the fit uncertainties for the 152.5nm dataset at 3eV. The black dashed line indicates the threshold χ^2 for a 95% confidence interval. The red crosses indicate the actual fit uncertainties.

The background subtracted, time-resolved pump-probe (a) 2D PES, (b) fit and (c) residuals for both 152.5nm (left) and 154.5nm (right) VUV wavelengths can be seen in Fig. 4.12. These are the time-resolved versions of Fig. 4.7. There is an intense peak at 2.9eV in both cases, as well as a shoulder extending to 0.3eV as expected.

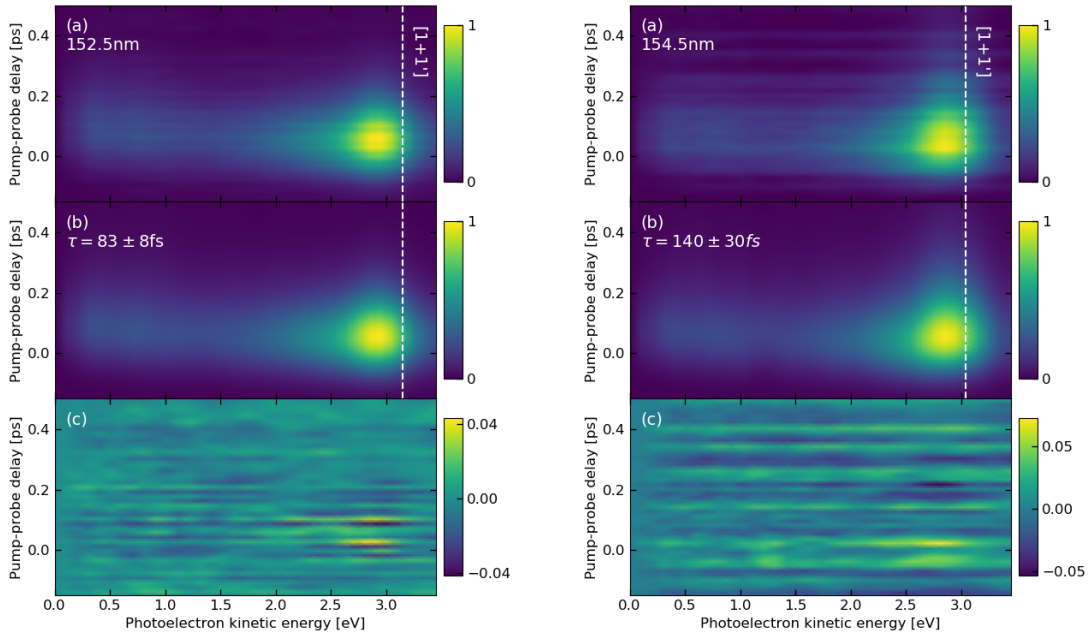

Figure 4.12: Time resolved photoelectron spectra (a) data, (b) fits and (c) residuals for the 152.5nm (left) and 154.5nm (right) VUV wavelengths. The 1+1' energy cut-offs are indicated by the white dashed lines. The lifetimes are written in panel b.

Figure 4.13 show the fit parameters (a) time zero offset t_0 and (b) lifetime τ for both VUV wavelengths, with the uncertainties represented by the shaded areas. The lifetimes were measured to be $\tau = 140 \pm 30$fs for the (1,1,0) state at 154.5nm and $\tau = 83 \pm 8$fs for the (2,1,0) state at 152.5nm, measured at the maxima of the peaks at 2.9eV (gray dashed line). Yamanouchi et al. reported lifetimes of 133fs and 44fs, respectively, based on linewidths from photofragment S(^{1}S) action spectra[87]. A linewidth, however, is not a direct measurement of the lifetime and represents only a lower bound. Our direct measurement of the lifetimes are therefore not inconsistent with previous work. It is interesting to note that the lifetimes converge to roughly 120fs in the low energy shoulder of the spectrum (0-1.5eV). This may be an indication of a different mechanism in the low photoelectron energy range.

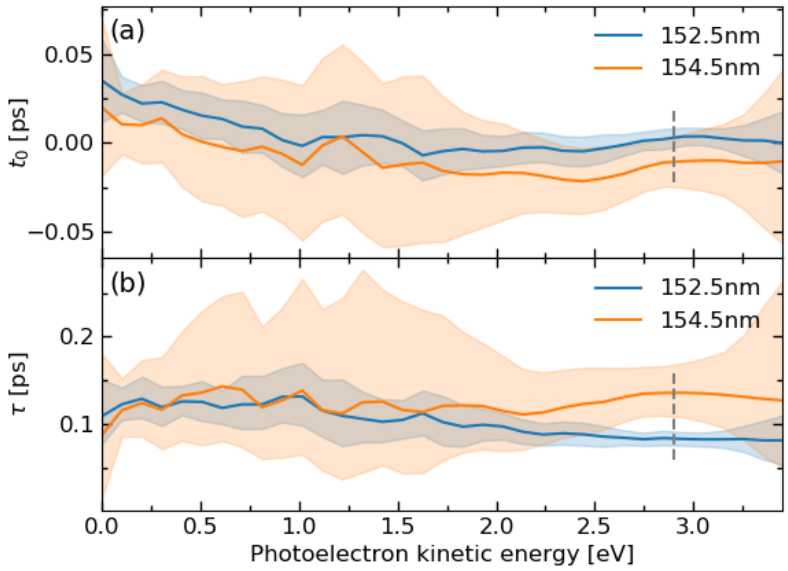

Figure 4.13: Fit parameters (a) time-zero offset t_0 and (b) lifetime tau for both VUV wavelengths. The lifetimes were found to be 83±8fs at 152.5nm and 140±30fs at 154.5nm, measured at the maxima of the peaks at 2.9eV (gray dashed lines). Uncertainties are represented by the shaded areas.

Looking at the time-zero offset (panel a), there is a clear sloping delay at lower energies. This is further evidence of a different mechanism. Note that it is the combination of this effect, along with the changing lifetimes as a function of energy that necessitated a non-global fit. There is also a 13fs offset between the two wavelengths. For a non-global fit, this offset is arbitrary and is likely due to an imperfect time-zero calibration.

To explain the origins of the low electron kinetic energy shoulder and the features described above, it is helpful to first describe which explanations can be ruled out. In the experiment, the pump laser excited the OCS molecule, subsequent dynamics evolved and then the probe laser ionized the molecule, projecting the excited state dynamics onto the final state. Dynamics occuring in the final state following the probe laser transition, including neutral predissociation, intramolecular radiationless transitions, molecular autoionization, atomic sulfur autoionization, etc. are not themselves probed as a function of time in this ex-

periment. The observed time-dependent features can only originate from dynamical evolution on the $^1\Sigma^+$ excited state potential and its time-dependent projection onto final states.

The following is a suggested explanation of the phenomenological observation that the delay of time-zero offset increases towards low electron kinetic energy. Low kinetic energy photoelectrons mean that the cation is left in a higher final vibrationally excited state. Due to Franck-Condon factors, higher lying vibrational final states of the cation will be populated by transitions from to neutral excited states undergoing larger amplitude motions. This means that as the nuclear geometry of the $^1\Sigma^+$ state evolves, so will the Franck-Condon overlap with the vibrational states. Thus, the transition probability to those states will be time dependent, with transitions to higher lying vibrational states (i.e. slower photoelectrons) increasing with time delay. This due to the distorted geometries that gain probability as the $^1\Sigma^+$ excited state geometry evolves. However, we cannot definitively explain this phenomenological observation without theoretical support. Theoretical quantum dynamics simulations of wavepacket dynamics in the $^1\Sigma^+$ state of OCS are currently underway, led by Dr. Michael S. Schuurman of the NRC theory group. Combined with the experimental observations from this work, the results will be presented in a future publication.

4.8 Conclusion

OCS is a linear triatomic molecule with relevance to atmospheric chemistry due to its absorption cross section in the UV/VUV. For our purposes, OCS will be a useful benchmark for the new spectrometer outlined in chapter VMI. The evidence of OCS and sulfur autoionization outlined in this chapter will be definitively proven by the photoelectron photoion covariance capabilities of the new instrument. OCS will also be useful as a benchmark molecule in ultrafast X-ray spectroscopy. As OCS is comprised of three distinct atoms, probing the atom-specific charge density variations will provide insight into the benefits of this method over conventional valence shell spectroscopy described in this chapter.

The $^1\Sigma^+$ excited state dynamics of OCS were directly observed using time-resolved velocity map imaging (VMI) photoelectron spectroscopy. Two vibrational transitions were investigated using a tunable femtosecond VUV source: the (1,1,0) state at 8.025eV and the (2,1,0) state at 8.130eV. In the 2×VUV background spectra we found evidence for direct ionization based on the different peak positions for each wavelength and the β_2 contribution to the anisotropy. Sulfur autoionization was also observed, evidenced by the independence of peak position with respect to pump wavelength as well as previous work by Hikosaka et al. In the time dependent photoelectron spectra, we find evidence for transition to vibrationally active superexcited Rydberg states. The time-dependent spectra were fit with a phenomenological mono-exponential decay function to determine the lifetimes of the $^1\Sigma^+$ vibrationally excited states, which were found to be $\tau = 140 \pm 30$fs for the (1,1,0) state at 154.5nm and $\tau = 83 \pm 8$fs for the (2,1,0) state at 152.5nm.

Chapter 5

Conclusion

The design and simulations of a new angle-resolved PEPICO spectrometer were presented. It was compared to several other designs on the basis of photoelectron kinetic energy resolution, mass spectrometry resolution, and photoelectron time spread resolution, the latter being an important factor for 3D VMI. A new advance in electrode potentials was presented which doubles the electron arrival time spread while maintaining VMI conditions with minimal degradation in energy resolution. The spectrometer is currently awaiting machine shop parts to be assembled.

The ultrafast tunable VUV light source and VMI spectrometer, located at the NRC on 100 Sussex Drive, were presented to provide the technical background required to understand in detail the OCS VMI experiments. Issues of stability were discussed, noting that maintaining a stable ultrafast amplified laser system of the course of many hours is a significant challenge and requires the best in lab stability with respect to temperature, vibration, and humidity. Data preprocessing and VMI spectrometer calibration were also discussed.

The ultrafast tunable VUV source was used for a TRPES study of the $^1\Sigma^+$ excited state dynamics of OCS. Two VUV-exited vibrational transitions ((1,1,0) and (2,1,0)) were investigated and found to have lifetimes of 140±30fs and 82±8fs, respectively. Theoretical calculations, by Dr. Michael S. Schuurman (NRC theory group), of the excited state dynamics are currently underway but were not completed at the time of writing this thesis. These theoretical results will be combined with the experimental results presented here in a future

publication.

In TRPES experiments, it is important to understand the projection of the excited state by the probe pulse onto the molecular ionization continuum. In the case of OCS, there is a rich structure of superexcited Rydberg states superimposed on a flat photoelectron continuum. From the photoelectron spectra and anisotropy parameter fits, we deduced three different ionization mechanisms. Direct ionization to the continuum was inferred by the pump wavelength dependence of the highest photoelectron kinetic energy peaks as well as the β_2 anisotropy parameter contributions. Projection to superexcited Rydberg states followed by molecular autoionization was observed, as evidenced by the wavelength independence of the photoelectron kinetic energy peaks and the β_4 anisotropy parameter contributions. Projection to superexcited Rydberg states, followed by dissociation of the superexcited neutral molecule into neutral CO and superexcited S* photoproducts with subsequent S* autoionization was deduced via the wavelength independence of the peaks, the photoelectron kinetic energy range they occupied and comparison to previous work by Hikosaka and coworkers[97].

This valence shell study of OCS will be used as a benchmark for the new VMI spectrometer, taking full advantage of the covariance capabilities to definitively determine our assignments of direct ionization, molecular autoionization and sulfur autoionization. It will also be used as a benchmark to test the validity of the claim that ultrafast X-ray spectroscopy provides unprecedented detail by measuring atom-specific core shell charge density variations as opposed to their valence shell counterparts.

Appendix A

3D Simulations

3D simulations were performed by sampling thousands of electron initial conditions to generate 2D VMI images. Each electron was given from a distribution:

- An initial position in the interaction region
- An initial kinetic energy
- An initial angular direction

The interaction region was sampled as described in section 2.3.3 and is shown in Fig. 2.3. Kinetic energies were chosen to be exact, but a normal distribution is easily added if simulation of a laser bandwidth is of interest. Electron angular distributions were sampled from a spherical harmonic probability distribution function (PDF). The derivation is as follows: using the spherical harmonic Y_1^0 as an example, the PDF is

$$\mathrm{PDF}(\theta, \phi) = |Y_1^0(\theta, \phi)|^2 \sin\theta = \frac{3}{4\pi} \cos^2\theta \sin\theta,$$

adding in the $\sin\theta$ from the solid angle area element $d\Omega = \sin\theta d\theta d\phi$. Here θ is defined as the polar angle and ϕ is the azimuthal angle. Marginalizing the joint distribution to separate into individual PDFs for θ and ϕ, we obtain

$$\mathrm{PDF}(\theta) = \int_0^{2\pi} \frac{3}{4\pi} \cos^2\theta \sin\theta d\phi = \frac{3}{2} \sin\theta \cos^2\theta,$$

$$\mathrm{PDF}(\phi) = \int_0^{\pi} \frac{3}{4\pi} \cos^2\theta \sin\theta d\theta = \frac{1}{2\pi}.$$

The idea now is to find the cumulative distribution function (CDF) for each angle. The CDF is a monotonically increasing function from [0,π] $\rightarrow$ [0,1] for theta and [0,2π] $\rightarrow$ [0,1] for phi, which means it can be inverted. The inverse CDF allows us to randomly sample a uniform distribution from [0,1] that will output an angle that follows the original probability distribution. The CDFs are

$$\mathrm{CDF}(\theta) = \int_0^{\theta} \frac{3}{2} \sin\theta' \cos^2\theta' d\theta' = \frac{1}{2}(1 - \cos^3\theta),$$

$$\mathrm{CDF}(\phi) = \int_0^{\phi} \frac{1}{2\pi} d\phi' = \frac{\phi}{2\pi},$$

and their inversions are

$$\theta = \cos^{-1}[(1-2u)^{1/3}],$$

$$\phi = 2\pi v,$$

where u, v are randomly sampled numbers on the interval [0,1]. In principle this will work for any spherical harmonic if simulation of more complex angular distributions was of interest. Note that the angles theta and phi here are not the same as the angles defined in section axes. The uniform spherical distribution is parameterized by the equations

$$\theta = \cos^{-1}(1 - 2u),$$

$$\phi = 2\pi v.$$

Appendix B

Simulated VMI Voltages

B.1 3 plate design

Figure B.1: Schematic of the 3 plate design with numbered electrodes in reference to the table below.

Table B.1: 3 plate electron VMI voltage settings.

Name	Number	Voltage [V]
Repeller	1	-462.00
Extractor	2	-332.20
Ground	3	0.00

B.2 NRC design

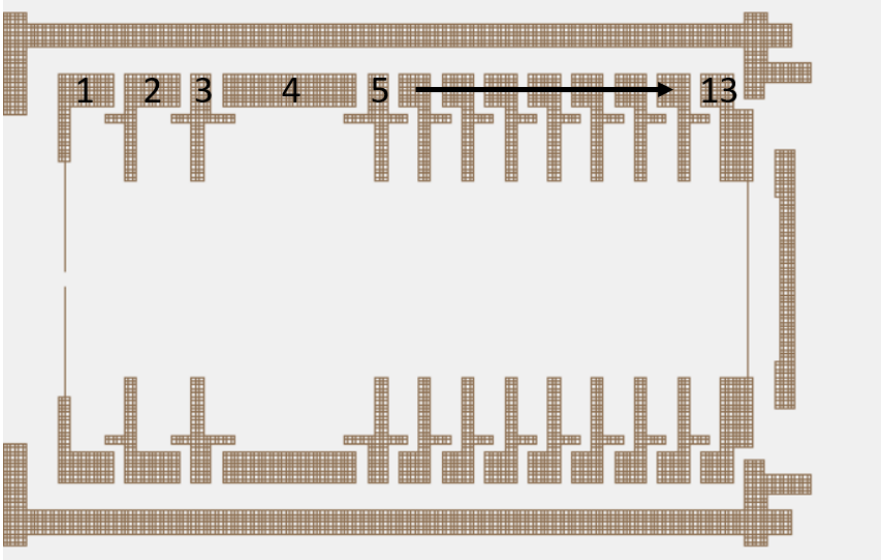

Figure B.2: Schematic of the NRC design with numbered electrodes in reference to the tables below.

B.2.1 Electron VMI

Table B.2: NRC electron VMI voltage settings.

Name	Number	Voltage [V]
Repeller grid	1	-516.66
Repeller 1	2	-558.08
Repeller 2	3	-558.08
Light port	4	-515.57
Extractor	5	-474.15
—	6	-414.96
—	7	-355.67
—	8	-296.37
—	9	-237.08
—	10	-177.89
—	11	-118.59
—	12	-59.30
Ground grid	13	0.00

B.2.2 Ion mass spectrometry

Table B.3: NRC mass spectrometry parallel molecular beam voltage settings.

Name	Number	Potential [V]
Repeller grid	1	4250.00
Repeller 1	2	4300.00
Repeller 2	3	4300.00
Light port	4	2437.50
Extractor	5	2166.50
—	6	1895.50
—	7	1624.75
—	8	1354.00
—	9	1083.25
—	10	812.25
—	11	541.50
—	12	270.75
Ground grid	13	0.00

Table B.4: NRC mass spectrometry perpendicular molecular beam voltage settings.

Name	Number	Potential [V]
Repeller grid	1	4250.00
Repeller 1	2	4300.00
Repeller 2	3	4300.00
Light port	4	3368.75
Extractor	5	2437.50
—	6	2132.75
—	7	1828.00
—	8	1523.25
—	9	1218.75
—	10	914.00
—	11	609.25
—	12	304.50
Ground grid	13	0.00

B.3 20 lens design

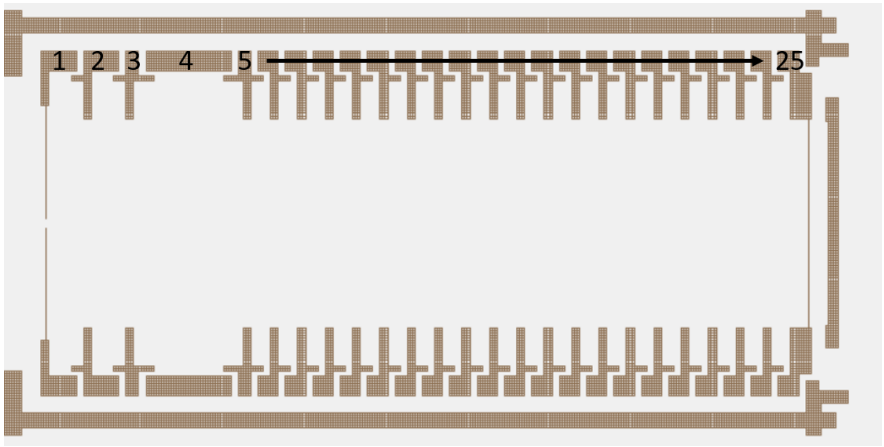

Figure B.3: Schematic of the 20 lens design with numbered electrodes in reference to the tables below.

B.3.1 Electron VMI

Table B.5: 20 lens electron VMI voltage settings.

Name	Number	Potential [V]
Repeller grid	1	-662.39
Repeller 1	2	-697.15
Repeller 2	3	-697.15
Light port	4	-648.64
Extractor	5	-600.12
—	6	-570.14
—	7	-540.11
—	8	-510.12
—	9	-480.10
—	10	-450.11
—	11	-420.09
—	12	-390.10
—	13	-360.07
—	14	-330.09
—	15	-300.06
—	16	-270.07
—	17	-240.09
—	18	-210.06
—	19	-180.04
—	20	-150.05
—	21	-120.06
—	22	-90.04
—	23	-60.05
—	24	-30.03
Ground grid	25	0.00

B.3.2 Ion mass spectrometry

Table B.6: 20 lens mass spectrometry parallel molecular beam voltage settings.

Name	Number	Potential [V]
Repeller grid	1	4275
Repeller 1	2	4300
Repeller 2	3	4300
Light port	4	2500
Extractor	5	1500
—	6	1425
—	7	1350
—	8	1275
—	9	1200
—	10	1125
—	11	1050
—	12	975
—	13	900
—	14	825
—	15	750
—	16	675
—	17	600
—	18	525
—	19	450
—	20	375
—	21	300
—	22	225
—	23	150
—	24	75
Ground grid	25	0

Table B.7: 20 lens mass spectrometry perpendicular molecular beam voltage settings.

Name	Number	Potential [V]
Repeller grid	1	4275.00
Repeller 1	2	4300.00
Repeller 2	3	4300.00
Light port	4	3368.75
Extractor	5	2437.50
—	6	2315.50
—	7	2193.75
—	8	2071.75
—	9	1950.00
—	10	1828.00
—	11	1706.25
—	12	1584.25
—	13	1462.50
—	14	1340.50
—	15	1218.75
—	16	1096.75
—	17	975.00
—	18	853.00
—	19	731.25
—	20	609.25
—	21	487.50
—	22	365.50
—	23	243.75
—	24	121.75
Ground grid	25	0.00

B.4 PEPICO design

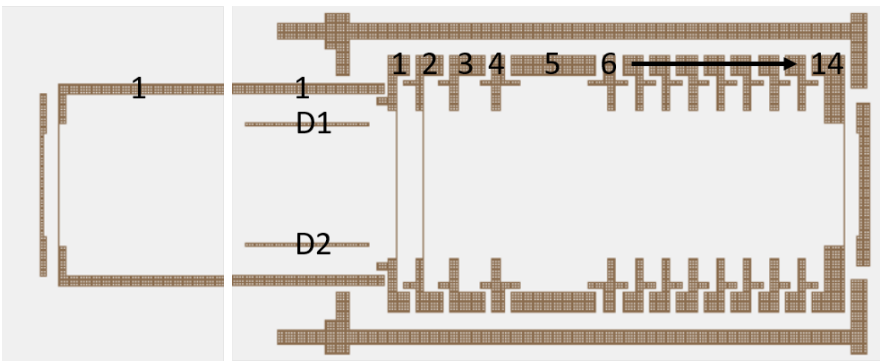

Figure B.4: Schematic of the PEPICO design with numbered electrodes in reference to the tables below.

B.4.1 Electron VMI

Table B.8: PEPICO electron VMI voltage settings.

Name	Number	Potential [V]
WM grid/ion tube	1	—
Repeller grid	2	-521.40
Repeller 1	3	-563.20
Repeller 2	4	-563.20
Light port	5	-521.40
Extractor	6	-478.50
—	7	-418.69
—	8	-358.88
—	9	-299.06
—	10	-239.25
—	11	-179.44
—	12	-119.63
—	13	-59.81
Ground grid	14	0.00

Table B.9: PEPICO electron VMI with quadratic stepped potentials voltage settings.

Name	Number	Potential [V]
WM grid/ion tube	1	—
Repeller grid	2	-462.30
Repeller 1	3	-507.25
Repeller 2	4	-507.25
Light port	5	-481.15
Extractor	6	-452.15
—	7	-437.67
—	8	-411.17
—	9	-372.67
—	10	-322.16
—	11	-259.63
—	12	-185.10
—	13	-98.55
Ground grid	14	0.00

B.4.2 Ion mass spectrometry

Table B.10: PEPICO mass spectrometry voltage settings.

Name	Number	Potential [V]
Deflector Plate 1	D1	-1889.36
Deflector Plate 2	D2	-1959.36
WM grid/ion tube	1	-1924.36
Repeller grid	2	-1330.00
Repeller 1	3	-1200.00
Repeller 2	4	-1060.00
Light port	5	-1160.00
Extractor	6	-980.00
—	7	-857.50
—	8	-735.00
—	9	-612.50
—	10	-490.00
—	11	-367.50
—	12	-245.00
—	13	-122.50
Ground grid	14	0.00

B.4.3 Covariance

Table B.11: PEPICO covariance voltage settings.

Name	Number	Potential [V]
Deflector Plate 1	D1	-1890.00
Deflector Plate 2	D2	-1960.00
WM grid/ion tube	1	-1925.00
Repeller grid	2	-665.00
Repeller 1	3	-600.00
Repeller 2	4	-530.00
Light port	5	-510.00
Extractor	6	-490.00
—	7	-428.75
—	8	-367.50
—	9	-306.25
—	10	-245.00
—	11	-183.75
—	12	-122.50
—	13	-61.25
Ground grid	14	0.00

Appendix C

OPA

C.1 OPA operation

An optical parametric amplifier is a device that leverages parametric amplification through difference frequency mixing (DFM) to generate broadly tuneable ultrafast pulses, typically in the infrared spectral region. There are two main steps to optical parametric amplification: white light seed generation and amplification. In the first step, white light is generated via a third order nonlinearity in a $\chi^{(3)}$ material. The white light is a broad spectrum that contains the desired wavelength but has low spectral power and thus needs to be amplified. The next step consists of one or more stages of parametric amplification chained together in series. DFM uses energy from the pump to amplify the seed as well as generate a complimentary wavelength that is exactly the difference in energy between the pump and the seed. The amplified seed is called the signal and the complimentary wavelength is called the idler. The wavelength that is amplified from the white light is determined by the phase matching angle of the crystal used for DFM, as well as temporal gating of the seed by the pump.

As stated in the experimental setup section the OPA used was the Light Conversion TOPAS-C which has a tuning range of 1160-1600nm for the signal and 1600-2600nm for the idler. As stated in the experimental section, wavelengths of 980nm and 1070nm were required for VUV generation. Therefore, the idler was used at 1960nm and 2140nm and frequency doubled at the output. In this section, the operation of the OPA will be discussed, including

the setup for wavelength tuning as well as pitfalls to avoid.

C.2 OPA under the hood

The incoming pump is split into three paths, listed in ascending order of the fraction of input intensity: The first is for white light generation, the second is the pump pulse for the first stage of amplification, while the third is the pump for the final stage of amplification. Note that the higher intensity split is always reflected to minimize nonlinear and dispersion effects in the beam splitter. This will become important later when pulse compression is discussed.

The 800nm for the white light arm is passed through a motorized delay line (D1) and then focussed into a sapphire disk to generate the white light. It then passes through a zinc selenide rod to chirp and stretch the pulse. This allows for more selectivity in which colour is amplified by changing the timing overlap (using D1) of the white light with the pump in the first amplification stage.

The white light then recombines with the path 2 pump pulse non-collinearly in the first amplification stage BBO crystal. The crystal is mounted on a motorized rotation stage (C1) for tuning of the phase matching angle. It is also a thin crystal which promotes broadband amplification but with much less gain than a thick crystal (gain is proportional to the thickness squared). The non-collinear geometry is used to block the pump and the idler after the crystal.

The signal from the first stage is then passed through another delay line (D2) and recombined collinearly with the path 3 pump in a thick BBO crystal mounted on another motorized rotation stage (C2). The leftover pump is then filtered out and the signal and idler exit the OPA with crossed polarizations.

C.3 Turning on the OPA

The following is a set of instructions for properly turning on the OPA and avoiding damage to the crystals inside:

1. The laser was warmed up for at least an hour.

2. The OPA shutter was checked to be closed and a physical beam block was placed in front of the OPA input. The shutter is not meant to withstand high power beams for extended periods of time.

3. The compressor was set to maximize power in the 267nm pump of the VUV generation arm (roughly 180mW in our setup). The focussing optics in the OPA are optimized for this compressor setting. If the compression is set incorrectly, the white light generation and first stage pump pulses in the OPA can be compressed by material dispersion, increasing their instantaneous power which can cause damage in the crystals.

4. The HEPA filter above the OPA was turned off to reduce air currents. This was useful to accurately assess stable white light generation.

5. The OPA cover was removed. Care was taken not to speak or track dirt into the box as the optics are difficult to clean and expensive to replace. A piece of tape was placed on the limit switch to defeat the safety interlock.

6. A beam block was placed in the path of the second stage pump. A business card was placed to simultaneously block the first stage pump and observe the white light generation.

7. The beam block in front of the OPA input was removed and the shutter was opened.

8. The white light was observed on the business card. It should be a rainbow-like pattern extending radially outward. There should be minimal flickering and no visible fringes.

9. If flickering or fringes were observed, the shutter was closed, and the compression was adjusted slightly. The shutter was reopened, and the white light generation was checked again. If the problem persisted, it may be caused by poor alignment of the input beam into the OPA (For alignment procedures refer to the TOPAS-C manual).

10. When the white light appeared stable, the shutter was closed. The paper card and beam block were removed from inside the OPA. The cover was then replaced.

11. A power meter was placed after the dielectric separator mirrors. The shutter was opened, and the output power was measured. Typical pulse energies measured were 18mW at 980nm and 12mW at 1070nm. Normal variation was roughly ±1mW, fluctuating on the few-second time scale.

C.4 Tuning the OPA

Figure C.1 shows the typical efficiency tuning curve of the TOPAS-C OPA. Figure C.2 shows the VUV tuning curve for a 267nm pump. The VUV wavelength is calculated with basic energy conservation using the formula

$$\lambda_{VUV} = \frac{1}{\left(\frac{2}{267nm} - \frac{1}{\lambda_{OPA}}\right)}.$$

From Fig. C.1 we see that the signal does not tune to the wavelength region required (980-1070 nm). Therefore, the idler was tuned to half the frequency and doubled in BBO outside the OPA.

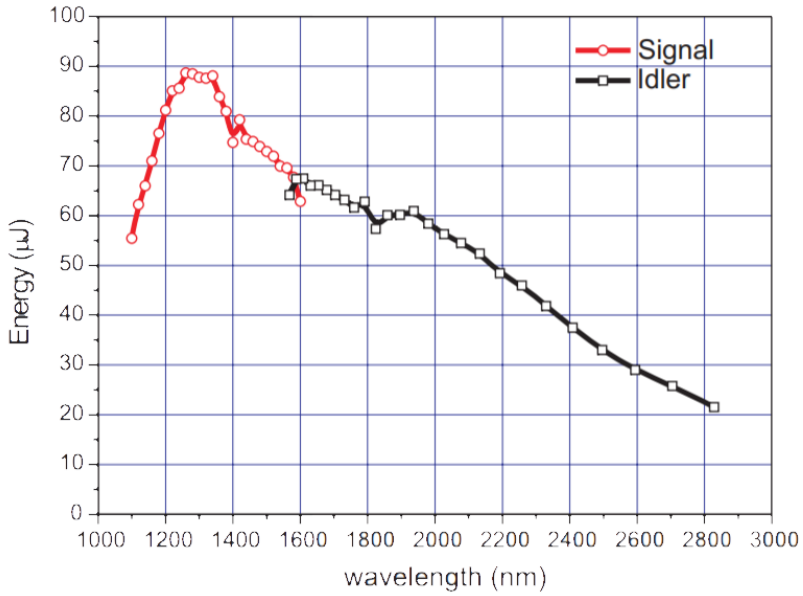

Figure C.1: Typical output performance of TOPAS-C pumped with 0.5mJ, 792nm, 135fs pulses (Quantronix-4800). Stability of pump energy 0.5% rms. While not a direct comparison to our setup, this plot provides a reference for conversion efficiency. Adapted from Light Conversion TOPAS-C manual.

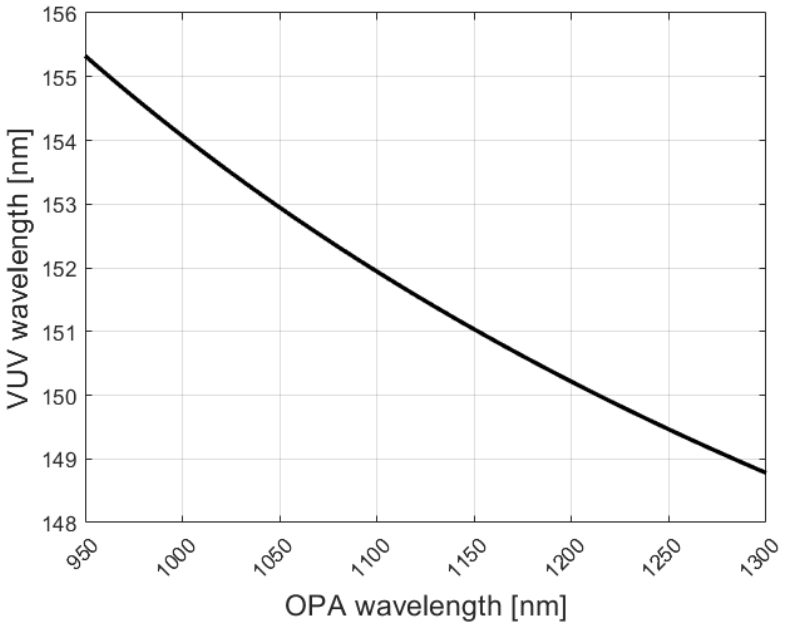

Figure C.2: VUV wavelength dependence on OPA wavelength, based on energy conservation. The pump wavelength was fixed at 267nm.

Depending on the desired change in wavelength, tuning the OPA can be either a simple task or a massive headache. Since the OPA in our setup does not have a properly calibrated tuning curve, changing the wavelength by large amounts can be challenging. I will outline a fast method for small increments that requires no interruptions to the output beam path and a slower, more robust method that has a higher chance of losing spatial overlap of the OPA with the 267nm in the VUV box.

The fast method is to place a spectrometer in the beam path after the wavelength separator. In this way it is used as both a spectrometer and power meter. This is quick and simple for small adjustments, provided the spectrometer is properly calibrated and has a flat spectral response across the tuning range. In our case we used an Ocean Optics HR4000 spectrometer which uses a silicon based detector. Silicon has a large drop in sensitivity leading up to 1100nm. Using the spectrometer on a sloping sensitivity curve will artificially blueshift the observed spectrum as well as substantially decrease the observed flux when tuning towards longer wavelengths. This method worked well for fine tuning around 980nm but was much less reliable to tune to 1070nm.

The more robust method involves measuring the frequency doubled signal pulse with a power meter and spectrometer simultaneously. Figure C.3 shows a picture of the setup. The BBO crystal that frequency doubles the idler was rotated by 90 degrees for type I phase matching of the signal instead. The wavelength separator was removed as table space was limited. In theory this is not necessary and would help minimize the chances of misaligning the VUV generation interaction region. The power meter was placed after the BBO to measure the signal, its frequency doubled component and the idler. The front face reflection from the power meter was directed into the spectrometer for simultaneous measurement. This scheme solves two problems: First, the frequency doubled signal is in the visible region where silicon is a better detector. This eliminates the sensitivity issue. Second, the total output power of the signal and idler is measured as opposed to just the frequency doubled idler. This

provides a more reliable measure of the efficiency for comparison to the expected efficiencies. Due to it being a parametric process, simple energy conservation is used to calculate the idler wavelength from the frequency doubled signal. The idler frequency is calculated with the equation $\omega_{idler} = \omega_{pump} - \omega_{2signal}/2$.

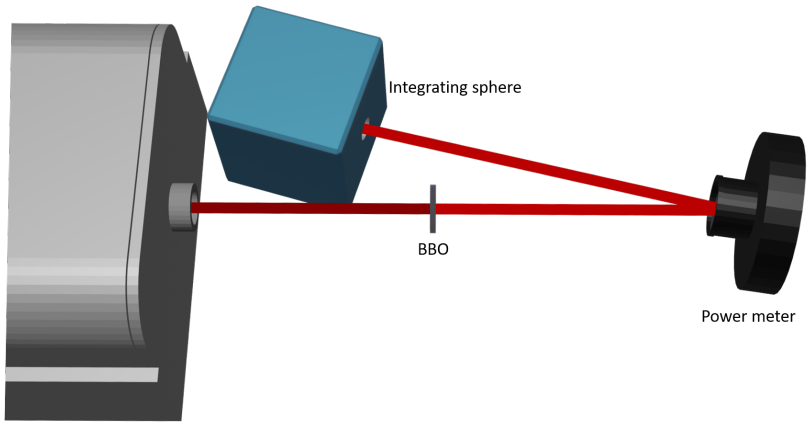

Figure C.3: Setup for tuning the OPA. The BBO crystal is set up to frequency double the signal. The power meter measures the power of the signal, idler and frequency doubled signal. The integrating sphere, connected to an ocean optics (model) spectrometer, measures the spectrum of the frequency double signal using the front-face reflection from the power meter.

The basic tuning procedure in both methods is the same:

1. The phase matching angle C2 was adjusted so that the spectrum shifted in the desired direction. C2 is the most wavelength selective as thick crystals have more restrictive phase matching conditions.

2. The phase matching angle of the BBO crystal outside the OPA was adjusted until the spectrum was symmetric. Looking for the asymmetry of the tails of the spectrum was helpful.

3. D2 was adjusted to recover or increase the measured power. The pulse from the first stage of amplification is chirped so adjusting D2 will optimize the timing overlap of the required wavelengths in C2.

4. Finer adjustments were made with C1 and D1. D1 is more wavelength selective than C1 as the chirped white light pulse is gated in time by the pump in the first BBO crystal.

5. Steps 1-4 were iterated over, while saving and writing down all four stepper motor positions at regular intervals. Once the desired wavelength was achieved with comparable efficiencies to Fig. C.3, stepper motor positions were saved and written down again.

6. Once completed, the saved motor positions were used to quickly swap between wavelengths, with the only adjustment being the phase matching angle of the external BBO crystal.

Bibliography

(1) Bixon, M.; Jortner, J. *The Journal of Chemical Physics* **1968**, *48*, 715.

(2) Jortner, J.; Rice, S. A.; Hochstrasser, R. M. *Adv. Photochem.* **1969**, *7*, 149.

(3) Birks, J. B., *Organic Molecular Photophysics*; John Wiley & Sons Inc.: 1973; Vol. 1.

(4) Fong, F. K.; Diestler, D. J.; Freed, K. F.; Kopelman, R.; Wright, J. C., *Radiationless processes in molecules and condensed phases*; Springer: 1976, p 23.

(5) Stock, G.; Domcke, W. *Advances in Chemical Physics* **1997**, *100*, 1.

(6) Worth, G. A.; Cederbaum, L. S. *Annu. Rev. Phys. Chem.* **2004**, *55*, 127.

(7) Klessinger, M.; Michl, J., *Excited states and photochemistry of organic molecules*; VCH: 1994.

(8) Köppel, H.; Domcke, W.; Cederbaum, L. S. *Advances in Chemical Phyiscs* **1984**, *57*, 59.

(9) Schoenlein, R. W.; Peteanu, L. A.; Mathies, R. A.; Shank, C. V. *Science* **1991**, *254*, 412–415.

(10) Jortner, J.; Ratner, M. A., *Molecular electronics: a 'chemistry for the 21st century' monograph*; Blackwell Science: 1997.

(11) Stolow, A. *Faraday Discussions* **2013**, *163*, 9–32.

(12) Schinke, R., *Photodissociation Dynamics: Spectroscopy and Fragmentation of Small Polyatomic Molecules*; Cambridge Monographs on Atomic, Molecular and Chemical Physics; Cambridge University Press: 1993.

(13) Stolow, A.; Underwood, J. G. *Advances in Chemical Physics* **2008**, *139*, 497–583.

(14) Khundkar, L. R.; Zewail, A. H. *Annu. Rev. Phys. Chem.* **1990**, *41*, 15–60.

(15) Geneaux, R.; Marroux, H. J.; Guggenmos, A.; Neumark, D. M.; Leone, S. R. *Philosophical Transactions of the Royal Society A: Mathematical, Physical and Engineering Sciences* **2019**, *377*, DOI: 10.1098/rsta.2017.0463.

(16) Namboodiri, V.; Namboodiri, M.; Flachenecker, G.; Materny, A. *Journal of Chemical Physics* **2010**, *133*, DOI: 10.1063/1.3466750.

(17) Okabe, C.; Nakabayashi, T.; Inokuchi, Y.; Nishi, N.; Sekiya, H. *Journal of Chemical Physics* **2004**, *121*, 9436–9442.

(18) Wong, M. C.; Le, A. T.; Alharbi, A. F.; Boguslavskiy, A. E.; Lucchese, R. R.; Brichta, J. P.; Lin, C. D.; Bhardwaj, V. R. *Physical Review Letters* **2013**, *110*, 1–5.

(19) Stolow, A.; Bragg, A. E.; Neumark, D. M. *Chemical Reviews* **2004**, *104*, 1719–1757.

(20) Eland, J. H. D., *Photoelectron spectroscopy*; Butterworths: 1984.

(21) Fischer, I.; Villeneuve, D. M.; Vrakking, M. J.; Stolow, A. *The Journal of Chemical Physics* **1995**, *102*, 5566–5569.

(22) Reid, K. L. *Annual Review of Physical Chemistry* **2003**, *54*, 397–424.

(23) Eppink, A. T.; Parker, D. H. *Review of Scientific Instruments* **1997**, *68*, 3477–3484.

(24) Kregel, S. J.; Thurston, G. K.; Zhou, J.; Garand, E. *Journal of Chemical Physics* **2017**, *147*, DOI: 10.1063/1.4996011.

(25) Kling, N. G.; Paul, D.; Gura, A.; Laurent, G.; De, S.; Li, H.; Wang, Z.; Ahn, B.; Kim, C. H.; Kim, T. K.; Litvinyuk, I. V.; Cocke, C. L.; Ben-Itzhak, I.; Kim, D.; Kling, M. F. *Journal of Instrumentation* **2014**, *9*, DOI: 10.1088/1748-0221/9/05/P05005.

(26) Underwood, J. G.; Sussman, B. J.; Stolow, A. *Physical Review Letters* **2005**, *94*, 1–4.

(27) Lee, K. F.; Villeneuve, D. M.; Corkum, P. B.; Stolow, A.; Underwood, J. G. *Physical Review Letters* **2006**, *97*, 1–4.

(28) Wollenhaupt, M.; Krug, M.; Köhler, J.; Bayer, T.; Sarpe-Tudoran, C.; Baumert, T. *Applied Physics B: Lasers and Optics* **2009**, *95*, 647–651.

(29) Smeenk, C.; Arissian, L.; Staudte, A.; Villeneuve, D. M.; Corkum, P. B. *Journal of Physics B: Atomic, Molecular and Optical Physics* **2009**, *42*, 1–6.

(30) Townsend, D.; Minitti, M. P.; Suits, A. G. *Review of Scientific Instruments* **2003**, *74*, 2530–2539.

(31) Dinu, L.; Eppink, A. T.; Rosca-Pruna, F.; Offerhaus, H. L.; Van der Zande, W. J.; Vrakking, M. J. *Review of Scientific Instruments* **2002**, *73*, 4206–4213.

(32) Lampton, M.; Siegmund, O.; Raffanti, R. *Review of Scientific Instruments* **1987**, *58*, 2298–2305.

(33) Lee, S. K.; Lin, Y. F.; Lingenfelter, S.; Fan, L.; Winney, A. H.; Li, W. *Journal of Chemical Physics* **2014**, *141*, DOI: 10.1063/1.4903744.

(34) Weeraratna, C.; Amarasinghe, C.; Lee, S. K.; Li, W.; Suits, A. G. *Journal of Chemical Physics* **2018**, *149*, DOI: 10.1063/1.5040589.

(35) Baeza-Romero, M. T.; Blitz, M. A.; Goddard, A.; Seakins, P. W. *International Journal of Chemical Kinetics* **2012**, *44*, 532–545.

(36) Geßner, O.; Lee, A. M.; Shaffer, J. P.; Reisler, H.; Levchenko, S. V.; Krylov, A. I.; Underwood, J. G.; Shi, H.; East, A. L.; Wardlaw, D. M.; Chrysostom, E. T.; Hayden, C. C.; Stolow, A. *Science* **2006**, *311*, 219–222.

(37) Vredenborg, A.; Roeterdink, W. G.; Janssen, M. H. *Review of Scientific Instruments* **2008**, *79*, DOI: 10.1063/1.2949142.

(38) *Applied Sciences* **2018**, *8*, 998.

(39) Frasinski, L. J. *Journal of Physics B: Atomic, Molecular and Optical Physics* **2016**, *49*, 152004.

(40) Mikosch, J.; Patchkovskii, S. *Journal of Modern Optics* **2013**, *60*, 1426–1438.

(41) Hillenkamp, M.; Keinan, S.; Even, U. *Journal of Chemical Physics* **2003**, *118*, 8699–8705.

(42) Cho, Y. T.; Na, S. J. *Measurement Science and Technology* **2005**, *16*, 878–884.

(43) Garcia, G. A.; Nahon, L.; Harding, C. J.; Mikajlo, E. A.; Powis, I. *Review of Scientific Instruments* **2005**, *76*, DOI: 10.1063/1.1900646.

(44) León, I.; Yang, Z.; Liu, H. T.; Wang, L. S. *Review of Scientific Instruments* **2014**, *85*, DOI: 10.1063/1.4891701.

(45) Liu, S. Y.; Alnama, K.; Matsumoto, J.; Nishizawa, K.; Kohguchi, H.; Lee, Y. P.; Suzuki, T. *Journal of Physical Chemistry A* **2011**, *115*, 2953–2965.

(46) Muller, A.; Djuric, N.; Dunn, G. H.; Belic, D. S. **1986**, *57*, 349–353.

(47) Wiley, W. C.; McLaren, I. H. *Review of Scientific Instruments* **1955**, *26*, 1150–1157.

(48) Boesl, U. *Mass Spectrometry Reviews* **2017**, *36*, 86–109.

(49) Harrison, G. R.; Vaughan, J. C.; Hidle, B.; Laurent, G. M. **2018**, *148*, 194101.

(50) Ghotbi, M.; Trabs, P.; Beutler, M.; Noack, F. *Optics Letters* **2013**, *38*, 486.

(51) Ghotbi, M.; Beutler, M.; Noack, F. *Optics Letters* **2010**, *35*, 3492.

(52) Ltd., R. VS7550 VUV Mini Spectrometer – Spectrometers, Monochromators and Light Sources from Vacuum Ultra-Violet (VUV) to Visible (Vis) — Resonance Ltd.

(53) Even, U. *EPJ Techniques and Instrumentation* **2015**, *2*, DOI: 10.1140/epjti/s40485-015-0027-5.

(54) Lu, H. C.; Chen, H. K.; Chen, H. F.; Cheng, B. M.; Ogilvie, J. F. *Astronomy and Astrophysics* **2010**, *520*, 5–8.

(55) *Physical Review A - Atomic, Molecular, and Optical Physics* **2001**, *64*, 6.

(56) Hansen, J. E.; Persson, W. *Physica Scripta* **1987**, *36*, 602–643.

(57) Lennartz, S. T.; Marandino, C. A.; Von Hobe, M.; Cortes, P.; Quack, B.; Simo, R.; Booge, D.; Pozzer, A.; Steinhoff, T.; Arevalo-Martinez, D. L.; Kloss, C.; Bracher, A.; Atlas, E.; Krüger, K. *Atmospheric Chemistry and Physics* **2017**, *17*, 385–402.

(58) Montzka, S. A.; Calvert, P.; Hall, B. D.; Elkins, J. W.; Conway, T. J.; Tans, P. P.; Sweeney, C. S. *Journal of Geophysical Research Atmospheres* **2007**, *112*, 1–15.

(59) Glatthor, N.; Höpfner, M.; Leyser, A.; Stiller, G. P.; Von Clarmann, T.; Grabowski, U.; Kellmann, S.; Linden, A.; Sinnhuber, B. M.; Krysztofiak, G.; Walker, K. A. *Atmospheric Chemistry and Physics* **2017**, *17*, 2631–2652.

(60) Brühl, C.; Lelieveld, J.; Crutzen, P. J.; Tost, H. *Atmospheric Chemistry and Physics* **2012**, *12*, 1239–1253.

(61) Mian, C.; Davis, D. D. *Global Biochemical Cycles* **1993**, *7*, 321–337.

(62) Crutzen *Geophysics Research Letters* **1976**, *3*, 73–76.

(63) Attar, A. R.; Bhattacherjee, A.; Pemmaraju, C. D.; Schnorr, K.; Closser, K. D.; Prendergast, D.; Leone, S. R. *Science* **2017**, *356*, 54–59.

(64) Young, L. et al. *Journal of Physics B: Atomic, Molecular and Optical Physics* **2018**, *51*, DOI: 10.1088/1361-6455/aa9735.

(65) Feng, R.; Cooper, G.; Brion, C. E. *Chemical Physics* **2000**, *252*, 359–378.

(66) Lochte-Holtgreven, W.; Bawn, C. E. H. *Transactions of the Faraday Society* **1932**, *28*, 698–704.

(67) Tanaka, Y.; Jursa, A. S.; LeBlanc, F. J. *J. Chem. Phys.* **1960**, *32*, 1205.

(68) Matsunaga, F. M.; Watanabe, K. *The Journal of Chemical Physics* **1967**, *46*, 4457–4459.

(69) Rabalais, J. W.; Mcdonald, J. M.; Scherr, V.; McGlynn, S. P. *Chemical Reviews* **1971**, *71*, 73–108.

(70) Leclerc, B.; Poulin, A.; Roy, D.; Hubin-Franskin, M. J.; Delwiche, J. *The Journal of Chemical Physics* **1981**, *75*, 5329–5348.

(71) McCarthy, M. I.; Vaida, V. *Journal of Physical Chemistry* **1988**, *92*, 5875–5879.

(72) Limão-Vieira, P.; Ferreira Da Silva, F.; Almeida, D.; Hoshino, M.; Tanaka, H.; Mogi, D.; Tanioka, T.; Mason, N. J.; Hoffmann, S. V.; Hubin-Franskin, M. J.; Delwiche, J. *Journal of Chemical Physics* **2015**, *142*, DOI: 10.1063/1.4907200.

(73) Breckenridge, W. H.; Taube, H. *The Journal of Chemical Physics* **1970**, *53*, 1750–1767.

(74) Sivakumar, N.; Burak, I.; Cheung, W. Y.; Houston, P. L.; Hepburn, J. W. *Journal of Physical Chemistry* **1985**, *89*, 3609–3611.

(75) Danielache, S. O.; Nanbu, S.; Eskebjerg, C.; Johnson, M. S.; Yoshida, N. *Journal of Chemical Physics* **2009**, *131*, DOI: 10.1063/1.3156314.

(76) Toulson, B. W.; Murray, C. *Journal of Physical Chemistry A* **2016**, *120*, 6745–6752.

(77) Sofikitis, D.; Suarez, J.; Schmidt, J. A.; Rakitzis, T. P.; Farantos, S. C.; Janssen, M. H. *Physical Review Letters* **2017**, *118*, 1–5.

(78) Sivakumar, N.; Hall, G. E.; Houston, P. L.; Hepburn, J. W.; Burak, I. *The Journal of Chemical Physics* **1988**, *88*, 3692–3708.

(79) Sofikitis, D.; Suarez, J.; Schmidt, J. A.; Rakitzis, T. P.; Farantos, S. C.; Janssen, M. H. *Physical Review A* **2018**, *98*, 1–11.

(80) Black, G.; Sharpless, R. L.; Slanger, T. G. *The Journal of Chemical Physics* **1976**, *64*, 3985–3992.

(81) Pibel, C. D.; Ohde, K.; Yamanouchi, K. *The Journal of Chemical Physics* **1994**, *101*, 836–839.

(82) Itakura, R.; Hishikawa, A.; Yamanouchi, K. *Journal of Chemical Physics* **2000**, *113*, 6598–6607.

(83) Ondrey, G. S.; Kanfer, S.; Bersohn, R. *The Journal of Chemical Physics* **1983**, *79*, 179–184.

(84) Strauss, C. E.; McBane, G. C.; Houston, P. L.; Burak, I.; Hepburn, J. W. *The Journal of Chemical Physics* **1989**, *90*, 5364–5372.

(85) Loo, R. O.; Strauss, C. E.; Haerri, H. P.; Hall, G. E.; Houston, P. L.; Burak, I.; Hepburn, J. W. *Journal of the Chemical Society, Faraday Transactions 2: Molecular and Chemical Physics* **1989**, *85*, 1185–1205.

(86) Wu, S. M.; Yang, X.; Parker, D. H. *Molecular Physics* **2005**, *103*, 1797–1807.

(87) Hishikawa, A.; Ohde, K.; Itakura, R.; Liu, S.; Yamanouchi, K.; Yamashita, K. *The Journal of Physical Chemistry A* **1997**, *101*, 694–704.

(88) Xie, T.; Chen, W.; Yuan, D.; Yu, S.; Fu, B.; Yuan, K.; Yang, X.; Wang, X. *The Journal of Physical Chemistry A* **2020**, *124*, 6420–6426.

(89) Yang, B.; Eslami, M. H.; Anderson, S. L. *J. Chem. Phys.* **1988**, *89*, 5527.

(90) Cossart-Magos, C.; Jungen, M.; Xu, R.; Launay, F. *Journal of Chemical Physics* **2003**, *119*, 3219–3233.

(91) Chen, W.; Hochlaf, P. R.; Z., H. G.; Ng, C. Y. *J. Chem. Phys.* **2002**, *116*, 5612.

(92) Wang, L. S.; Reutt, J. E.; Lee, Y. T.; Shirley, D. A. *Journal of Electron Spectroscopy and Related Phenomena* **1988**, *47*, 167–186.

(93) Morse, S.; Takehashi, M.; Eland, J. H.; Karsson, L. *International Journal of Mass Spectrometry* **1999**, *184*, 67–74.

(94) Eland, J. H.; Berkowitz, J. *The Journal of Chemical Physics* **1979**, *70*, 5151–5156.

(95) Delwiche, J.; Hubin-Franskin, M. J.; Guyon, P. M.; Nenner, I. *The Journal of Chemical Physics* **1981**, *74*, 4219–4227.

(96) Hubin-Franskin, M. J.; Delwiche, J.; Guyon, P. M. *Zeitschrift für Physik D Atoms, Molecules and Clusters* **1987**, *5*, 203–216.

(97) Hikosaka, Y.; Hattori, H.; Hikida, T.; Mitsuke, K. *Journal of Chemical Physics* **1997**, *107*, 2950–2961.

(98) Holland, D. M.; Shaw, D. A. *Chemical Physics* **2016**, *479*, 151–159.

(99) Hikosaka, Y.; Hattori, H.; Mitsuke, K. **1999**, *110*, 335–344.

(100) Ellis, A.; Feher, M.; Wright, T., *Electronic and Photoelectron Spectroscopy: Fundamentals and Case Studies*; Cambridge University Press: 2005.

(101) Martin, W. C.; Zalubas, R.; Musgrove, A. *Journal of Physical and Chemical Reference Data* **1990**, *19*, 821–880.

(102) Wu, G.; Boguslavskiy, A. E.; Schalk, O.; Schuurman, M. S.; Stolow, A. *Journal of Chemical Physics* **2011**, *135*, DOI: 10.1063/1.3652966.

(103) Schalk, O.; Boguslavskiy, A. E.; Stolow, A. *Journal of Physical Chemistry A* **2010**, *114*, 4058–4064.